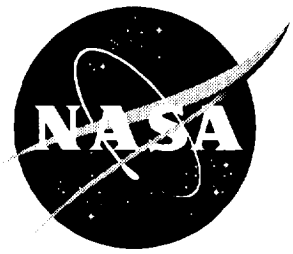

NASA Technical Paper 3672

Application of Wind Tunnel Free-Flight Technique for Wake Vortex Encounters

Jay M. Brandon, Frank L. Jordan, Jr., and Robert A. Stuever
Langley Research Center • Hampton, Virginia

Catherine W. Buttrill
Unisys Corporation • Hampton, Virginia

National Aeronautics and Space Administration
Langley Research Center • Hampton, Virginia 23681-2199

November 1997

Available electronically at the following URL address: http://techreports.larc.nasa.gov/ltrs/ltrs.html

Printed copies available from the following:

NASA Center for AeroSpace Information
800 Elkridge Landing Road
Linthicum Heights, MD 21090-2934
(301) 621-0390

National Technical Information Service (NTIS)
5285 Port Royal Road
Springfield, VA 22161-2171
(703) 487-4650

Summary

A wind tunnel study was conducted to determine the feasibility of using the free-flight test technique to study wake vortex encounters. A generic business-class jet airplane model was instrumented and flown in the vicinity of a wake vortex generated by a simple wing. The strength of the vortex could be varied by adjusting the generating-wing angle of attack. The variation in the strength of the vortex allowed researchers to study a range of simulated vortex strengths for a fixed-span ratio of 0.75 and enabled the simulation of various following distances and generator airplane weights without the uncertainties in vortex decay and atmospheric effects. The study showed that the free-flight test technique was a viable and useful tool in the study of the wake vortex encounters—combining vortex flow fields, airplane dynamics, sensors, and flight control aspects.

Data obtained during this test included qualitative and quantitative results. Steady-state limits of controllability were documented as a function of vortex strength. By flying several vortex encounter trajectories at high vortex strengths, a mapping was conducted of roll angle, roll rate, lateral velocity, and vortex-induced roll-rate acceleration. The data quantified the effects of the model entering vortex flow fields of varying strengths.

Introduction

The National Aeronautics and Space Administration (NASA) is conducting research that will enable safe improvements in the capacity of the air transportation system. As part of this research, the Terminal Area Productivity (TAP) program has the goal of safely achieving capacity levels during instrument meteorological conditions equivalent to those currently achievable under visual meteorological conditions. One element of TAP, Reduced Spacing Operations (RSO), focuses on both lateral and longitudinal separation requirements. A key concern for reducing spacing requirements, especially when an airplane is following large aircraft on an approach, is the danger of upsets generated by the wake vortex of the preceding aircraft. Consequently, part of the current NASA research effort focuses on developing and validating the technologies required for an automated Aircraft Vortex Spacing System (AVOSS, ref. 1), which will properly select safe separation distances for different weather conditions based on the aircraft pair and predicted-measured vortex behavior. Although the AVOSS will generally attempt to space aircraft to avoid any wake encounter at all, it must be able to select a separation distance at which a wake encounter is safe and operationally satisfactory, should one occur.

Defining a safe, operationally satisfactory wake encounter for a given aircraft pair under any one condition has proved very difficult. In addition to being able to adequately model the decay and advection of a wake vortex in the atmosphere, an equally important element is a valid model that represents the wake vortex encounter itself. Substantial analytical research has been conducted in vortex modeling (refs. 2 through 4), in vortex-airplane interaction, and in resulting forces and motions (refs. 5 through 7) to try and quantify or predict hazards. Experimental research has been conducted both in flight (refs. 8 through 10) and in wind tunnels (refs. 11 and 12) to provide information on the wake vortex flow fields produced by various airplanes and to investigate loads imposed by an aircraft wake vortex on following airplanes.

The free-flight test reported in this paper extends the research database by experimentally investigating the dynamic response characteristics of a follower aircraft during wake vortex encounters. This was the first attempt to conduct such tests in a wind tunnel, and was viewed primarily as a feasibility test to determine whether the free-flight test technique was a useful research tool in wake vortex encounter research. Specific objectives for this test were (1) to see if the model could be flown safely and maneuvered accurately in a wake vortex flow field of specified strengths, (2) to develop photogrammetry techniques for measuring the position of the model relative to the vortex, (3) to estimate rolling moments imposed on the model due to the vortex flow field while flying, and (4) to conduct exploratory qualitative evaluations of relative upsets for various encounter trajectories. Related work involved selecting appropriate flight control system approaches to enable these tests to be conducted successfully. Flight test data obtained in the past were very difficult to analyze and apply in any general sense due to large uncertainties in the data. For example, two significant uncertainties are the strength and position of the vortex which is encountered. It is well-known (ref. 13, for example) that atmospheric effects play a predominant role in the dissipation characteristics of a wake vortex. Also, it is very difficult in flight experiments to repeatably conduct the same encounter flight paths which would allow high confidence in the results. In proposing this wind tunnel experiment, it was assumed that the vortex characteristics in the wind tunnel would remain essentially constant with time (only be affected by turbulence levels in the tunnel and temperature-pressure variations during the day). Additionally, the level of the vortex strength may be easily controlled by increasing or decreasing the lift of the wake vortex generator. In this way, the effects of vortex strength on the dynamics of an airplane can be studied. The results of this study can be applied to a range of generating airplane pairs (with span

ratios of 0.75) and separation distances by calculating or measuring the vortex intensity at the follower-airplane location.

The metric defining a safe and operationally satisfactory vortex encounter may entail very small allowable perturbations in aircraft attitude, as well as relatively little required corrective control activity. However, in light of the wake encounters reported herein that were being flown as part of a feasibility test to evaluate the free-flight technique, it is important to note that the subsequent upsets often and deliberately exceeded what might be regarded as acceptable. Exceeding what were regarded as acceptable upsets was necessary to determine the feasibility limits for planned follow-on tests and to establish how an aircraft will respond to wake turbulence and the magnitude of controls that must be provided to correct for it. Similarly, although the results from this test may be combined with results from other research efforts to identify wake encounter metrics, it should be noted also that the intent of this experiment was not to establish an acceptable level for an upset metric.

Symbols

b	wingspan, ft
C_L	lift coefficient
C_{L_α}	lift-curve slope per deg
C_l	rolling-moment coefficient
$C_{l_{\delta_a}}$	$= \frac{\partial C_l}{\partial \delta_a}$, per deg
$C_{l_{\delta_r}}$	$= \frac{\partial C_l}{\partial \delta_r}$, per deg
c	mean aerodynamic chord, ft
g	normalized acceleration
I_X	roll axis inertia, slug-ft^2
I_Y	pitch axis inertia, slug-ft^2
I_Z	yaw axis inertia, slug-ft^2
i_t	horizontal tail incidence angle, deg
n_y	lateral acceleration, g units (positive right)
n_z	normal acceleration, g units (positive up)
p	roll rate, deg/sec
q	pitch rate, deg/sec
$\bar{q}$	dynamic pressure, psf
R	distance of follower model from vortex core, in.
r	yaw rate, deg/sec
S	reference wing area, ft^2
t_{30}	time required to reach 30° bank angle
U_∞	free-stream wind tunnel velocity, ft/sec
V_{so}	stall speed in landing configuration, ft/sec
x	downstream distance measured from the generating-wing quarter-chord
z	vertical distance, ft
α	angle of attack, deg
α_v	$= 0.5(\alpha_s - \alpha_p)$, deg
β	angle of sideslip, deg
Γ	vortex strength, ft^2/sec
δ_a	aileron deflection, $\frac{\delta_{a_s} - \delta_{a_p}}{2}$, deg
δ_e	elevator deflection, deg
δ_r	rudder deflection, deg
θ	pitch angle
θ_v	radial location of follower model relative to vortex core location, deg
σ	density ratio of air at full-scale flight conditions to model flight conditions at sea level
τ_r	roll mode time constant
ϕ	roll angle, deg
ψ	yaw angle, deg

Subscripts:

f	follower airplane
fs	full scale
g	vortex generator wing
p	port side
ms	model scale
s	starboard side
ss	steady state
v	vortex induced

Abbreviations:

ARI	aileron-rudder interconnect
ATP	advanced turboprop
AVOSS	Aircraft Vortex Spacing System
FAR	Federal Aviation Regulations
FCS	flight control system
FS	full-scale value
hsw	hardware switch
MS	model scale value
N	model scale

NLF natural laminar flow

RSO Reduced Spacing Operations

TAP Terminal Area Productivity

Model Description and Test Techniques

The overall test technique used for the free-flight experiment is illustrated in figure 1. The primary components are a wing in the forward section of the wind tunnel to generate a wake vortex flow field, a model flying unconstrained behind the wing in and around the wake vortex flow field, and instrumentation required to fly the model and to obtain data for analysis. Further details of the test setup and conduct will be given herein. The coordinate system used in the tests was based on the location of the starboard vortex of the generating wing. Model position data presented will be referenced to a radial distance from the measured vortex core location and an angle. The angle θ_v is defined as increasing clockwise from the horizontal three o'clock position relative to the vortex.

Vortex Generator Wing

The model used to generate the wake vortex was a rectangular planform aspect ratio 7.0 wing with a span of 12 ft, a chord of 1.71 ft, and a NLF(1)-0215F general aviation airfoil section. The wing was constructed of fiberglass and epoxy with an aluminum spar. Further details regarding the airfoil section can be found in reference 14. Overall aerodynamic forces and moments acting on the model were measured on an internal six-component balance, in part to enable estimation of the subsequent shed vortex strength from lift but also to monitor loads on the test rig. Smoke generator tubes using heated propylene glycol vapor were installed along the wing trailing edge to produce smoke at the wingtips to seed the vortex so that it would be visible for the flight encounters. The figure 2 photograph shows the wing installed in the Langley 30- by 60-Foot Tunnel (with the smoke generators operating). During the free-flight vortex encounters, all available smoke was concentrated in the starboard vortex to improve visual definition of the vortex core location. The figure 2 photograph also shows illumination of the vortices by a laser light-sheet technique, which will be described subsequently in the Free-Flight Tests section.

Follower Airplane

The geometric characteristics of the follower model airplane are depicted in figure 3. The model was constructed of fiberglass and epoxy. The mass and geometric properties were scaled to simulate a representative business-commuter aircraft for the purpose of determining flight characteristics from free-flight tests in the Langley 30- by 60-Foot Tunnel. Geometric and mass characteristics of the model are shown in table I. The intent of the investigation was to explore vortex encounters with the follower model in the high-lift-landing-approach condition; therefore, the configuration had the trailing-edge flaps deflected 35°. Model control-surface deflection limits were δ_a = +20° to −20°; δ_e = +15° to −25°; and δ_r = +20° to −20°. Horizontal tail incidence angle i_t could be varied from +2° to −10° to provide an extended range of pitch trim; however, i_t was fixed at 0° for the current test. No landing-gear geometry was included on the model.

The model also incorporated full-span Krüger flaps. Previous free-flight test results of the model configured as an advanced turboprop (ATP) (ref. 14) indicated that this configuration exhibits an abrupt wing drop and autorotative departure against full corrective control at the stall angle of attack. Static wind tunnel test results showed that the wing drop was due to an abrupt asymmetric wing stall that produced a pronounced rolling moment. Additional free-flight tests of the configuration, modified to include wing leading-edge devices such as Krüger flaps, showed that the modified configurations had acceptable overall flying qualities and no significant stability and control problems, even at post-stall angles of attack. Sketches and other details of the full-span Krüger flaps that were used on the model can be found in reference 15.

The model was powered with two thrust tubes installed on each side of the aft part of the fuselage. The thrust tubes only provided thrust to fly the model, and no attempt was made to simulate thrust characteristics of any specific airplane configuration.

Scaling Discussion

A straight, unflapped wing was selected to be the wake vortex generator because of the properties of rapid vortex rollup and essentially constant vortex strength for long downstream distances (ref. 16). Because of these characteristics, vortex strength at the location of the follower model could be estimated for an elliptically loaded wing by using the approximation: $\Gamma = \frac{2C_L U_\infty S_g}{\pi b_g}$. The vortex core size may not have been representative of full-scale flight conditions in these tests. This core size is currently believed to be of minor importance due to the large ratio of wingspan to vortex core diameter both in flight and in these wind tunnel tests.

To scale results from the current test and relate them to a full-size airplane, the flow angularity distribution caused by the vortex on the current follower model and the full-scale airplane must be equivalent. Additionally,

the follower model must have appropriate dynamically scaled mass and inertia values and similar aerodynamic characteristics compared to the full-scale airplane.

The scaling considerations dictate that the results are dependent on wingspan ratio between the generating wing and the follower aircraft. To apply the results directly, the span ratio must be equivalent in flight to the wind tunnel test values, and the model mass characteristics must be appropriately scaled. Then, the vortex strength estimated at the point of the encounter (at the follower airplane location) can be related to the present results by using generating-wing lift coefficients. For the current test, the wingspan ratio was $b_f/b_g = 0.75$. For discussion later in this report, the follower model will be considered to be at 0.175 scale, which is representative of an experimental test bed aircraft described in reference 17. These factors result in conditions representative of a business jet airplane following a commuter airline airplane. Table II shows a comparison of generating-wing lift coefficient, vortex strength, and full-scale vortex strength. The lift characteristics of the generating wing are shown in figure 4. Due to dynamic scaling relationships, the small-scale models tested with the free-flight test technique develop considerably faster responses than full-scale airplanes. Some scaling factors are shown in table III.

Free-Flight Tests

The wind tunnel free-flight tests were conducted in the Langley 30- by 60-Foot Tunnel with the technique illustrated in figure 1. With this technique, the remotely controlled, dynamically scaled model was flown in the open test section of the Langley 30- by 60-Foot Tunnel. For most of the tests, a vortex generating wing was mounted in the forward section of the wind tunnel. As previously discussed, the generating-wing angle of attack was varied to enable selection of an approximate vortex strength. The vortex core was marked with propylene glycol smoke to enable the free-flight pilots to position the flying model in desired locations relative to the wingtip vortex created by the upstream wing. Figure 5 is a photograph of the model flying in the vortex during the test. The wind tunnel free-flight tests were used first to evaluate the flying characteristics of the airplane with the various control laws and then to evaluate the dynamic response and controllability of the model near vortices of various strengths. Hence, prior to mounting the generating wing in the tunnel, the free-flight model was flown to evaluate the control law implementation and to adjust the gains to ensure that the model was well-behaved in free air. Next, for the vortex encounter tests, the model was first flown near the vortex, and then penetrations of the vortex were made from various trajectory paths. The resulting model motions were measured, and pilot comments were recorded for each flight condition. All vortex encounters were conducted at a tunnel speed corresponding to $1.3V_{so}$ with the airplane flaps configured for landing.

During the free-flight tests, the model was attached to an umbilical chord which supplied pneumatic and electric power and control signals to the model. The chord also contained a 1/8-in. steel safety cable that was controlled by a safety cable operator using a high-speed pneumatic winch. The safety cable operator's function was to help launch the model at the start of a test, to retrieve the model at the end of a test, to keep tension off the model from the umbilical cable during the test, and to attempt to protect the model in an out-of-control situation by pulling the model out of the airstream.

In addition to the safety cable operator, the model flight crew consisted of a pitch pilot, a thrust pilot, and a roll-yaw pilot. These piloting functions were located in the positions shown in figure 1 to afford the best view for controlling the pertinent axes. The separation of the piloting duties is very advantageous for several reasons. By separating pilots by axes, effective evaluations can be obtained more easily because the pilot is only controlling the axes he is trying to evaluate. Model control is also enhanced by providing the optimal visual perspective for control of each axis. Due to dynamic scaling, the model motions are substantially faster than those of the full-scale airplane, so separation of piloting tasks is beneficial for that reason as well.

The primary component in the free-flight control system is a digital minicomputer that was programmed with the flight control laws (presented in the appendix). The computer processed sensor information from the model and command inputs from the pilots to generate command signals to drive the high-speed pneumatic actuators onboard the model. The data sensors on the model included a three-axis rate gyro to measure angular rates, an accelerometer package to measure normal-, axial-, and side-force accelerations, a boom-mounted α/β vane sensor on each wingtip for angle of attack and sideslip, potentiometers to measure control-surface positions, and a transducer to measure pressure at the thrust tube for thrust estimations. These sensor data, along with pilot control inputs, were recorded in the computer for postflight analysis. Angular rates, linear accelerations, and α/β vane sensor data were filtered with a first order lag filter with a time constant of 0.05 sec before entering the FCS. Additionally, α and β from the wingtip mounted vanes were corrected for angular rates. Postflight data reduction included incorporating upwash corrections to the α data based on static wind tunnel test results obtained previously, correction of accelerometer

data to the model center-of-gravity location, and calculation of angular accelerations by differentiation of measured angular rate data.

Additional quantitative flight data were recorded by using photogrammetry techniques applied to free-flight testing for the first time (ref. 18). The model and the wind tunnel test section were marked with photo reflective spots at known locations. A camera above the exit cone in the tunnel was used to track the model. Postflight analysis of the tracker camera data was used to obtain model Euler angles and position in the wind tunnel. The location of the wingtip vortex produced by the generating wing also was located photogrammetrically. The smoke was marked in three locations by a laser light sheet. The forward position was illuminated by an Argon laser located just outside the balcony used by the pitch and thrust pilots. The middle and aft positions were illuminated by diode lasers mounted on the wind tunnel ground board. The intersection of the smoke and the light sheets was then used to determine the vortex core location during the test. Figure 6 is a photograph of the test setup showing the lasers. The locations of the plane of the laser light sheets relative to the quarter-chord of the generator wing are shown in table IV. Additional qualitative data were recorded, including pilot comments and video recordings of the model flights. Table V lists the transducer accuracies and data system resolutions which were available for the key recorded parameters during the test. A discussion of the photogrammetry data factors is available in reference 18.

Free-Flight Test Results

During the wind tunnel free-flight tests, the model was evaluated by using various flight control system features. Although the flight control system was not considered a primary area of interest for this test, it was necessary to provide the pilots with a model possessing good flying qualities to conduct the vortex encounter flights. Three longitudinal flight control system architectures were developed for the test: α-command, pitch rate command, and g-command. The α-command system was a direct link between the pitch stick and elevator positions and also included pitch rate damping. The pitch rate command system used the pitch stick position to command a pitch rate, and with no pitch stick input, the model control laws would attempt to maintain the current pitch attitude. The g-command system used the pitch stick position to command normal acceleration (load factor), and with no pitch stick input, would seek a $1g$ flight condition. Additionally, because of the higher rates developed in dynamic model testing, roll and yaw rate damping augmentation was added to aid in flying the model in the wind tunnel. More detail about the flight control system is presented in the appendix. This test represented the first time the wind tunnel free-flight test technique was used to study wake effects on a flying model. As such, several challenges were overcome to provide pertinent results. These challenges included flying the model in very precise locations in the wind tunnel, relative to the vortex, and measuring the model position and attitude angles in addition to the vortex core location for postflight analysis. Additionally, tests were conducted without the vortex generating wing installed to determine model flying characteristics and to establish minimum controllable airspeed (V_{so}), which determined the tunnel speed for the remainder of the testing.

Free-Air Flight Characteristics

The model was easily flown in free air (no vortex generating wing upstream) in each of the longitudinal flight command modes. The α-command mode was used throughout most of the free-air flights because it is a traditional flight control system and pilots are very familiar with it. The airplane could be flown with pitch rate damping removed; however, the resulting airplane motions were much more lively. The pitch rate command mode was very easy to fly; however, some pilot learning was involved for pilots to become comfortable with the integrated control path, which resulted in the pitch attitude remaining wherever it was when the stick was released. The g-command system also resulted in an easily controllable model.

Several options were programmed into the lateral-directional control laws. Similar to the longitudinal case, some experimentation was conducted to arrive at an acceptable flying airplane for the wake vortex encounter task. The unaugmented airplane was found to exhibit unfavorably low damping in roll and therefore required artificial roll damping for acceptable handling qualities. Additionally, the aileron-to-rudder interconnect (ARI) feature was used to alleviate adverse yaw and to enable the model to fly in the lateral axis with only one controller (roll). Yaw rate feedback to the rudder was used to reduce Dutch-roll oscillations during flight. Side acceleration feedback to the rudder was flown with and without the ARI engaged and was found to increase the ease of maintaining a lateral position in the tunnel; however, it degraded the maneuver capability needed to reposition the model. Differential angle-of-attack feedback to the ailerons from the two wingtip booms was also evaluated, but as expected, because the α signals were rate corrected, they did not influence the flight characteristics of the model in free air. After the flying qualities investigation was complete, the baseline configuration for the lateral-directional control system consisted of an ARI and artificial roll and yaw rate damping.

Flight-determined static stability. The lift coefficient and pitching-moment characteristics could be deduced in flight by stabilizing at $1g$ flight conditions at various tunnel speeds. As the tunnel airflow speed was decreased, the angle of attack of the model increased for level flight. A comparison of lift coefficient measured in flight with that measured during a static wind tunnel test of the same model is shown in figure 7. It is important to note that the data from reference 15 include pylon-mounted engines with propellers generating zero thrust with an untrimmed model. These data show reasonable agreement with data measured on the model of reference 15. Indications of pitching-moment characteristics are shown in figure 8 as average elevator angle at the trim angles of attack. Comparison with data calculated from reference 15 shows that the model is somewhat less stable in the current configuration without the pylons and propellers. The roll control effectiveness was not directly measured in flight, but the static wind tunnel results from reference 15 are shown in figure 9.

Identification of $1.3V_{so}$. The airflow velocity in the wind tunnel was progressively slowed to evaluate the slow-speed characteristics of the model and to determine the minimum controllable flight speed in the power-approach configuration. The model departed controlled flight due to insufficient pitch and roll control at a dynamic pressure of 5.4 psf, which resulted in a model angle of attack of approximately 10°. Based on these results and Federal Aviation Regulations (FAR), which allow an approach speed of at least $1.3V_{so}$, the remainder of the testing was conducted at a tunnel dynamic pressure of 9.0 psf, which is equivalent to a full-scale approach speed of about 120 knots.

Dynamic response characteristics. Flight control system (FCS) gains were adjusted in real time during initial flights in the wind tunnel to arrive at acceptable flying qualities for the tests. After setting the FCS gains, dynamic response characteristics were converted to full-scale values and compared with airplane handling qualities criteria to ensure that the model was still representative of actual full-scale airplanes. Model dynamic response characteristics for the various flight control system modes were obtained by performing doublet control inputs and observing the resultant model motions. The typical free-flight control system has traditionally been an α-command system with proportional feedbacks for stability. The α-command system, which provided the pilot with what he considered to be good characteristics, gave a short-period mode with a frequency of approximately 1.56 Hz (0.65 Hz full scale) and a damping ratio of approximately 0.6. These dynamic characteristics, along with a n/α = 5.9 g/rad, meet level I requirements for a full-scale airplane based on military specifications (ref. 19). The g-command and q-command control systems introduced higher order dynamics; however, each system resulted in a model with very desirable handling characteristics for the free-flight task of limited maneuvering in free air conditions.

The lateral dynamic response was similarly obtained both with dampers-on and dampers-off conditions. All lateral-directional maneuvers were conducted with the ARI engaged. The roll mode time constant and maximum roll rates achieved during free-flight handling qualities evaluations for the bare airframe (dampers off) and the augmented configuration (dampers on) are shown in table VI. These values also are shown scaled to representative full-scale values and are compared to reference 19 requirements for a class II land-based airplane during approach. As can be seen, the roll rate damper limited roll rate capability because it did not differentiate between a commanded or an uncommanded roll rate.

Vortex Flow Field Encounters

After establishing flight control system gains to ensure good flying characteristics for the model, the vortex generating wing was installed in the forward portion of the wind tunnel test section. Initial flights were made with the wing at zero lift angle of attack, and it was noted that there was significantly more turbulence experienced by the model due to the wing and its support (fig. 6). An interesting phenomenon occurred when the generating-wing angle of attack was slightly increased to generate a small amount of lift. The flow in the tunnel appeared much smoother when there was a slight increase of generating-wing angle of attack when flying the model. The wake generated by the wing at low lift coefficients is believed to have smoothed out the turbulence generated by the support structure by the time it reached the area in which the model was flying.

As the wing angle of attack was further increased, generating wake vortices, the flow field characteristics were very evident in the flight characteristics of the model. Figure 10 shows a schematic of the flow field characteristics around the wake vortex. The starboard vortex (right vortex looking upstream) was the vortex used for vortex encounters. The figure shows an area of upwash to the right of the vortex and downwash to the left of the vortex (between the starboard and left wingtip vortices). This upwash-downwash flow field made it very difficult to accurately position the model vertically, while maneuvering laterally. Each longitudinal command mode was evaluated to determine the best configuration for conducting the vortex encounters. The g-command mode minimized the vertical excursions of the model while it was flying through the vortex flow

field. This command mode was used in all transient vortex encounters presented herein.

The vortex generated by the upstream wing exhibited its own set of dynamics. The vortex core location wandered approximately ±5 in. in the vertical and lateral directions, as shown in figure 11. These data represent the vortex core location movement over a time interval of approximately 0.5 sec, with the wind tunnel operating at a dynamic pressure of approximately 5.3 psf. The data were obtained with the free-flight model removed from the test section. The vortex core position was measured by using photogrammatic techniques described in reference 18 to locate spatially the centroid of the smoke marking the vortex core that was illuminated by laser 3. Laser 3 was located beneath the vortex track a distance of x/b_g = 2.6. Most free-flight testing was conducted at a wind tunnel dynamic pressure of 9.0 psf; however, the meander of the vortex was qualitatively the same at either wind tunnel dynamic pressure.

A simple calculation was made to estimate the vortex-induced rolling moment on the follower model during vortex encounters. The assumptions required for this calculation were that the control power effectiveness was invariant during the encounter (given by the data in fig. 9). Effects of roll rate damping and dihedral were neglected. Specifically, the vortex-induced rolling moment was estimated by

$$C_{l_v} = \frac{\ddot{\phi}_f I_X}{\bar{q}Sb} - C_{l_{\delta_a}}\delta_a - C_{l_{\delta_r}}\delta_r$$

Although not a part of the current study, a comparison between statically measured and dynamically derived rolling moments may be useful in addressing the importance of dynamic effects in predicting vortex encounter hazards.

Steady-state encounters. A systematic set of vortex encounters were flown to establish steady-state conditions in the vortex. These test points were conducted by establishing the generating-wing angle of attack and the resulting flow field, and then the model was flown into the smoke marking the vortex core of the tip vortex. The model was stabilized with the fuselage in the center of the vortex core (marked by smoke) for several seconds for data recording. The test runs started with the generating wing at zero lift, and then the angle of attack of the wing was increased in 1° increments until the free-flight model could no longer maintain position in the vortex flow field. To aid in the application of these data in a general sense, all generating-wing vortex strength data will be represented by using the wing lift coefficient as shown previously in table II. Figure 12 shows the result of the steady-state encounters. The model could be stabilized in the vortex flow field up to a C_{L_g} of approximately 0.7. At that point, roll control on the model was saturated, and the model could not maintain position in the vortex.

As the vortex in which the model was flying increased in strength, the flow field sensed by the wingtip-mounted α/β vanes showed the increase in rotational flow. Figure 13 shows the difference between the angle-of-attack measurement at the left and right wingtips. These data were obtained with the model positioned directly in the vortex core. The data show that as the vortex strength is increased, the difference in the angle of attack of the right and left wingtip increases. The predicted rolling-moment effects on the model due to the vortex flow field are shown in figure 14. These data were calculated by using the differential wing angle of attack and by assuming a linear upwash-downwash distribution across the span of the model with the following equation:

$$\Delta C_l = -\frac{C_{L_\alpha}\alpha_v}{6}$$

where C_{L_α} = 0.107 was obtained from free-flight data records. Though the assumption of linear upwash-downwash distribution across the span of the model does not physically represent typical vortex flow-field characteristics, the prediction based on differential α shows reasonable agreement with free-flight data (fig. 12) as to the strength of the vortex in which the model can be flown in steady-state controlled flight.

Transient vortex encounters. Most research flight maneuvers were conducted to obtain data as the model was maneuvered near and through the core of the starboard vortex. As previously discussed, several encounter profiles were flown with the generating wing set at various angles of attack to provide a wake vortex strength variation. The transient vortex encounters began with a generating-wing angle of attack of 8° for a C_{L_g} of approximately 0.95 and ended at the maximum wing angle of attack of 13.4° that was available in the tunnel for a C_{L_g} of approximately 1.25. As previously mentioned, testing was conducted with vortex strengths far beyond what would be expected to yield acceptable flight encounter boundaries. This testing was done primarily for two reasons: (1) to validate and explore fully the use of the free-flight test technique in these applications, and (2) to obtain a set of data with large amplitude effects for possible use later in the validation of modeling and prediction techniques. Additionally, the large vortex strength data ensured that the observed effects were significantly greater in magnitude than would occur due to normal wind tunnel turbulence.

Time-history data for vortex encounters for a range of vortex strengths and for the four general encounter trajectories are discussed in this section, and overall trends from the data will be discussed subsequently. The four encounter trajectories were (1) to descend directly through the starboard vortex core, (2) to climb directly through the vortex core, (3) to translate from the right side of the vortex to between the generating-wing vortex pair, and (4) to translate from between the vortex pair through the vortex to the right side outside the vortex. Model position data will be presented relative to the vortex position which was measured during the run at laser location 2 at the initiation of a data run. Note that the actual vortex core location at the follower model likely would differ due to downstream distance and the interference effects of the follower model on the vortex. The vortex core (marked by smoke) tended to go around the model rather than to impact directly; therefore, it was very difficult to position the model directly in the vortex center. The sign convention for the position (radius and angular position) is shown in figure 15. Most of the free-flight data were obtained at a downstream distance from the generating-wing quarter-chord location of approximately 24 ft (2 spans of generating wing). Figure 16 shows a histogram of the distance between the generating wing and the follower model, including all data points reported herein.

Figures 17 and 18 show data for a vortex strength corresponding to $C_{L_g} = 0.95$. Figure 17 shows a horizontal approach from right to left. As the model crosses through the starboard vortex core ($t = 5.5$ sec), the vortex flow field causes the model to descend and roll to the left. The time-history data show full-right lateral controls to oppose the vortex-induced moments while the model is near the vortex core. As the left wingtip approaches the vortex, the flow vanes on the wingtip boom show a large upwash and also substantial sidewash. As the wingtip passes beyond the vortex core location, an abrupt change from upwash to downwash occurs. After crossing through the vortex, pitch attitude increased to enable level flight in the downwash flow field that existed between the two vortices created by the generating wing.

Figure 18 shows a vortex penetration attempt beginning between the vortex pair and translating to the right. Despite nearly full-right controls, less than 10° of right bank could be generated, and thus the translation rate was very small. Even with full-right controls while near the starboard vortex, the model was rolled to the left, was unable to pass through the vortex, and instead translated back to a lateral location between the vortex pair. This maneuver was repeated at a faster lateral translation rate and resulted in a successful transition through the vortex to the free air on the right side of the tunnel.

Pilot comments at a $C_{L_g} = 0.95$ indicated that the vortex produced rolling moment when the model was near the vortex core, exceeded the control capability of the model, and usually resulted in uncommanded left roll rate and translation down and to the left. Recovering control of the model, once it was away from the core location, was accomplished easily, and the ability to regain positive control of the model before exceeding the wind tunnel test section area was never seriously in doubt.

Figures 19 through 21 show data for $C_{L_g} = 1.07$. Figure 19 shows a horizontal approach from right to left. The trajectory shows, by a rise in the flight path, the effect of the upwash as the model approaches the vortex. As the model crosses through the vortex, it develops a left-wing-down-roll attitude and descends out to the left of the generating-wing starboard vortex The left wingtip probe dramatically shows the crossing of the vortex by the large upwash just prior to the wingtip entering the vortex core and by the immediate change to large, negative-sensed angles of attack after the wingtip crossed through the vortex core. The distance to the vortex core at which α begins to increase ($t = 1.3$ sec) is approximately 80 in. from the model center of gravity or 26 in. from the wingtip. At this location, the vortex flow field produces a small, positive rolling moment ($C_{l_v} > 0$). The model center of gravity distance to the vortex is 29 in. before vortex-induced rolling moment to the left ($C_{l_v} < 0$) is produced. As seen for the $C_{L_g} = 0.95$ case, the model controls are saturated against the vortex-induced left rolling moment as the model flies through the vortex core. The large roll angle, to which the model was disturbed due to the vortex, elicited pilot comments that this condition resulted in less certainty of easily regaining control after the vortex encounter; however, the control was regained without exceeding the wind tunnel test envelope limitations.

Vortex penetration attempts were also flown by using descending trajectories (fig. 20) and climbing trajectories (fig. 21). During the descending trajectory, the pilot had difficulty in positioning the model directly over the vortex core due to the effects of the rotational vortex flow field. The trajectory shows that the model passed to the left of the vortex position rather than through the core as intended. Roll control and roll rate activity show the difficulty experienced by the pilot in attempting to position the model. When the model approached the vortex, full controls were used again to oppose the vortex-induced rolling motions while the model was rolled and descended out the vortex to the left. The climb through the vortex (fig. 21) shows that the model again failed to pass directly through the reference vortex core location, although it was very close. Again, full opposing controls were required, and the model was pushed away towards the left of the vortex as it climbed. The wingtip probe did

not indicate the presence of the vortex prior to the encounter for the vertical trajectories. Pilot comments indicated that the vertical trajectories were much less dramatic than the horizontal trajectories for this generating-wing angle of attack because of the larger bank angles generated from the horizontal entry, and because the controls were set to substantial left roll commands in order to penetrate the vortex, which then had to be rapidly reversed when the model had reached nearly into the vortex core. For the vertical entries, large left-roll control was not needed, and the resultant roll angle perturbations were less.

Figures 22 through 25 show data for a vortex strength corresponding to $C_{L_g} = 1.18$. Figure 22 shows a horizontal approach from right to left. As the model approached the vortex, the upwash flow field generated a positive (roll-away) moment as indicated by positive values of C_{l_v} and required the lateral control deflections. The maximum value of positive rolling moment occurred when the model center of gravity was approximately 50 in. from the vortex. The sign of the vortex-induced moment changed at approximately 29 in. and reached a maximum value at the minimum distance, that is, model center of gravity in the vortex core. Controls were saturated for a substantial time during the penetration to oppose the left roll generated by the vortex. The wingtip probe showed the effect of the vortex with an increase in upwash that was measured beginning at a distance of 118 in. (t = 0.9 sec) and then a further rapid increase beginning at about 80 in. (t = 1.8 sec). The flow changed to downwash again as the wingtip passed the vortex position. Sideslip for this encounter showed a rapid increase beginning at about 62 in. (t = 2.1 sec) from the reference vortex position and changed sign to negative sideslip as the wingtip crossed the vortex. This sideslip response differs from the results shown at $C_{L_g} = 1.07$ where the sideslip initially showed negative values as the vortex was approached from the right. Slight differences in the vertical positioning of the model, relative to the vortex, may be responsible for this measured difference. Additionally, as previously noted, the vortex tended to move around the model when the model approached the vortex. This motion is not reflected in the plotted data because positions were recorded relative to the reference vortex location.

Vortex encounters also were flown from left to right, and pilot comments indicated that the model was more difficult to position than for right-to-left translations. Unless a reasonable translation rate was established, it was impossible to overcome the left rolling moment and successfully pass through the vortex. Figure 23 shows an example of an unsuccessful penetration attempt from the left. The trajectory shows the model translating from left to right, and when the model just reaches the vortex, it is pushed out rather violently to the left and down. Full-right lateral control was required, beginning when the model was within 29 in. of the reference vortex position. The wingtip probe shows that the wing experiences effects of the left generating-wing vortex flow field at the beginning of the run. Also note that the model pitch attitude is much higher (9° versus 3°) for the case in which the model is initially between the generating-wing vortex pair. The increased pitch attitude is an indication of the downwash field between the vortices, and pilot comments noted difficulty in climbing while in this location.

Vertical trajectories through the vortex were flown with both descending and climbing approaches (figs. 24 and 25). For the descending approach, it was very difficult to position the model to result in a good penetration of the center of the vortex, as had been seen at the previous lower vortex strengths. Additionally, recovery was complicated by the lack of climb performance capability when the model was positioned between the generating-wing vortex pair. Figure 24 shows a high-to-low vortex penetration. The trajectory shows that the model was initially pushed slightly to the left; then, right controls were applied to attempt an intersection with the vortex core and fuselage. Typically, in these flights, the model still slightly missed flying directly through the vortex core. Other than the positioning problems, the encounter was similar to what had been experienced at the previous vortex strengths. Figure 25 shows a low-to-high vortex penetration. The trajectory of the model shows a large perturbation to the left after the encounter. Roll controls were saturated for a long period. This penetration geometry was repeated several times, and some of the penetrations resulted in the model being recovered by the safety cable operator after going out of control and exceeding the wind tunnel test section envelope. Pilot comments indicated that control of the airplane through the vortex was much more difficult, and confidence was low on the ability to retain control of the model. Another interesting note is that control seemed more in question at this vortex strength for vertical penetrations, whereas at lower vortex strengths, it was felt that the lateral penetrations were more hazardous.

Figures 26 through 28 show data for vortex encounters with $C_{L_g} = 1.25$. Several attempts were made to cross the vortex from right to left. Figure 26 shows one of these penetration attempts. As the trajectory plot shows, the model did not pass through the vortex. The upwash field on the right side of the vortex induced more right roll than was available through the controls. The data showed full left lateral controls while the model was moving away from the vortex to the right. The wingtip probe showed that it apparently crossed the vortex core briefly during the encounter attempt with the large increase in upwash followed by downwash when the

wingtip probe went through the vortex core. Sideslip data showed a large negative sidewash approaching the core and positive sidewash once the wingtip probe was through the core. Pilot comments and video records showed that it was very hard to intersect the vortex core due to model interaction with the changing upwash field. Additionally, large translational rates were required to successfully penetrate through the vortex because of insufficient lateral control power to oppose the vortex-generated moments. Even with the faster rates, when the model was flown just below or just above the vortex, as marked by the smoke, it could translate across the vortex; however, when flown vertically, even with the vortex, it was not possible for the model to move horizontally past the vortex.

Vertical trajectories were flown through the vortex as shown in figures 27 and 28. Nearly every penetration resulted in large bank angles and large lateral displacements after encountering the vortex. As a result, nearly all encounters terminated with recovery on the safety cable after the model went out of control and exceeded the wind tunnel test envelope.

Vortex Encounter Data Trends

As previously mentioned, the primary objective of the current test was to determine whether the free-flight test technique could be used to fly a model in the presence of a wake vortex flow field. Because of the preliminary nature of the test, time constraints prevented an exhaustive data set with which to make statistically valid conclusions; however, the data may be analyzed to show some general trends.

The vortical flow field produced varying rolling moments on the model, depending not only on the vortex strength, but also on the relative position of the model and the wake vortex system. An example of the rolling moment produced by the vortex on the model, as a percent of roll control power available, is shown in figure 29 for a C_{L_g} = 1.18. This figure is a combination of all dynamic data available when the model was at approximately the 0° radial location from the reference vortex position. The data show a slightly increasing right rolling moment as the model gets closer to the vortex, with a maximum occurring at about 50 in. (approximately one half the span of the following model) from the vortex. For example, as presented in reference 20, these trends are consistent with general rolling moment predictions for this span ratio. At the maximum, the roll requirement is approximately 70 percent of the available roll control available. As the model moves nearer to the vortex reference position, the control requirement rapidly shifts to a left rolling moment due to the vortex, which exceeds the roll capability of the model as it approaches the vortex. Note that the percentage of roll control power available in figure 29 is estimated based on aileron effectiveness measured in a static wind tunnel test outside the influence of the wake vortex system.

To identify systematically the effects of flight through a wake vortex as the vortex strength was increased, data were obtained from all vertical trajectory vortex encounters. The horizontal encounter data were not included due to the large amounts of scatter attributable to differences in pilot technique between runs. One proposed measure of identifying wake vortex hazard is by quantifying maximum allowable bank angle excursions. Reference 21 proposes a maximum bank angle upset of 7° as being the maximum for safe acceptable operations during the final part of the approach. Free-flight results of bank angle perturbations, as a result of encounters with vortex wakes of various strengths, are shown in figure 30. The data indicate that by using the criteria of reference 21, a maximum C_{L_g} of approximately 0.95 would be allowable. Note that these tests were flown with a control system with relatively high-gain feedback loops that respond more rapidly to upsets than a pilot would in a typical business jet aircraft. Therefore, the comparison with reference 21 criteria is for illustrative purposes only.

Another indicator which will be a key pilot-observed response is the roll rate generated by a vortex encounter. Figure 31 shows the roll rates, converted to full-scale values, which would be experienced during encounters with vortices of various strengths. These values compare with a maximum roll rate achievable by the airplane, in free air, of approximately 33.5°/sec (dampers off). In addition to bank angle upsets, significant lateral displacements occur as a result of a vortex encounter. The lateral displacements are particularly undesirable on a precision approach to landing where very accurately flown ground track paths are required. Figure 32 shows the maximum lateral translation velocities across the ground that occurred during the tests. The data show uncommanded lateral velocities up to 20 percent of the approach velocity.

Conclusions

A wind tunnel study was conducted to determine the feasibility of using the free-flight test technique to study wake vortex encounters. A generic business class jet airplane model was instrumented and flown in the vicinity of a wake vortex generated by a rectangular wing. The strength of the vortex was varied by adjusting the generating-wing angle of attack and allowed study of a range of generating-airplane pairs (with span ratios of 0.75) and separation distances without the uncertainties in vortex decay and atmospheric effects. The study

showed that the free-flight test technique was a viable and useful tool in the study of wake vortex encounters—combining vortex flow fields, airplane dynamics, sensors, and flight control aspects.

Data obtained during this test included qualitative and quantitative results. The test indicated that although each of the longitudinal control schemes provided an easy-to-fly airplane, the g-command system reduced the longitudinal upsets slightly more than the pitch rate or angle-of-attack command systems. Steady-state limits of controllability during flight were documented as a function of vortex strength. These data showed limits of controllability for steady flight to be at a vortex strength corresponding to a lift coefficient of approximately 0.7 on the generator wing. By flying several vortex encounter trajectories at high vortex strengths, a mapping of roll angle, roll rate, lateral velocity, and vortex-induced roll rate acceleration was conducted. The data quantified the effects of an airplane entering vortex flow fields of varying strengths, and just as importantly, demonstrated the ability to fly safely and to recover from scale-model wake encounters in a confined test area. Pilot comments indicated that the selected flight trajectory through the vortex and the vortex strength affected the perceived difficulty of maintaining control. Specific conclusions reached are as follows:

1. The free-flight test technique can be used to fly a model in the vicinity of and to conduct encounters with a vortex generated from upstream models.

2. Accurate model and vortex-positioning data during flight can be derived by using postflight photogrammetry measurement techniques.

3. Mapping of approximate induced rolling moment due to the vortex flow field can be conducted.

4. Effects of vortex encounters on airplane model responses can be measured and repeated in well-controlled conditions with known vortex strengths. Results showed vertical trajectories to be the most demanding for encounters with high-strength vortices, and lateral penetrations were the most demanding at lower vortex strengths.

NASA Langley Research Center
Hampton, VA 23681-2199
June 12, 1997

Appendix

Control Laws for Follower Model

Basic Considerations

The flight control laws for the model were developed to provide good flying qualities for flying a model in the wind tunnel. The operational envelope modeled during the tests was the landing-final approach configuration at low speed and sea level altitude. The control laws were implemented on a digital minicomputer using an update rate of 200 iterations/sec. All flight control system gains could be modified in flight by a computer operator. Selected flight control system switches and gain paths could be activated by switches on the pilot control boxes. Block diagrams of the flight control laws are shown in figures A1 through A4. Switch default values and gain values shown in the figures correspond to the baseline (g-command) system used throughout most of the testing.

Longitudinal Axis

There were several control law options in each of the lateral and longitudinal axes. The longitudinal axes had either proportional or proportional plus integral modes using either normal acceleration or pitch rate in the integrator. The feedback gains for pitch rate, angle of attack, and normal acceleration could be adjusted in flight.

Angle-of-attack command mode. The angle-of-attack command mode was the most simple control law scheme. This mode bypassed the integrator by setting a switch to zero. The only parameter in the feedback loop with the α command system was pitch rate. The pitch pilot had the option of adding normal acceleration feedback, removing pitch rate feedback, or adding α feedback for static stability augmentation by using either one or both of the wingtip boom vanes. The pitch pilot could change these parameters with switches on the pitch control box during a flight.

Pitch rate command mode. The pitch rate command mode was entered by selecting a switch on the pitch pilot control box. This command mode combined the pitch rate and pilot command signals through a forward path integrator. Additional proportional feedback of pitch rate was added after the integrator. This mode changed the pilot input commands to represent pitch rate commands, and with centered stick, it was essentially a pitch attitude hold system.

g-command mode. The g-command mode was selected by switches on the pitch pilot control box. This mode combined the pilot commands with normal acceleration through the forward path integrator. Proportional pitch rate feedback was used outside the integrator. With centered control stick, this mode attempted to maintain 1g flight and resulted in a more lively model than the previous modes. Pitch rate damping was increased to provide better flying qualities.

Lateral-Directional Axes

The lateral-directional control laws included an aileron-to-rudder interconnect (ARI) so that one pilot could fly the roll-yaw axes of the airplane with one control. Switches on the roll-yaw pilot control box enabled selection of roll rate, yaw rate, side acceleration, or sideslip from one or both wingtip booms to be selected as feedbacks during flight. Additionally, differential signals of angle of attack between the two wingtip mounted vanes could be used as a feedback.

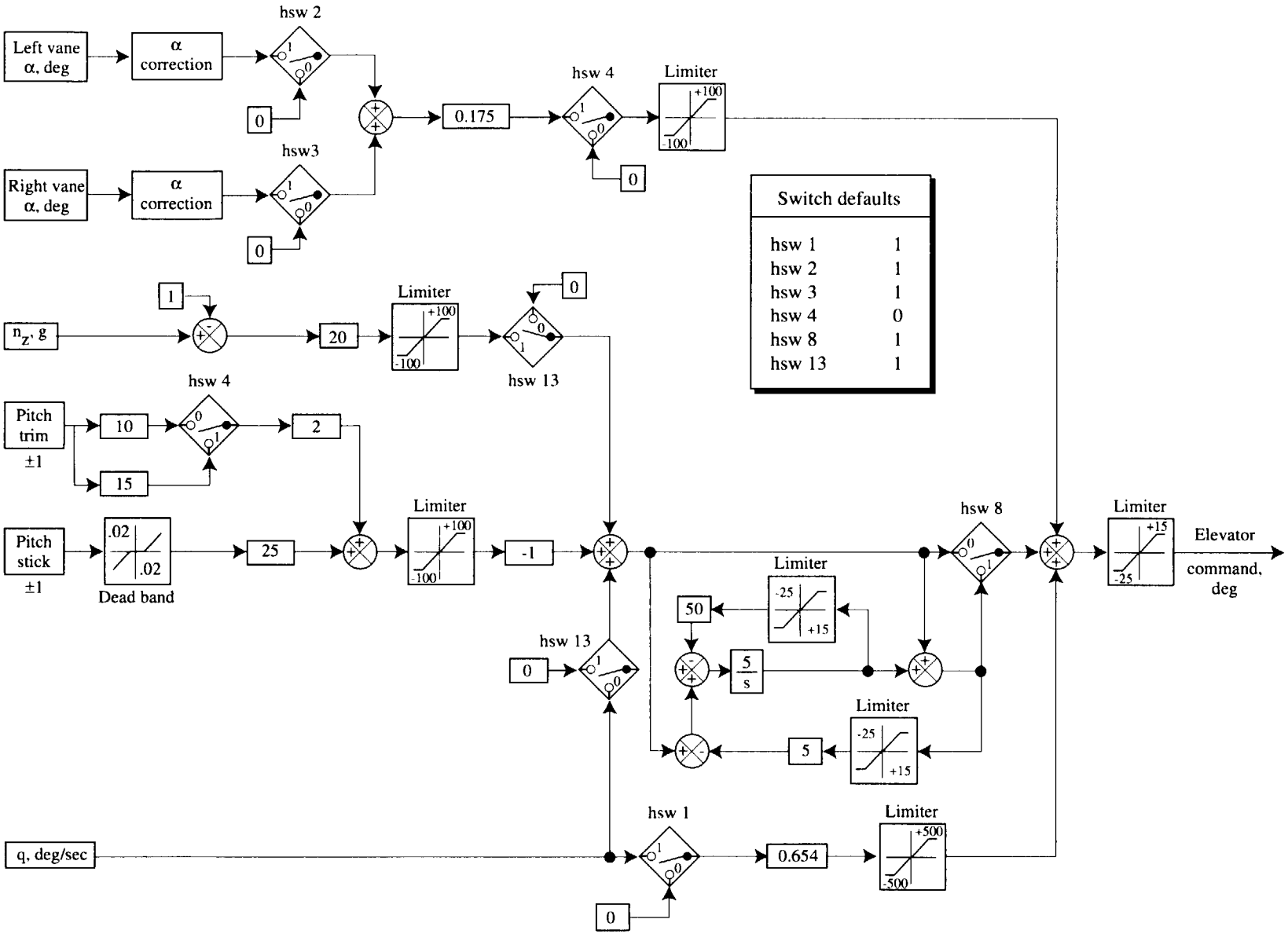

Figure A1. Model longitudinal control laws.

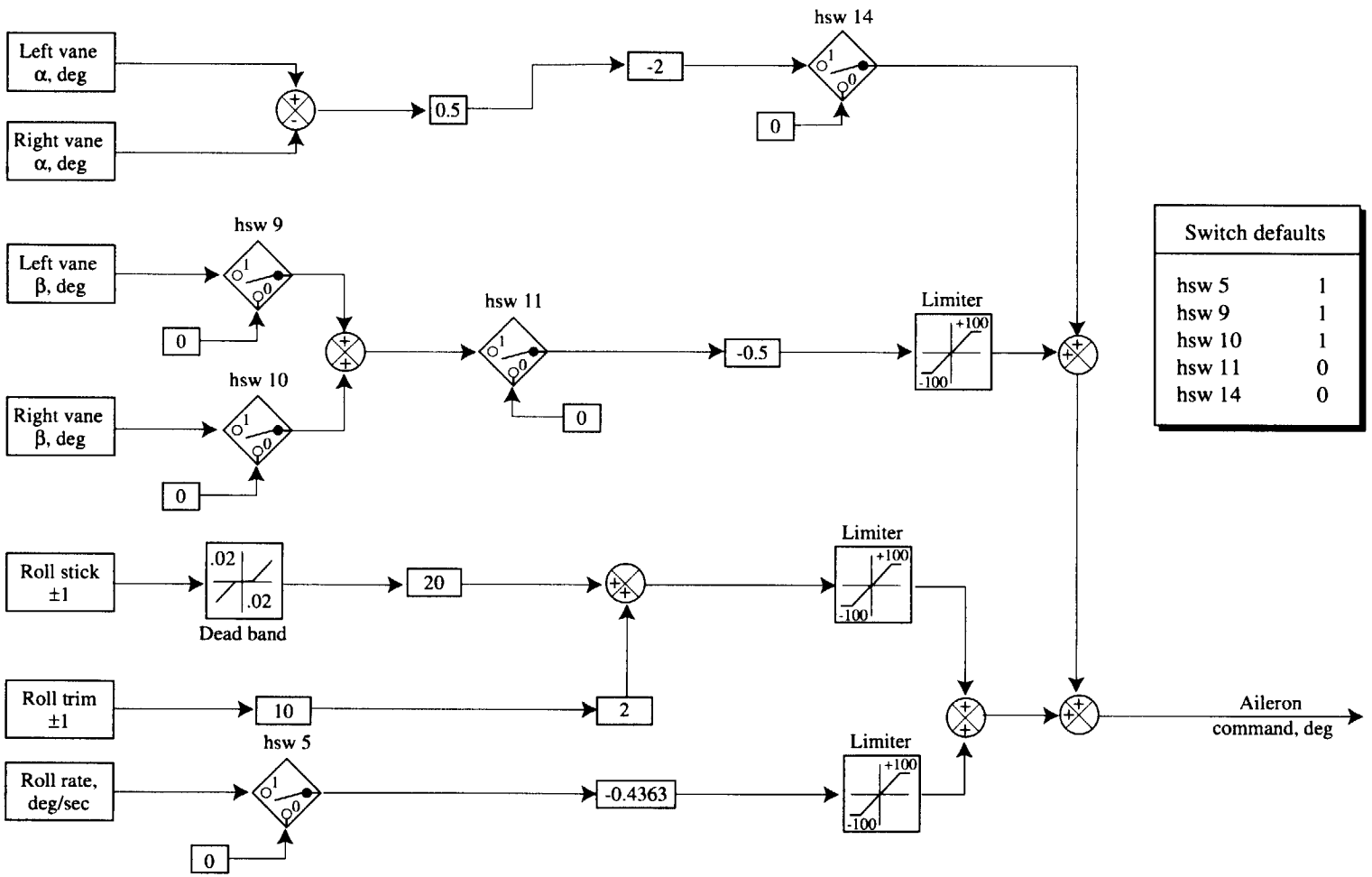

Figure A2. Model lateral control laws.

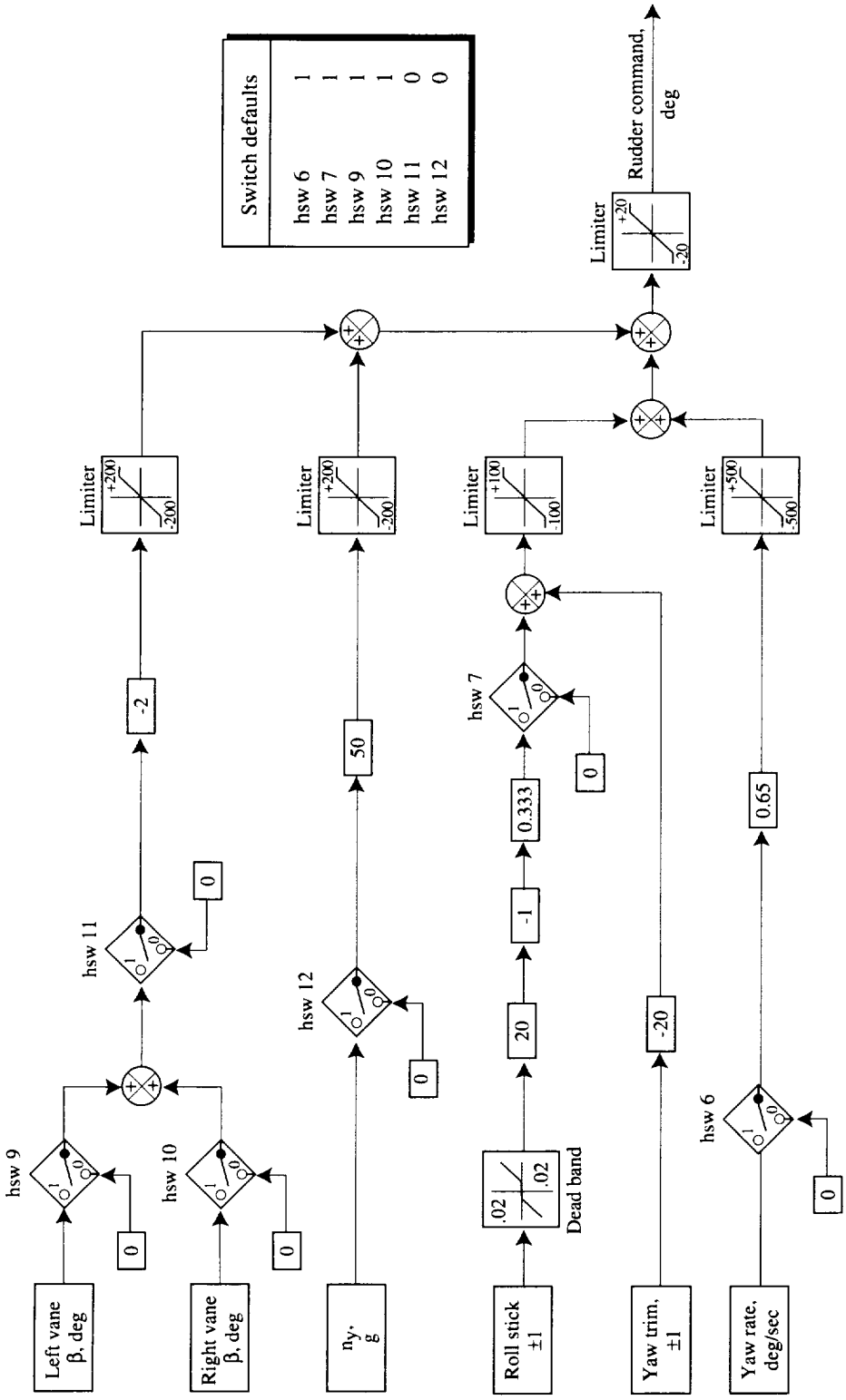

Figure A3. Model directional control laws.

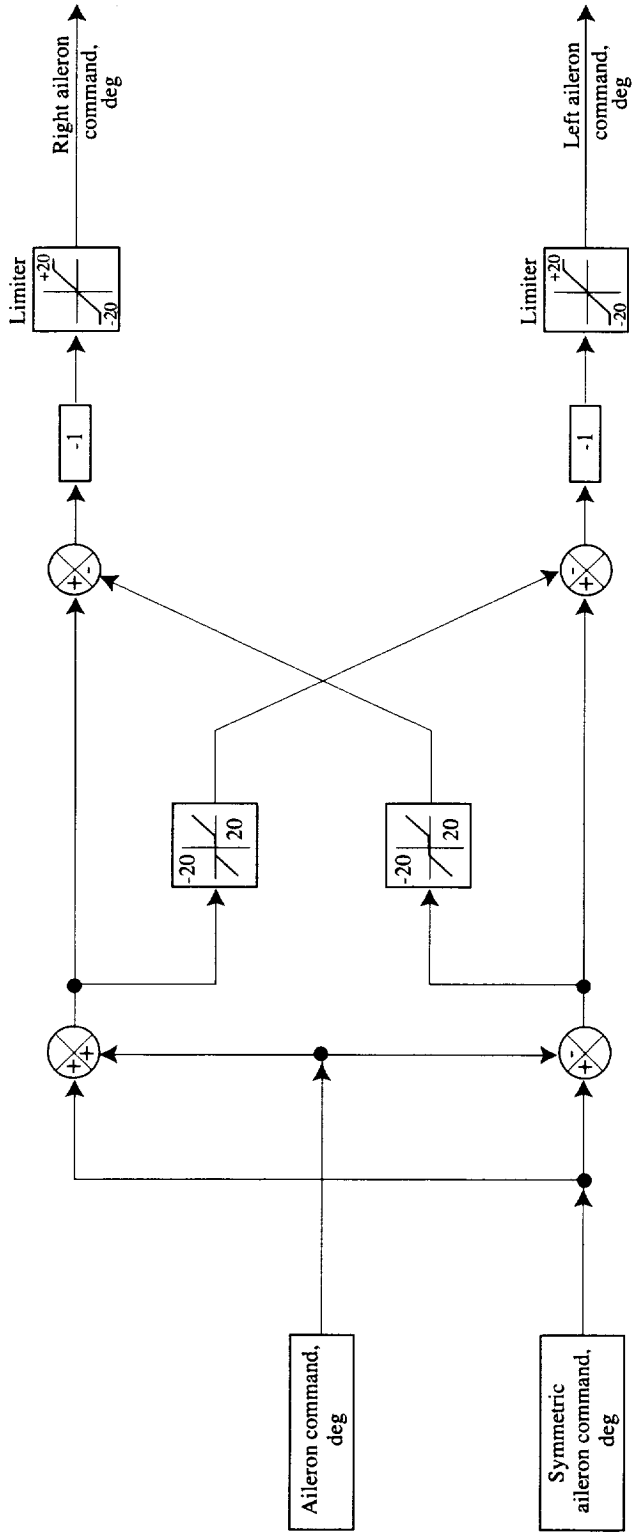

Figure A4. Aileron combiner. Note: All data reported herein used zero symmetric aileron command.

References

1. Hinton, David A.: *Aircraft Vortex Spacing System (AVOSS) Conceptual Design*. NASA TM-110184, 1995.

2. Rossow, V. J.: Inviscid Modeling of Aircraft Trailing Vortices. *Wake Vortex Minimization*, NASA SP-409, Feb. 1976, pp. 9–60.

3. Bilanin, A. J.; Teske, M. E.; Donaldson, C.; and Snedeker, R. S.: Viscous Effects in Aircraft Trailing Vortices. *Wake Vortex Minimization*, NASA SP-409, Feb. 1976, pp. 61–128.

4. Lee, T.; and Lan, C. E.: Navier-Stokes Calculation of Wing Wake Structure. AIAA-94-1882, June 1994.

5. McGowan, W. A.: *Calculated Normal Load Factors on Light Heavy Transport Airplanes*. NASA TN D-829, 1961.

6. McMillian, O. J.; Schwind, R. G.; Nielsen, J. N.; and Dillenius, M. F. E.: *Rolling Moments in a Trailing Vortex Flow Field*. NASA CR-151961, 1977.

7. Stuever, Robert A.; and Greene, George C.: An Analysis of Relative Wake-Vortex Hazards for Typical Transport Aircraft. AIAA-94-0810, Jan. 1994.

8. Garodz, L. J.; Lawrence, D. M.; and Miller, N. J.: *Measurement of the Trailing Vortex Systems of Large Transport Aircraft, Using Tower Fly-by and Flow Visualization—Summary, Comparison and Application*. FAA-RD-75-127, Jan. 1976. (Available from DTIC as AD A021305/8.)

9. Brashears, M. R.; and Zalay, A. D.: Laser Doppler Velocimeter Measurements of B-747 Wake Vortex Characteristics. *Proceedings of the Aircraft Wake Vortices Conference*, J. N. Hallock, ed., FAA, Mar. 1977. (Available from DTIC as AD A055510.)

10. Smith, H. J.: *A Flight Test Investigation of the Rolling Moments Induced on a T-37B Airplane in the Wake of a B-747 Airplane*. NASA TM X-56031, 1975.

11. Rossow, V. J.; Sacco, J. N.; Askins, P. A.; Bisbee, L. S.; and Smith, S. M.: Measurements in 80- by 120-Foot Wind Tunnel of Hazard Posed by Lift-Generated Wakes. AIAA-93-3518, Aug. 1993.

12. Rossow, Vernon J.: Wake-Vortex Structure From Lift and Torque Induced on a Following Wing. AIAA-93-3013, July 1993.

13. Greene, G. C.: An Approximate Model of Vortex Decay in the Atmosphere. *J. Aircr.*, vol. 23, July 1986, pp. 566–573.

14. Somers, D. M.: *Design and Experimental Results for a Flapped Natural-Laminar-Flow Airfoil for General Aviation Applications*. NASA TP-1865, 1981.

15. Coe, Paul L., Jr.; Turner, Steven G.; and Owens, D. Bruce: *Low-Speed Wind-Tunnel Investigation of the Flight Dynamic Characteristics of an Advanced Turboprop Business/Commuter Aircraft Configuration*. NASA TP-2982, 1990.

16. Ciffone, D. L.; and Orloff, K. L.: Application of Laser Velocimetry to Aircraft Wake-Vortex Measurements. *Wake Vortex Minimization*, NASA SP-409, Feb. 1976, pp. 157–192.

17. Riley, Donald R.; Brandon, Jay M.; and Glaab, Louis J.: *Piloted Simulation Study of an ILS Approach of a Twin-Pusher Business/Commuter Turboprop Aircraft Configuration*. NASA TM-4516, 1994.

18. Childers, Brooks A.; Snow, Walter L.; Jones, Stephen B.; and Franke, John M.: Support of Wake Vortex Detection Research in Flight and Wind Tunnel Testing Using Videometric Techniques. Paper presented at *ISPRS Commission V Intercongress Symposium*, Mar. 1994.

19. Military Specification: Flying Qualities of Piloted Airplanes. MIL-F-8785C, Nov. 1980.

20. Rossow, Vernon J.; and Tinling, Bruce E.: Research on Aircraft/Vortex-Wake Interactions to Determine Acceptable Level of Wake Intensity. *J. Aircr.*, vol. 25, June 1988, pp. 481–492.

21. Sammonds, Robert I.; Stinnett, Glen W., Jr.; and Larson, William E.: Criteria Relating Wake Vortex Encounter Hazard to Aircraft Response. *J. Aircr.*, vol. 14, no. 10, Oct. 1977, pp. 981–987.

Table I. Geometric and Mass Characteristics of Follower Model

Geometric characteristics:	
Fuselage:	
Length, ft	7.833
Maximum diameter, in.	11.2
Wing:	
Area (trapezoidal reference), ft^2	9.869
Span, ft	9.072
Quarter-chord sweep, deg	1.41
Aspect ratio	8.3
Taper ratio (trapezoidal reference)	0.35
Mean aerodynamic chord, in.	14.172
Dihedral, deg	4.0
Horizontal tail:	
Area, ft^2	2.067
Span, ft	3.211
Aspect ratio	4.988
Quarter-chord sweep, deg	31.6
Dihedral, deg	−3.0
Taper ratio	0.35
Mean geometric chord, in.	8.324
Vertical tail:	
Area, ft^2	2.016
Height, in.	18.223
Quarter-chord sweep, deg	50.0
Mean geometric chord, in.	16.259
Mass characteristics:	
Weight, lb	92.5
Moment of inertia:	
I_X, slug-ft^2	4.636
I_Y, slug-ft^2	14.547
I_Z, slug-ft^2	16.666

Table II. Generating-Wing Vortex Strength

α_g	C_{L_g}	Γ_{ms}	Γ_{fs}
−6.0	−0.929	−8.80	−120.22
−4.0	.054	5.14	70.27
−2.0	.195	18.45	252.08
0.0	.360	34.08	465.46
2.0	.516	48.92	668.24
4.0	.669	63.36	865.45
6.0	.810	76.72	1048.03
8.0	.945	89.53	1222.99
10.0	1.071	101.50	1386.42
12.0	1.185	112.22	1532.91
13.4	1.247	118.13	1613.65

Table III. Dynamic Scaling Relationships

[In current test, $N = 0.175$]

Parameter	Model	Full scale
Time	$FS\sqrt{N}$	$\frac{MS}{\sqrt{N}}$
Linear velocity	$FS\sqrt{N}$	$\frac{MS}{\sqrt{N}}$
Linear acceleration	FS	MS
Angular velocity	$\frac{FS}{\sqrt{N}}$	$MS\sqrt{N}$
Angular acceleration	FS	MS
Weight	$\frac{N^3}{\sigma} \times FS$	$\frac{\sigma}{N^3} \times MS$
Moment of inertia	$\frac{N^5}{\sigma} \times FS$	$\frac{\sigma}{N^5} \times MS$
Dynamic pressure	$\frac{N}{\sigma} \times FS$	$\frac{\sigma}{N} \times MS$

Table IV. Test Setup Geometry

Component	Downstream distance, x/b_g
Generating-wing quarter-chord	
Laser 1	0.84
Laser 2	1.92
Laser 3	2.61

Table V. Sensor Accuracies and Resolution

Free-flight model sensors	Range	Accuracy	Resolution
Roll rate gyro	±200°/sec	±0.7°/sec	0.1°/sec
Yaw rate gyro	±200°/sec	±0.7°/sec	0.1°/sec
Pitch rate gyro	±200°/sec	±0.7°/sec	0.1°/sec
A_x accelerometer	±20g	±0.002g	0.01g
A_y accelerometer	±20g	±0.002g	0.01g
A_z accelerometer	±20g	±0.002g	0.01g
Boom α	−10° to 80°	[a]±2°	0.06°
Boom β	±30°	[a]±1°	0.03°
Aileron position	±30°	[a]±1°	0.02°
Elevator position	±30°	[a]±1°	0.03°
Rudder position	±30°	[a]±1°	0.03°

[a]Estimated based on repeated calibrations during test.

Table VI. Model Dynamic Characteristics

Parameter	Model scale, dampers on/off	Full scale, dampers on/off	Level I requirements (ref. 19)
τ_r, sec	0.24/0.38	0.56/0.89	<1.4
t_{30}, sec	0.98/0.69	2.35/1.65	<1.8
p_{ss}, deg/sec	40/80	16.7/33.5	

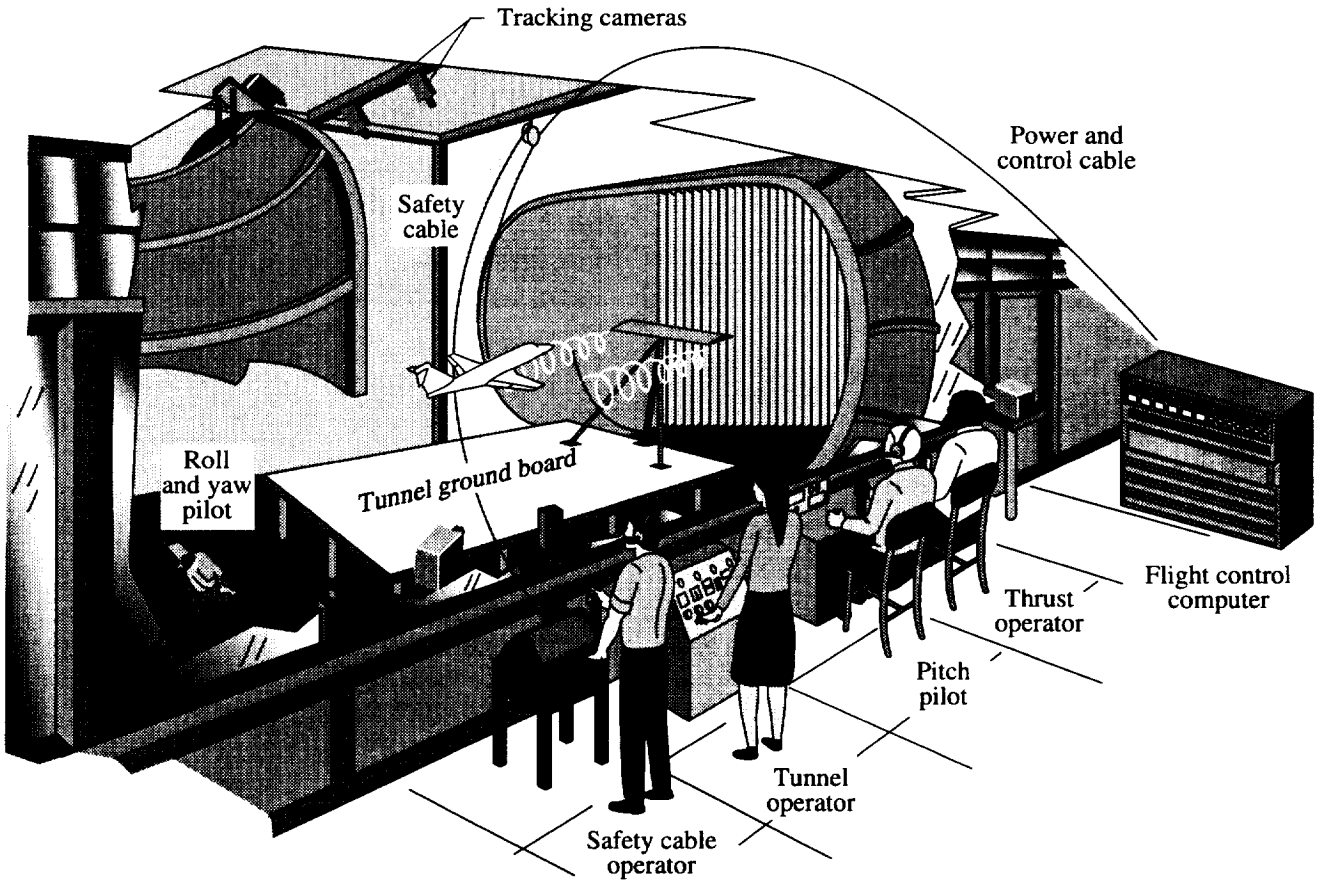

Figure 1. Sketch of free-flight test technique.

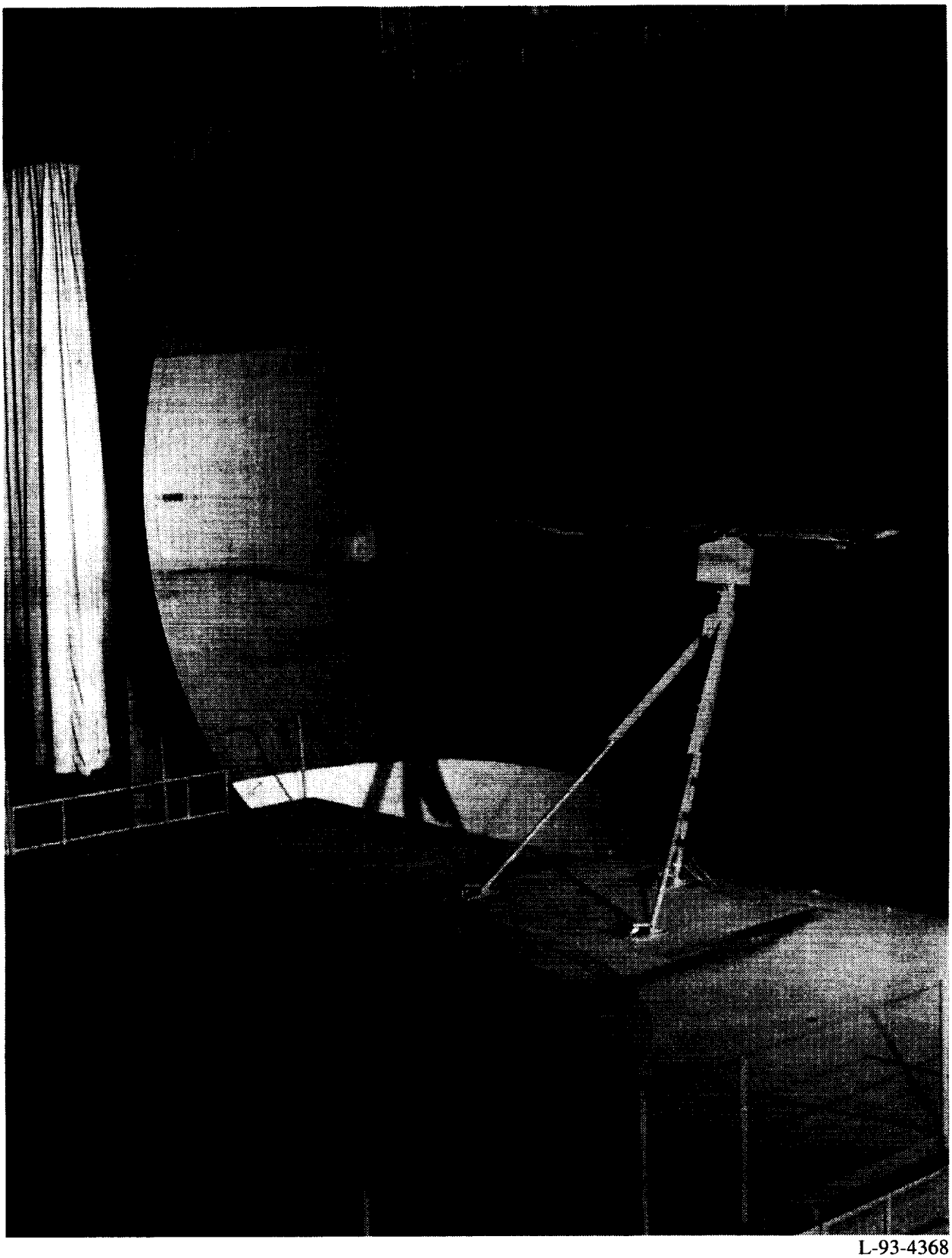

L-93-4368

Figure 2. Generating wing in Langley 30- by 60-Foot Tunnel.

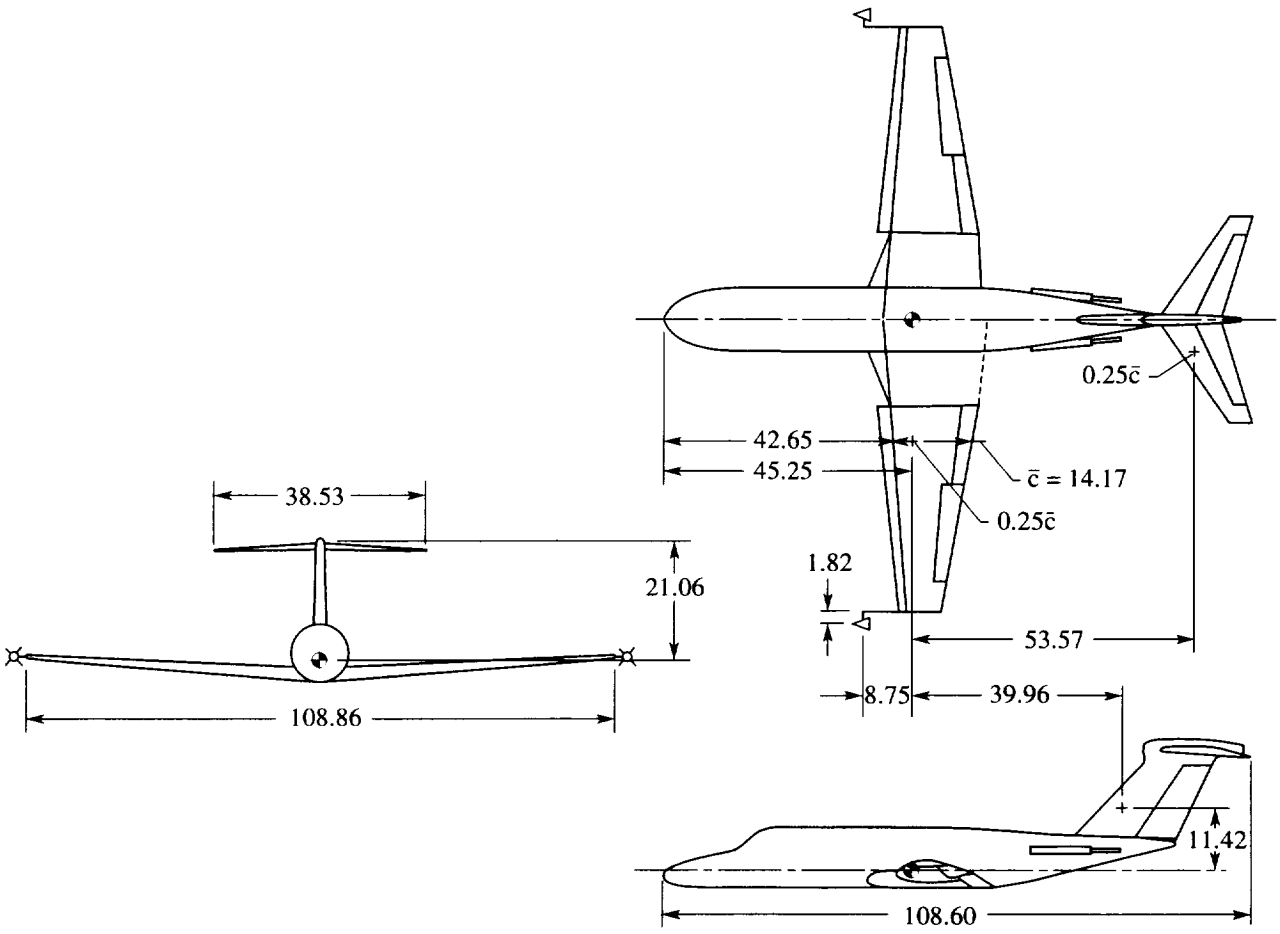

Figure 3. Free-flight model. Dimensions are in inches.

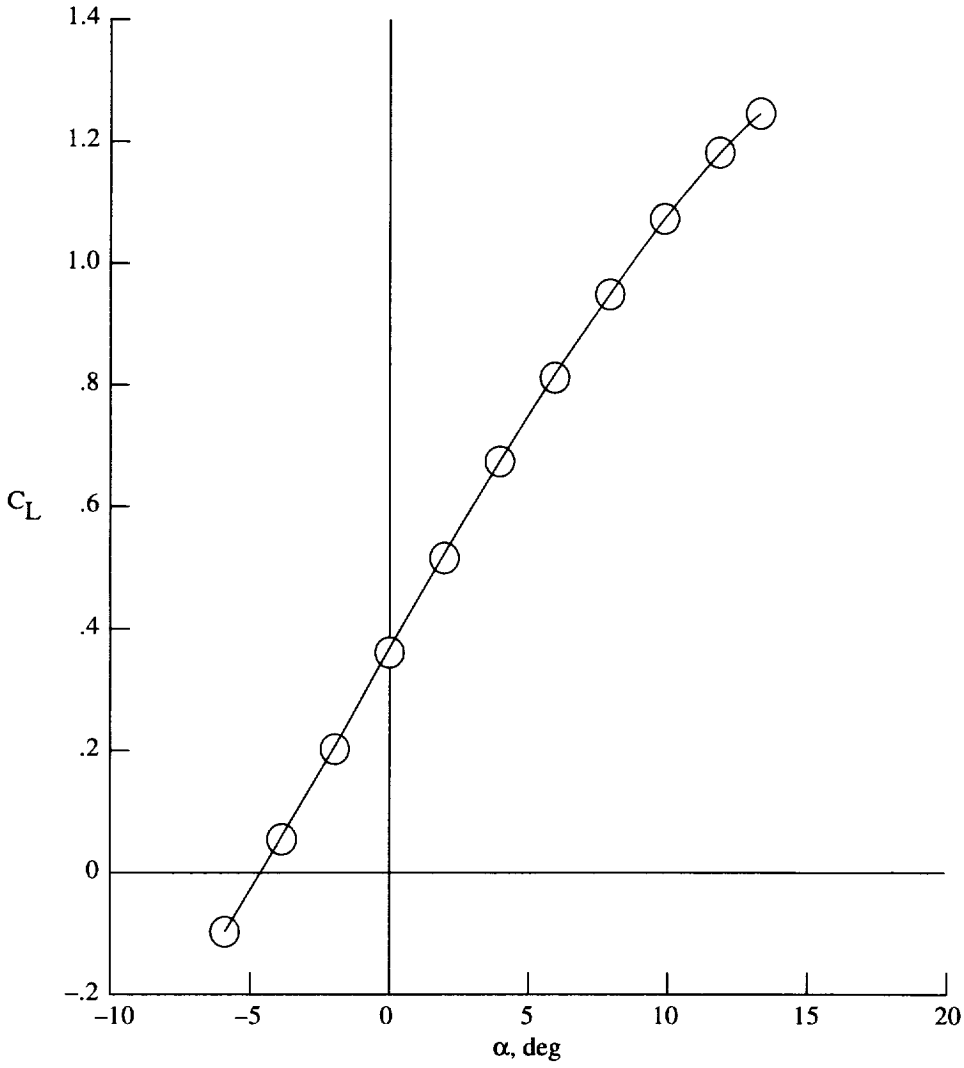

Figure 4. Generating-wing lift coefficient.

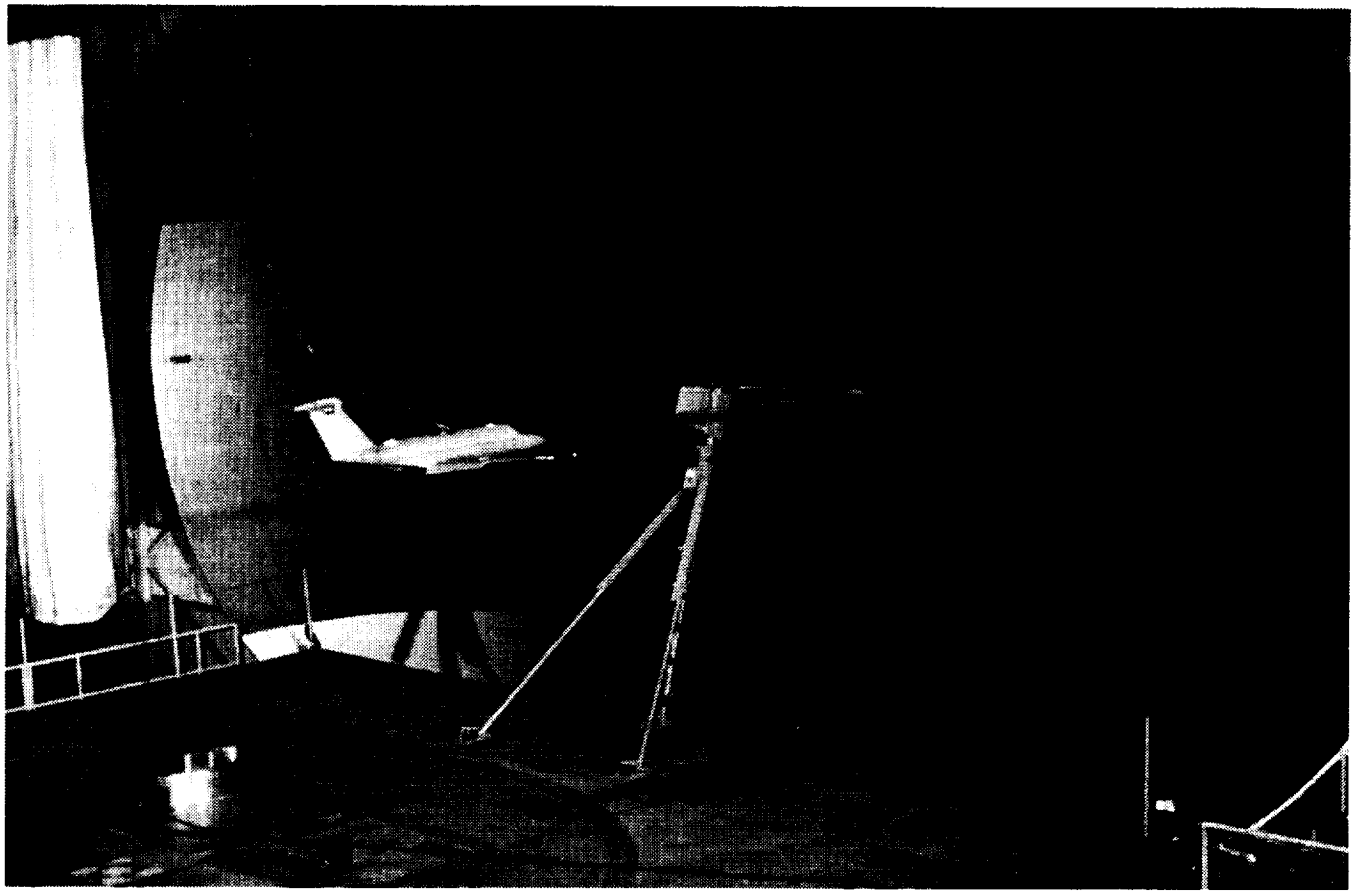

L-94-01277

Figure 5. Model in vortex during free-flight test.

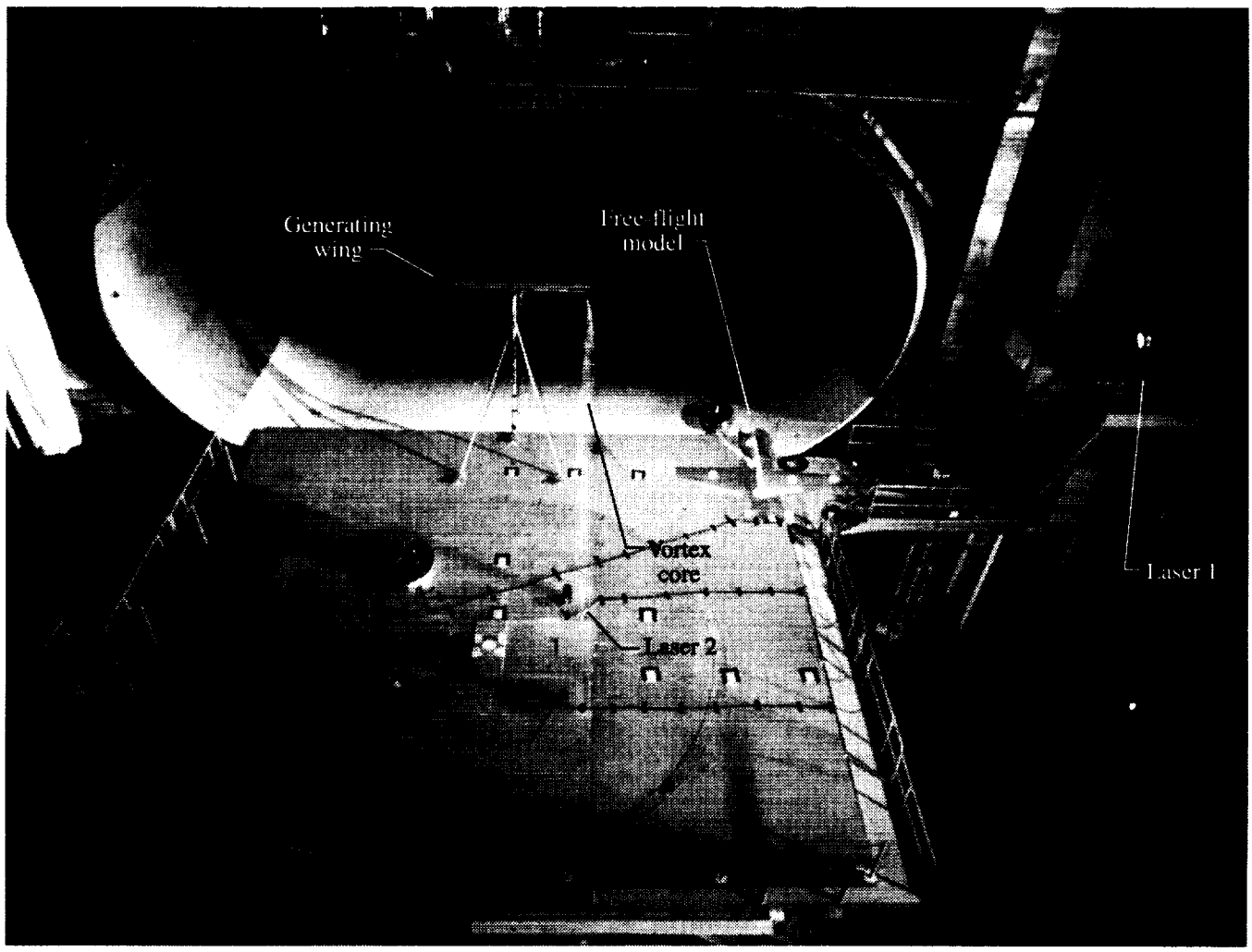

Figure 6. Wake vortex free-flight test setup.

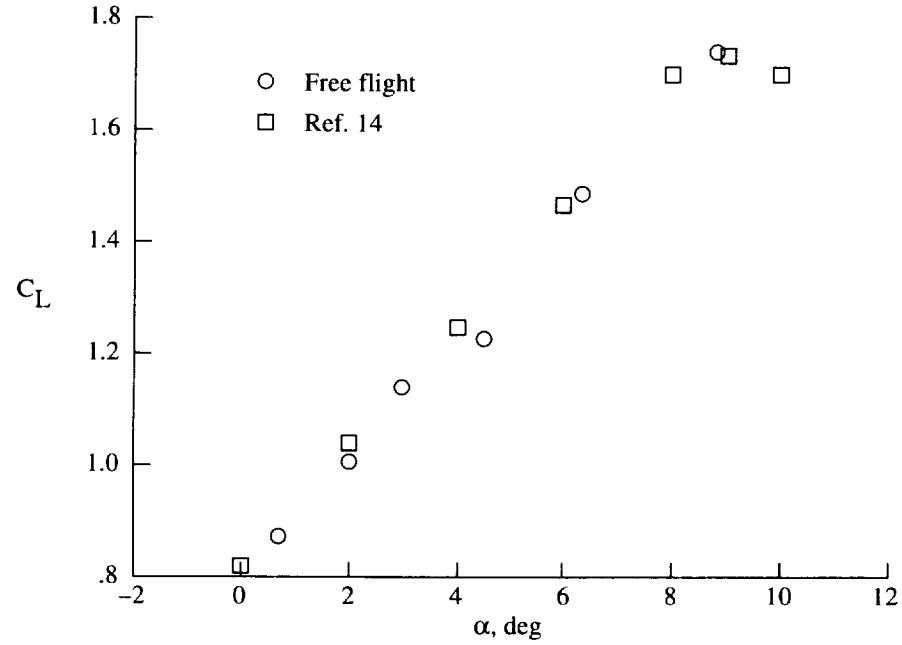

Figure 7. Flight-determined lift characteristics of free-flight model.

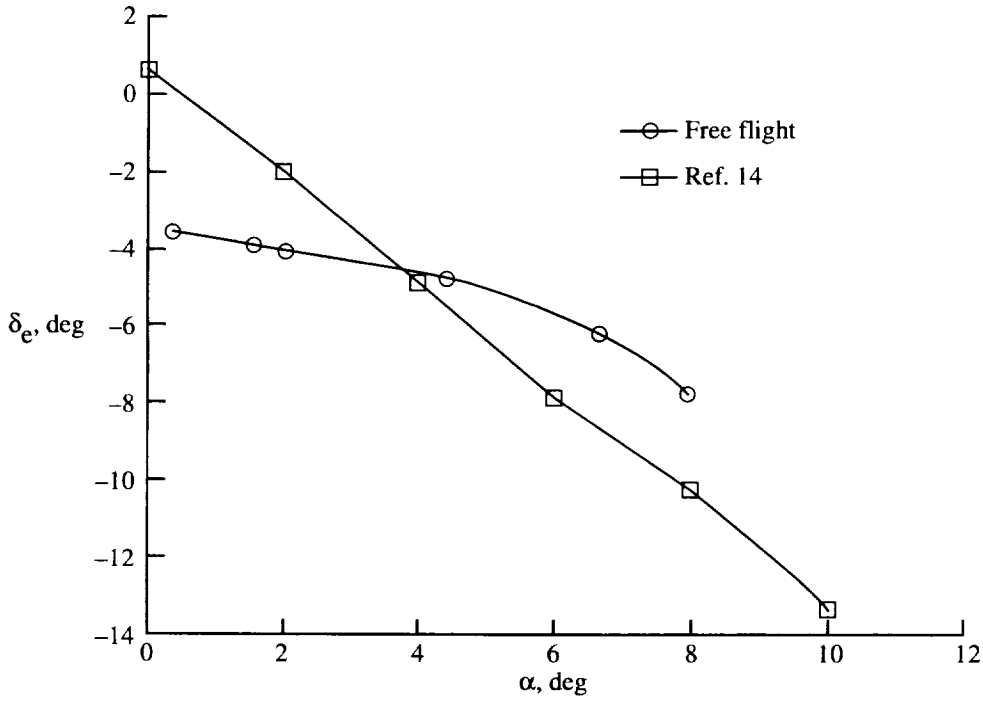

Figure 8. Trim tail settings in flight.

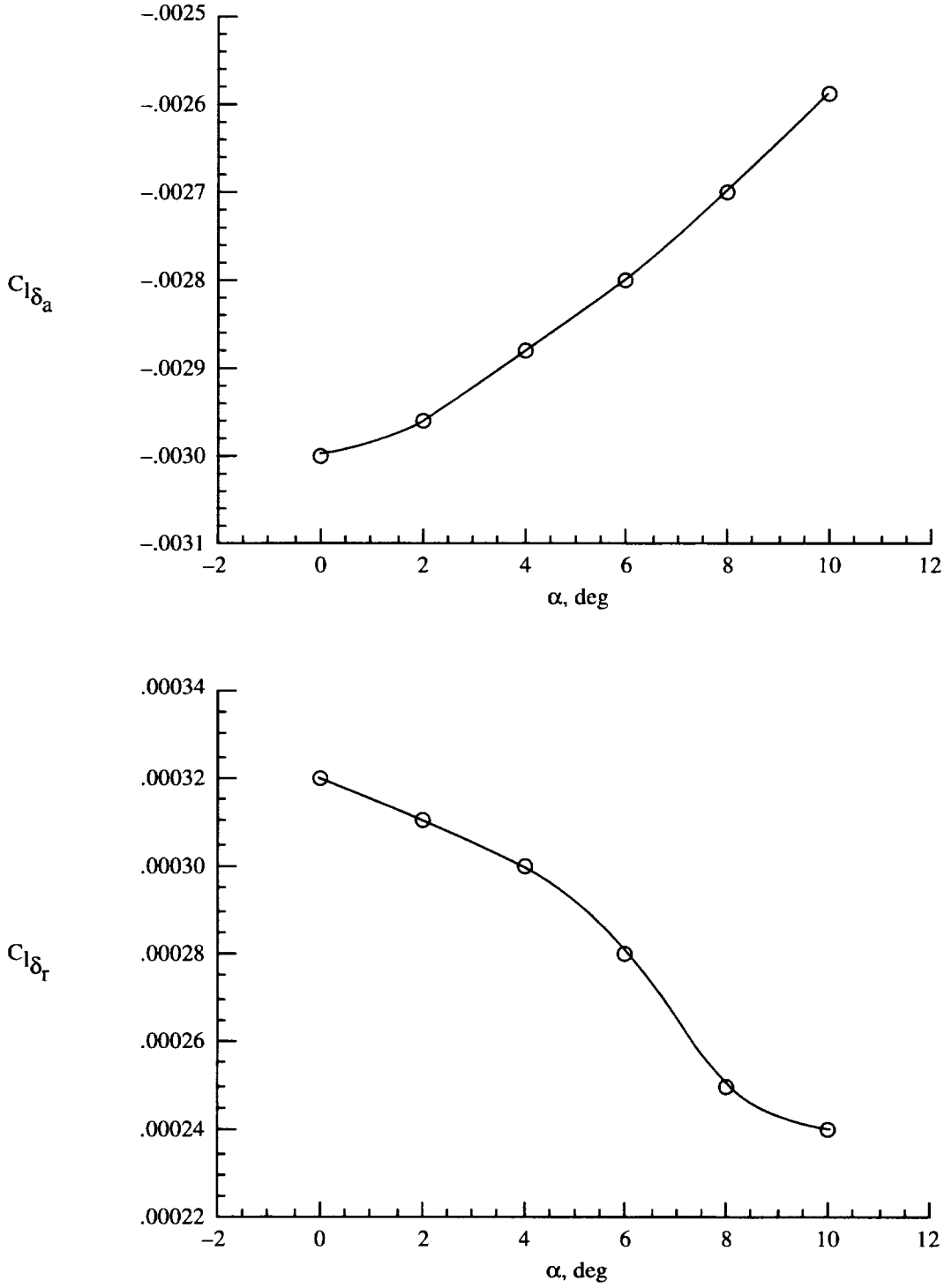

Figure 9. Roll control effectiveness (ref. 14).

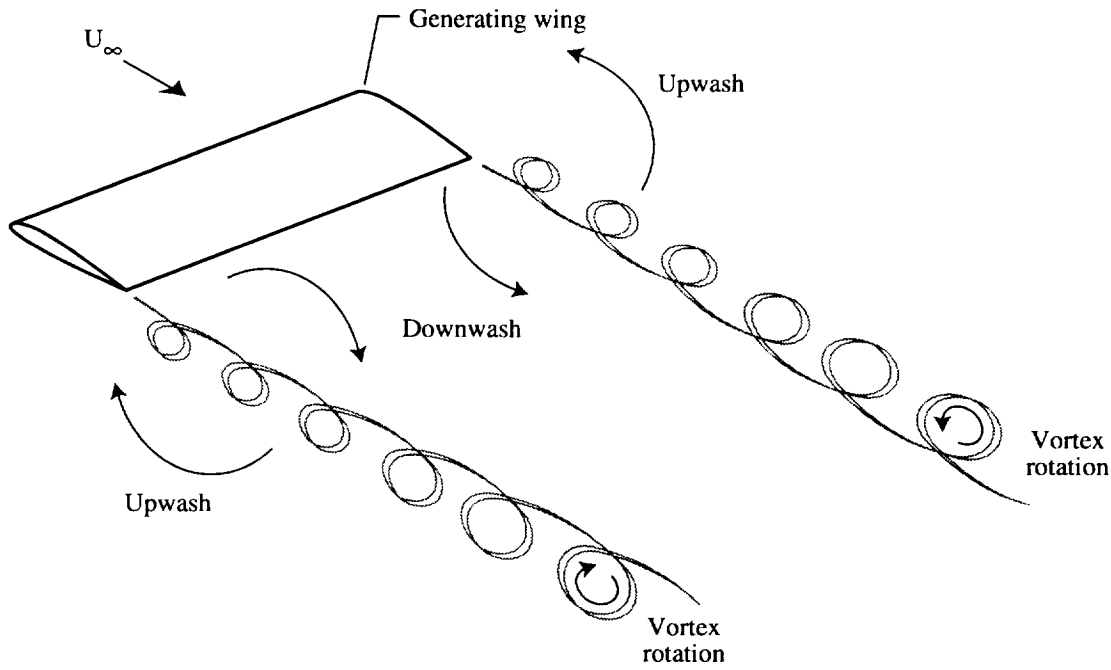

Figure 10. Flow-field schematic.

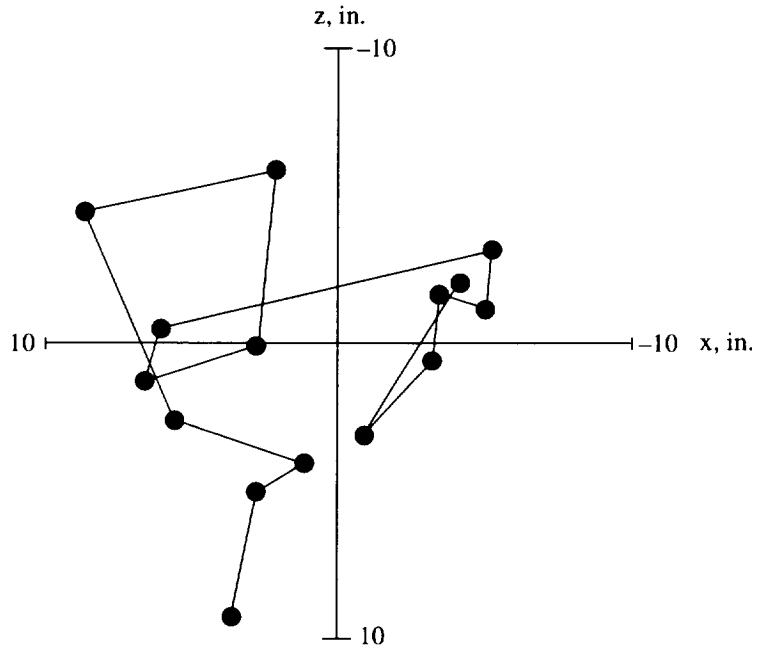

Figure 11. Photogrammetry-determined vortex position dynamics. Data span 0.5 sec; $\bar{q}$ = 5.3 psf.

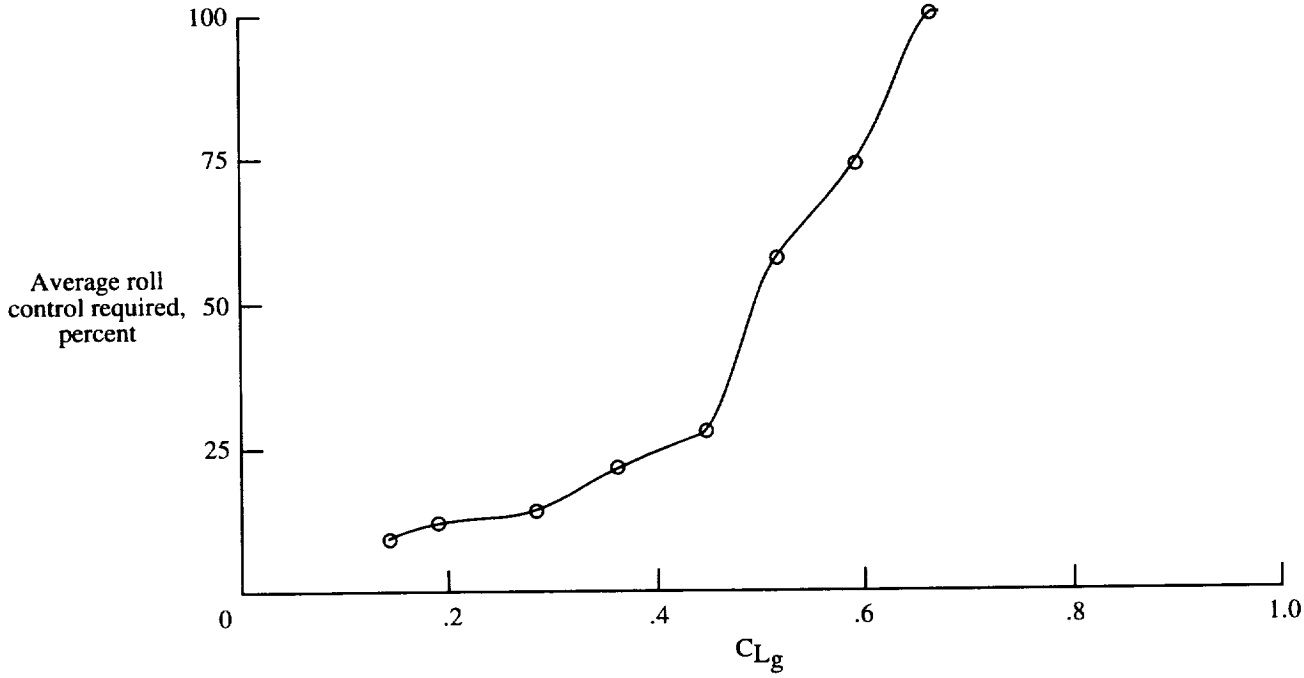

Figure 12. Roll control required for steady flight in vortex.

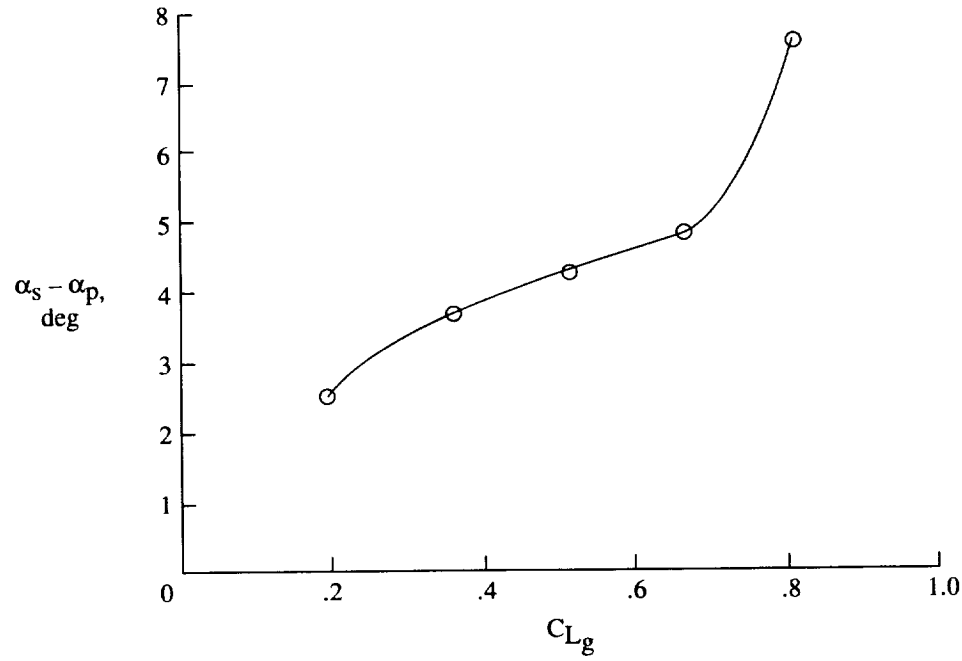

Figure 13. Vortex-induced differential angle of attack at wingtip probes while flying in center of vortex core.

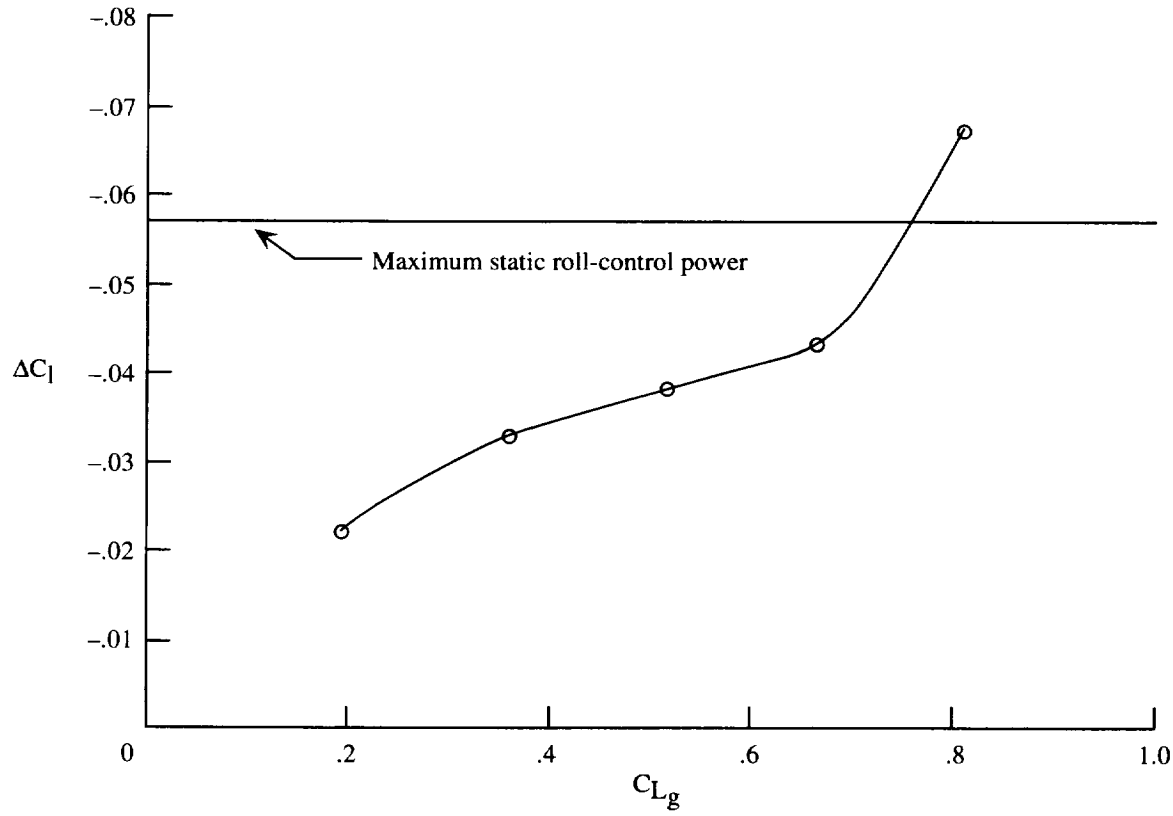

Figure 14. Linear prediction of rolling moment based on induced differential angle of attack at wingtips.

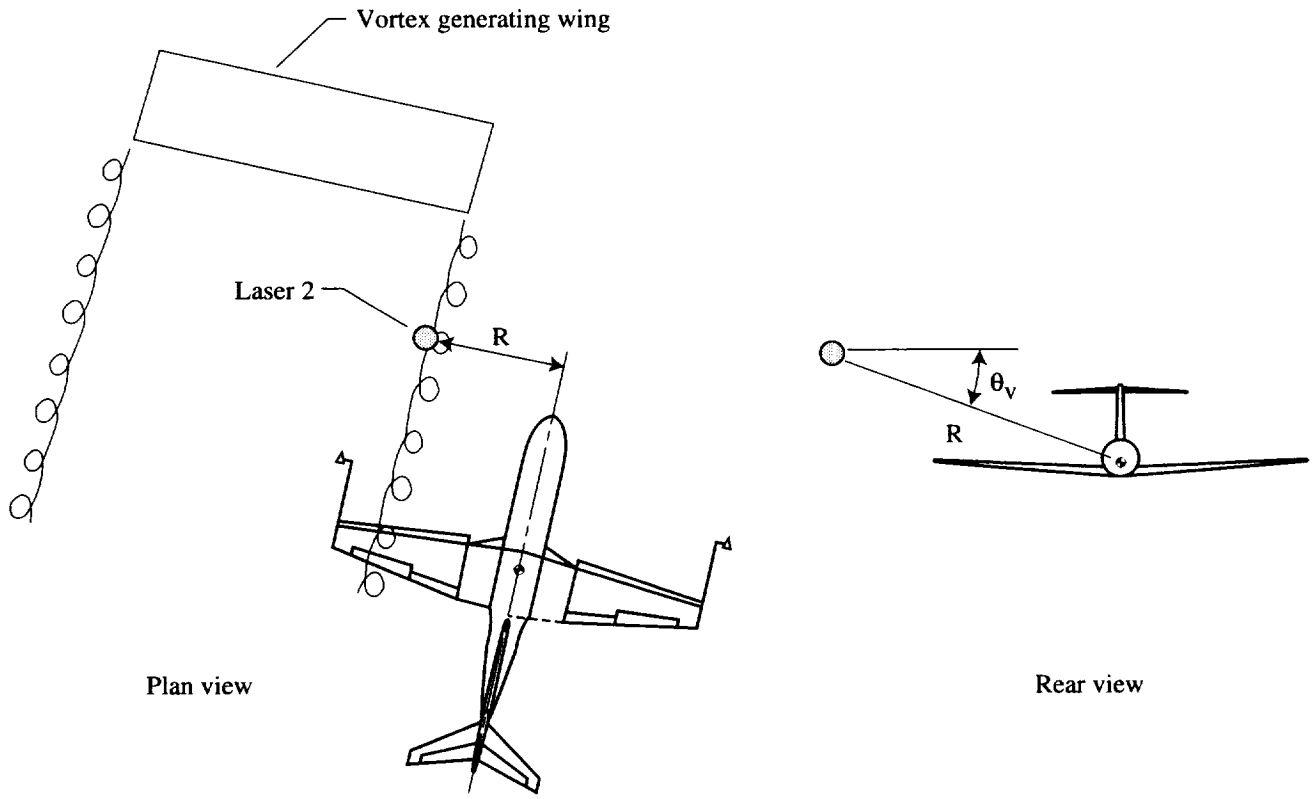

Figure 15. Sign convention for model location relative to vortex.

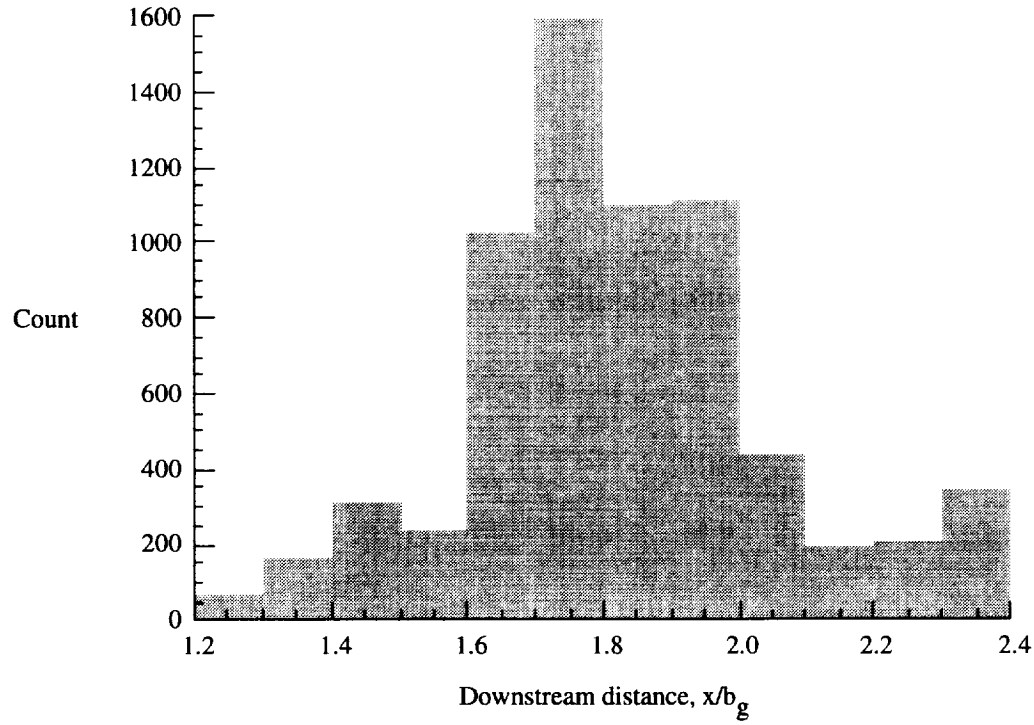

Figure 16. Histogram of downstream distance between model and generating wing. All runs included.

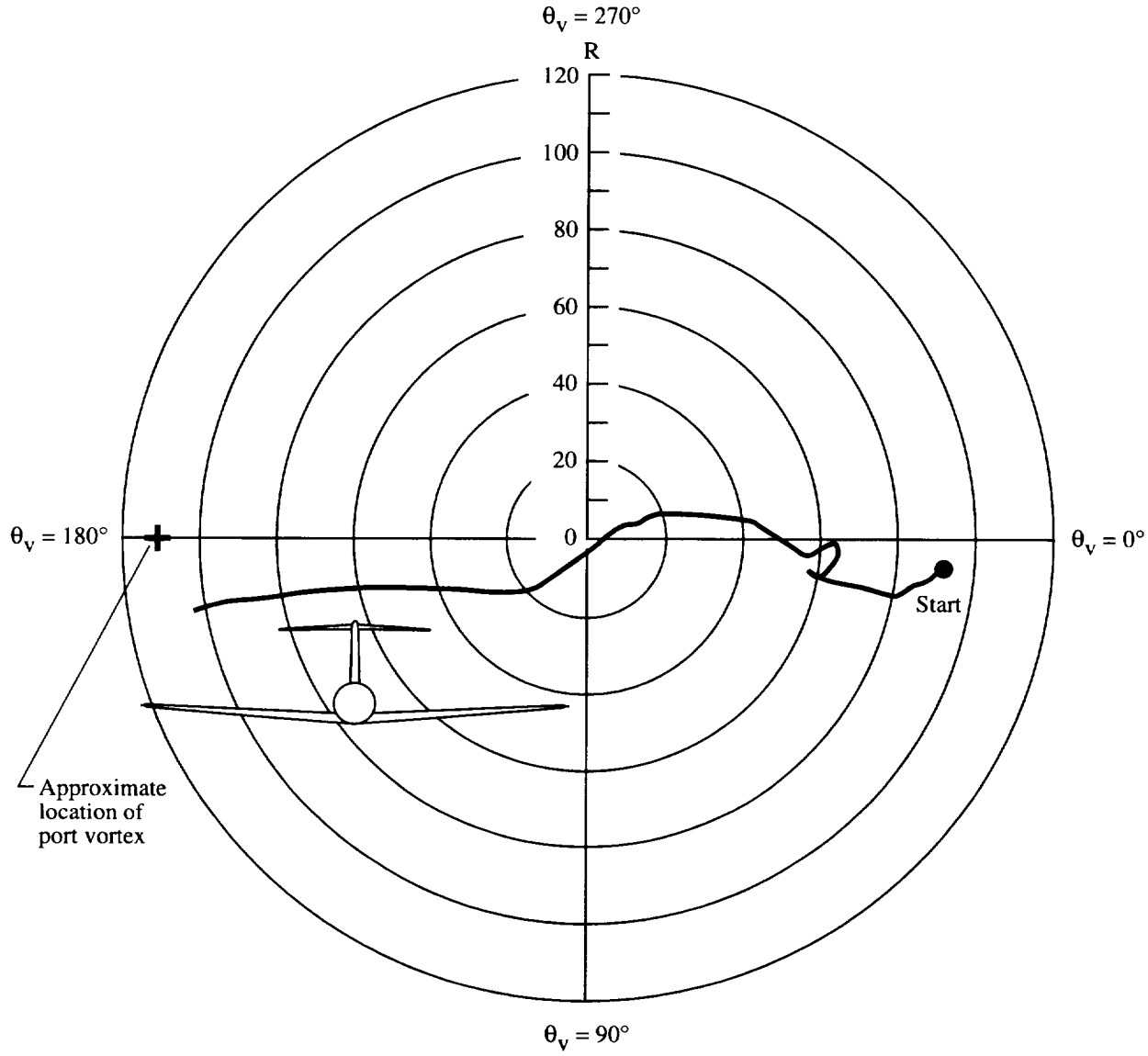

Figure 17. Right-to-left horizontal encounter. $C_{L_g} = 0.95$.

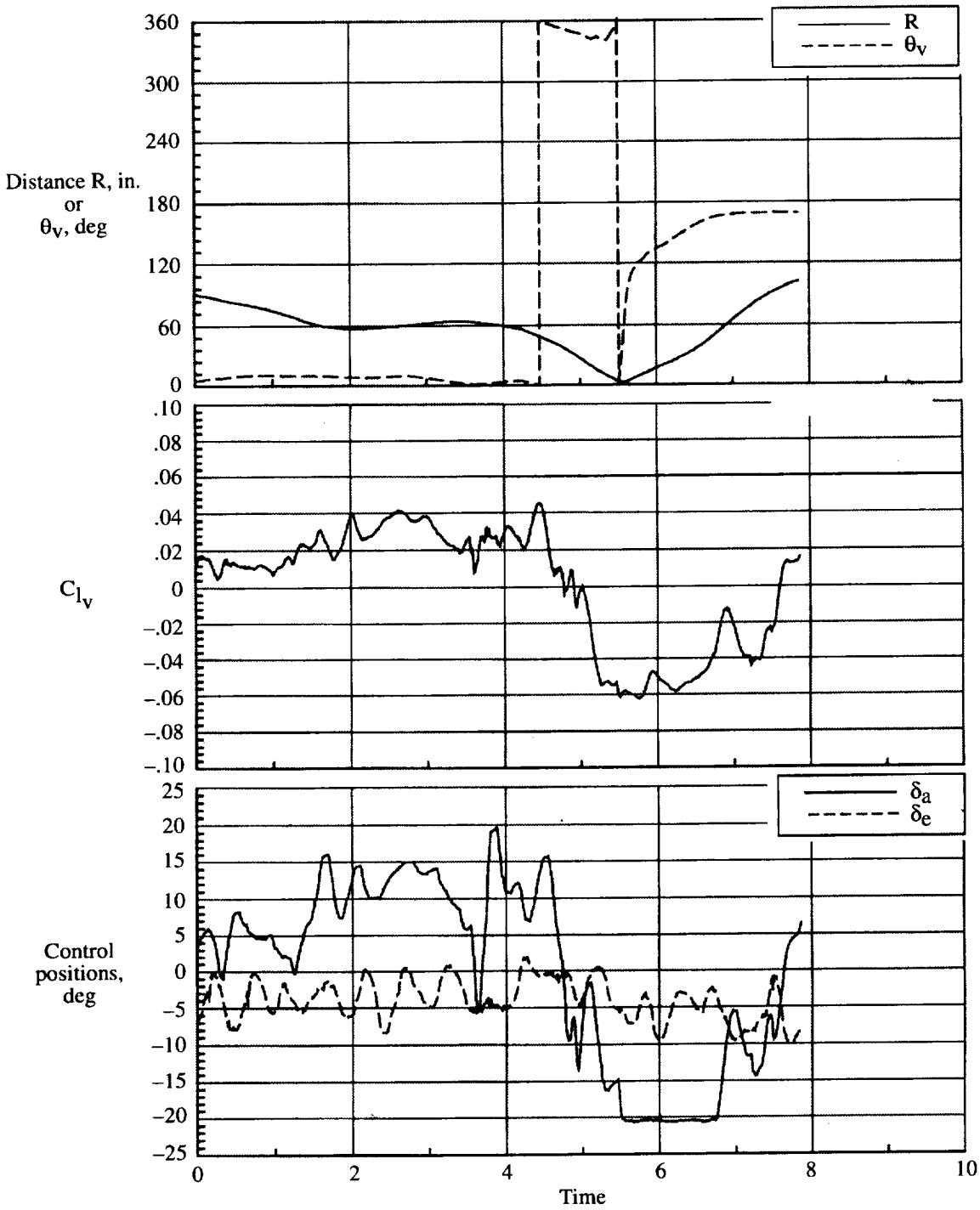

Figure 17. Continued.

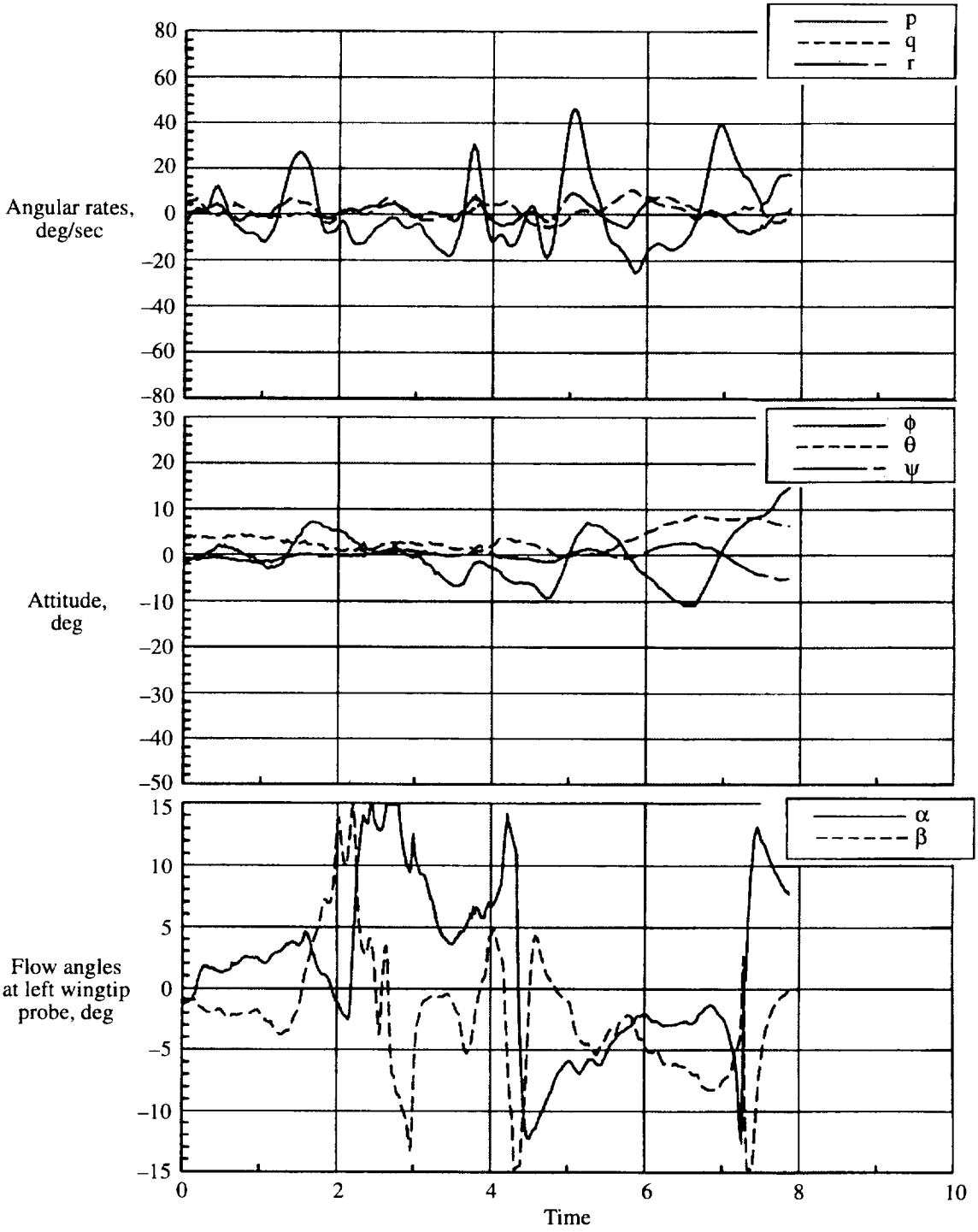

Figure 17. Concluded.

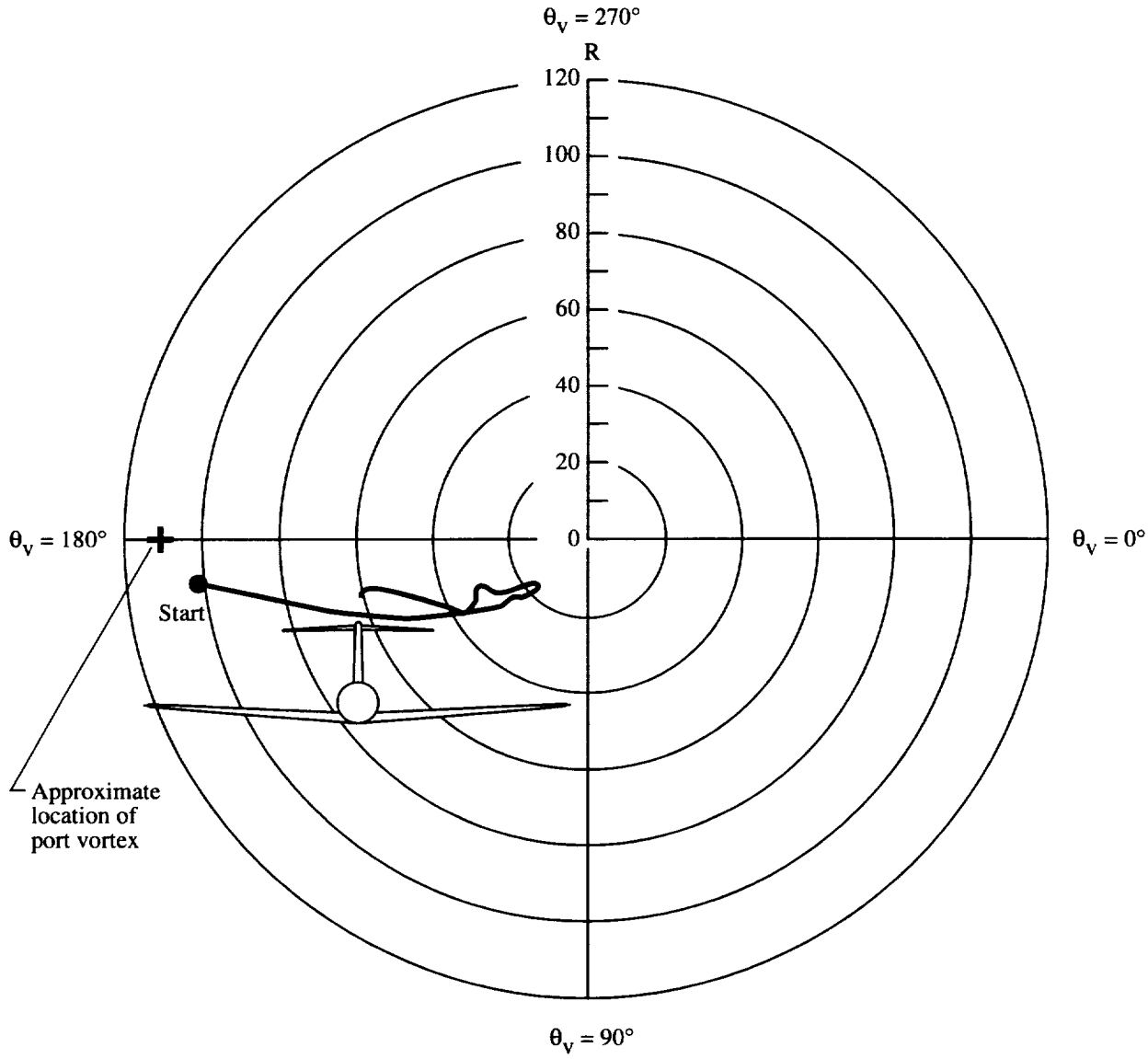

Figure 18. Left-to-right horizontal encounter. $C_{L_g} = 0.95$.

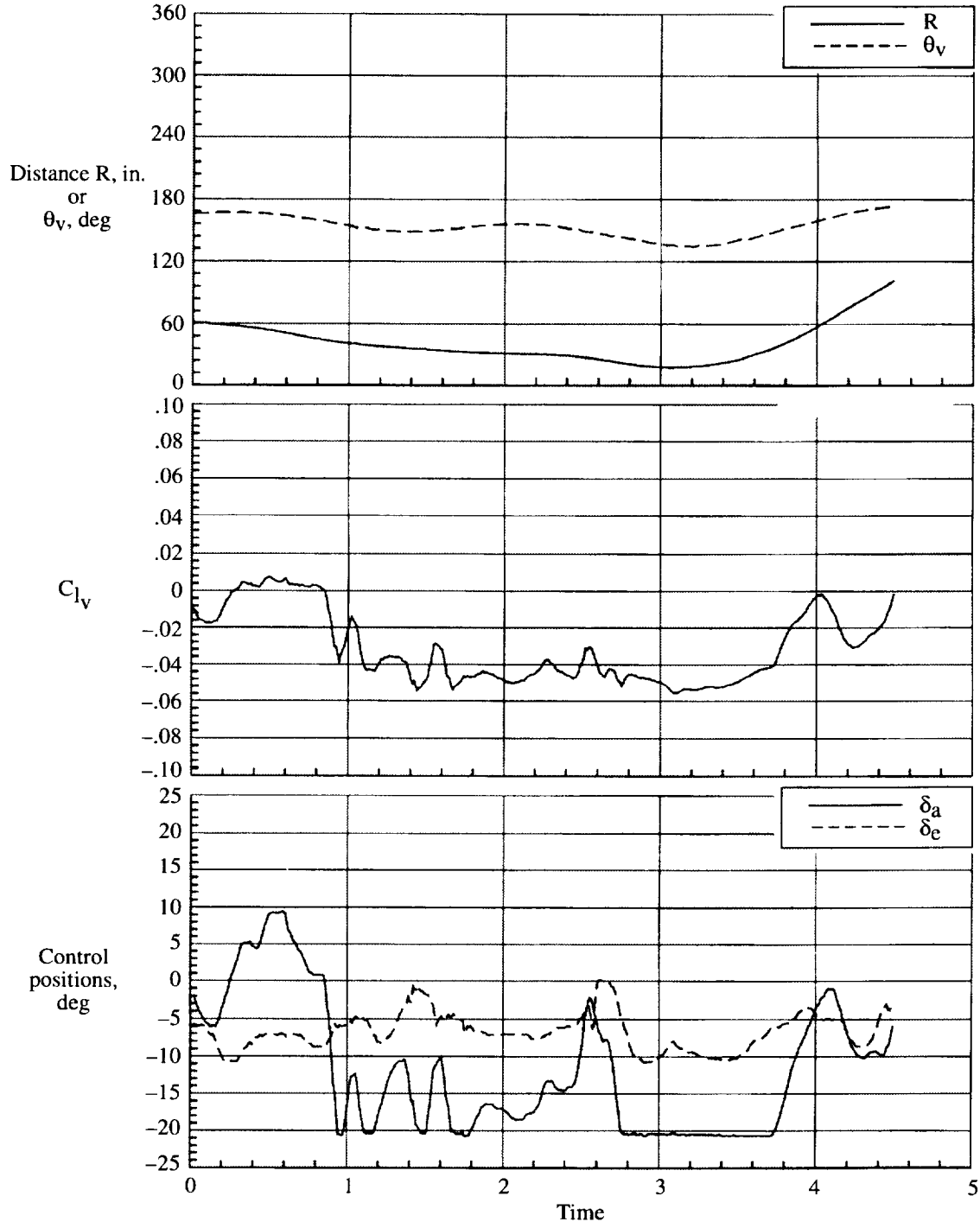

Figure 18. Continued.

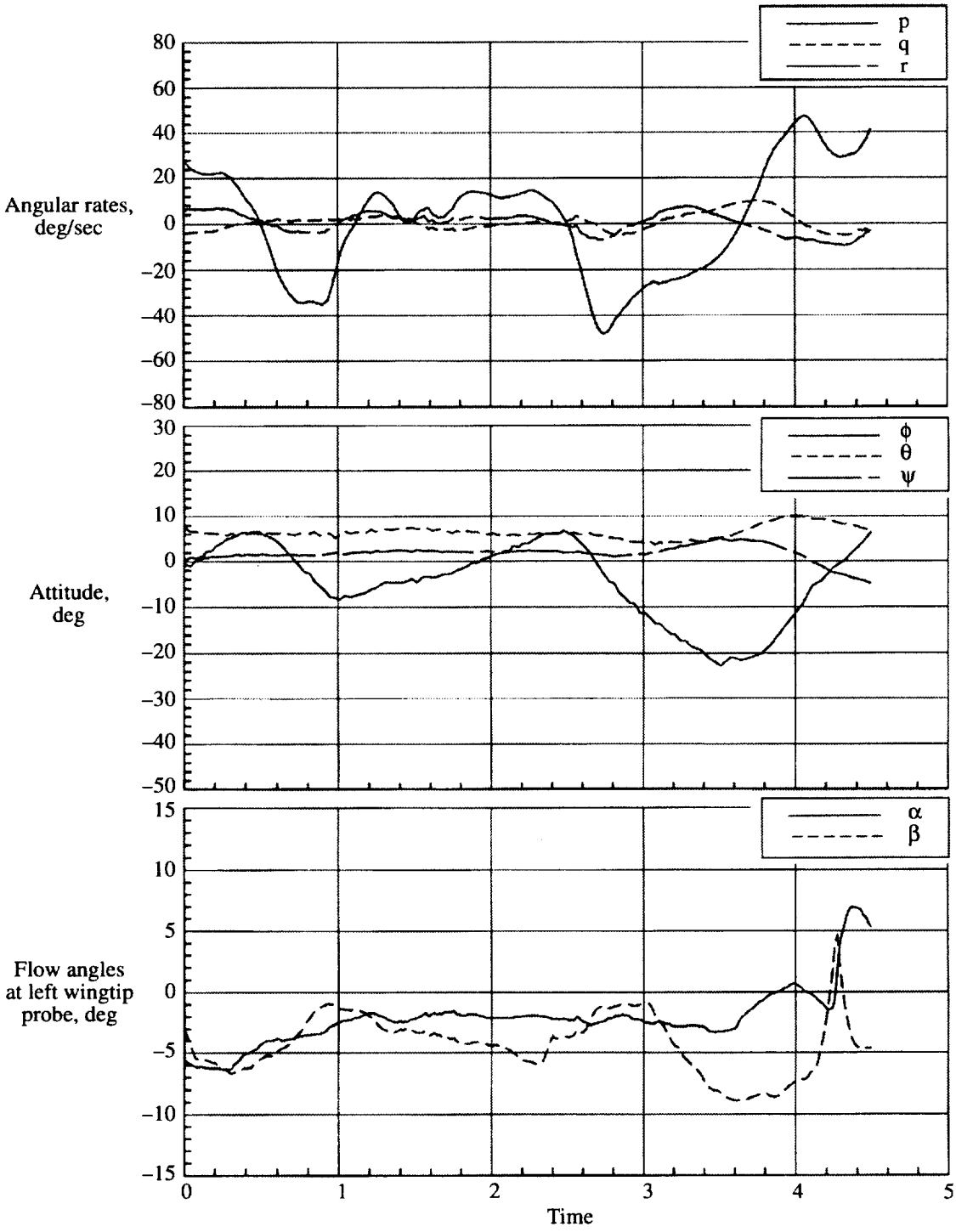

Figure 18. Concluded.

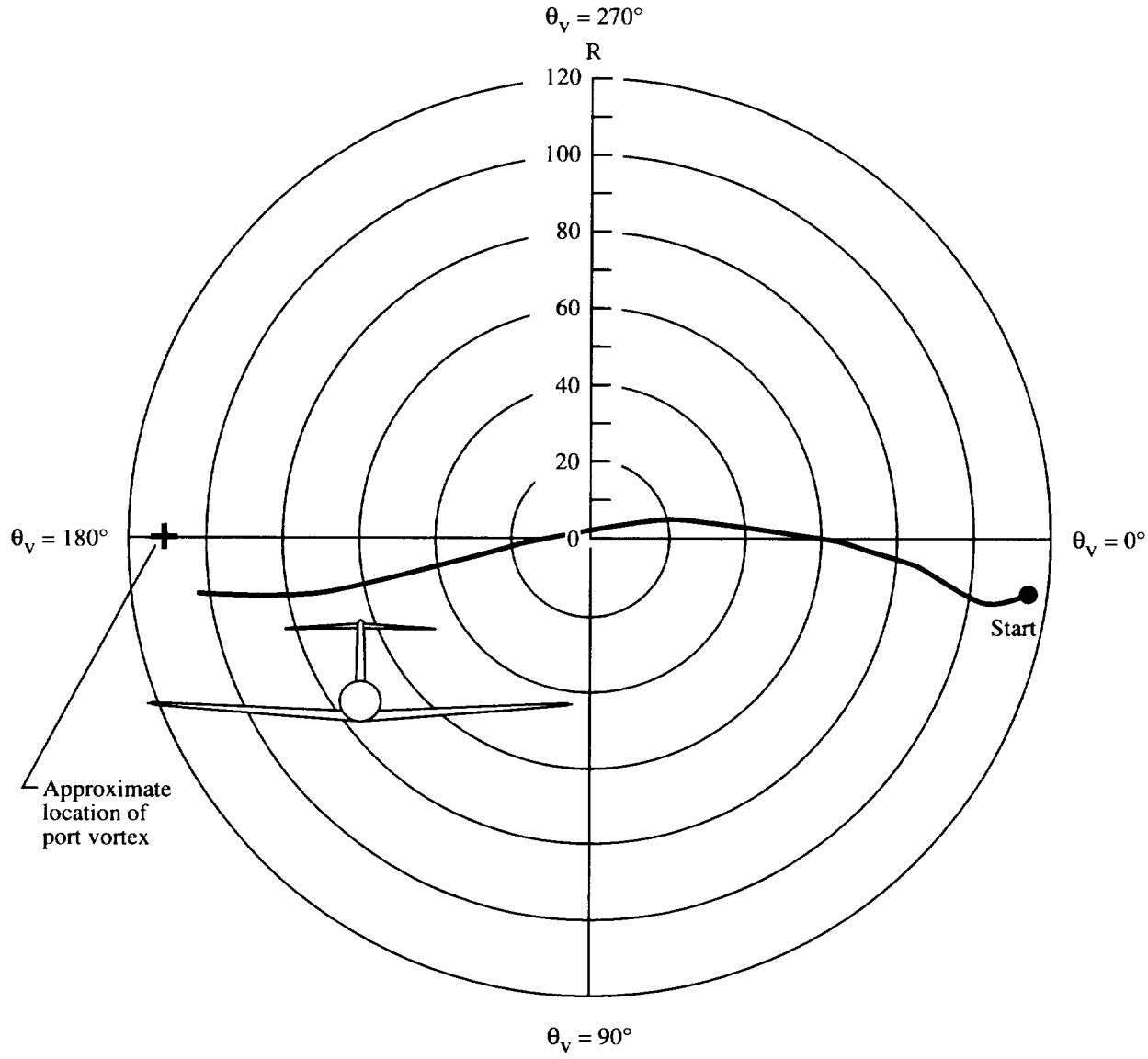

Figure 19. Right-to-left horizontal encounter. C_{L_g} = 1.07.

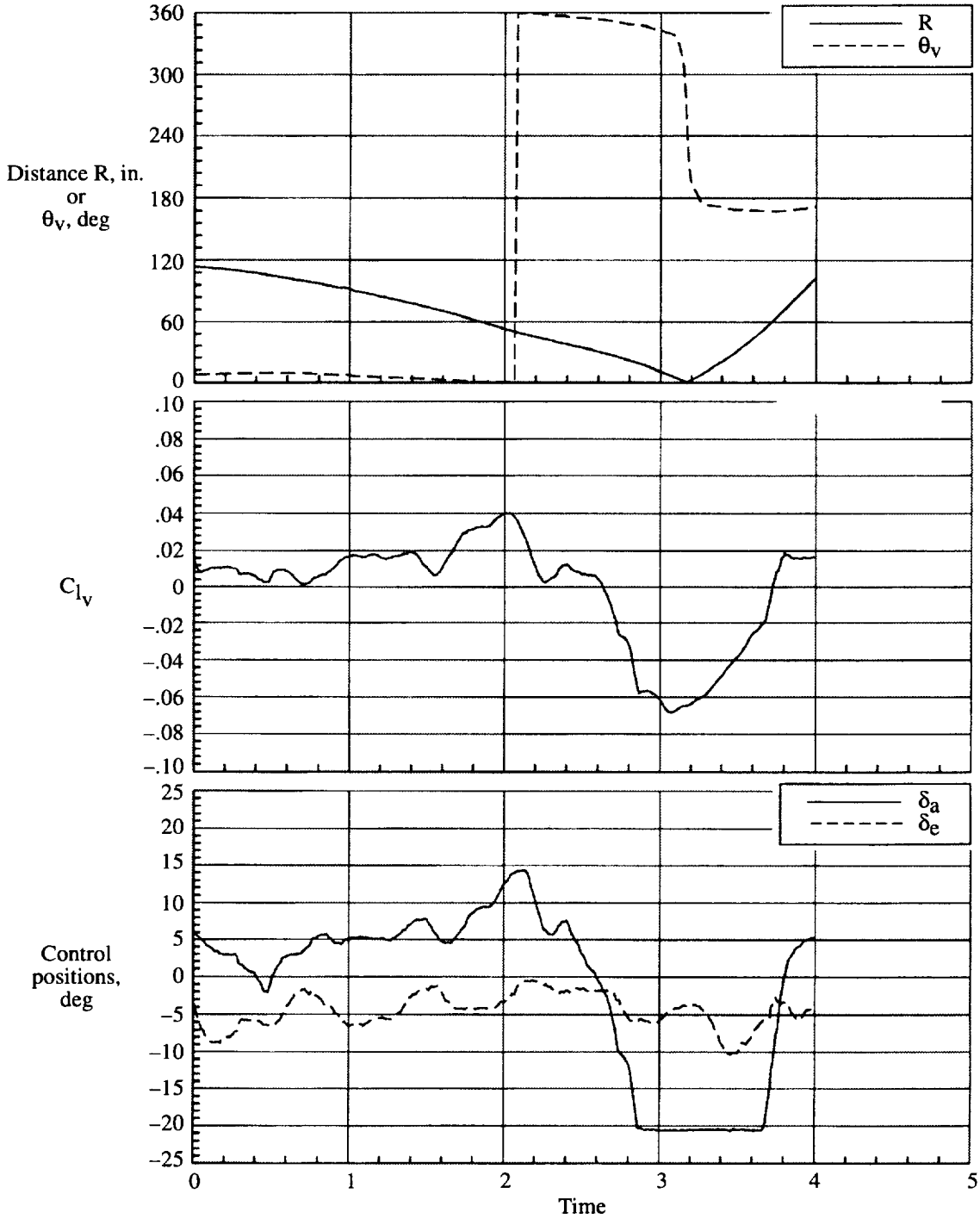

Figure 19. Continued.

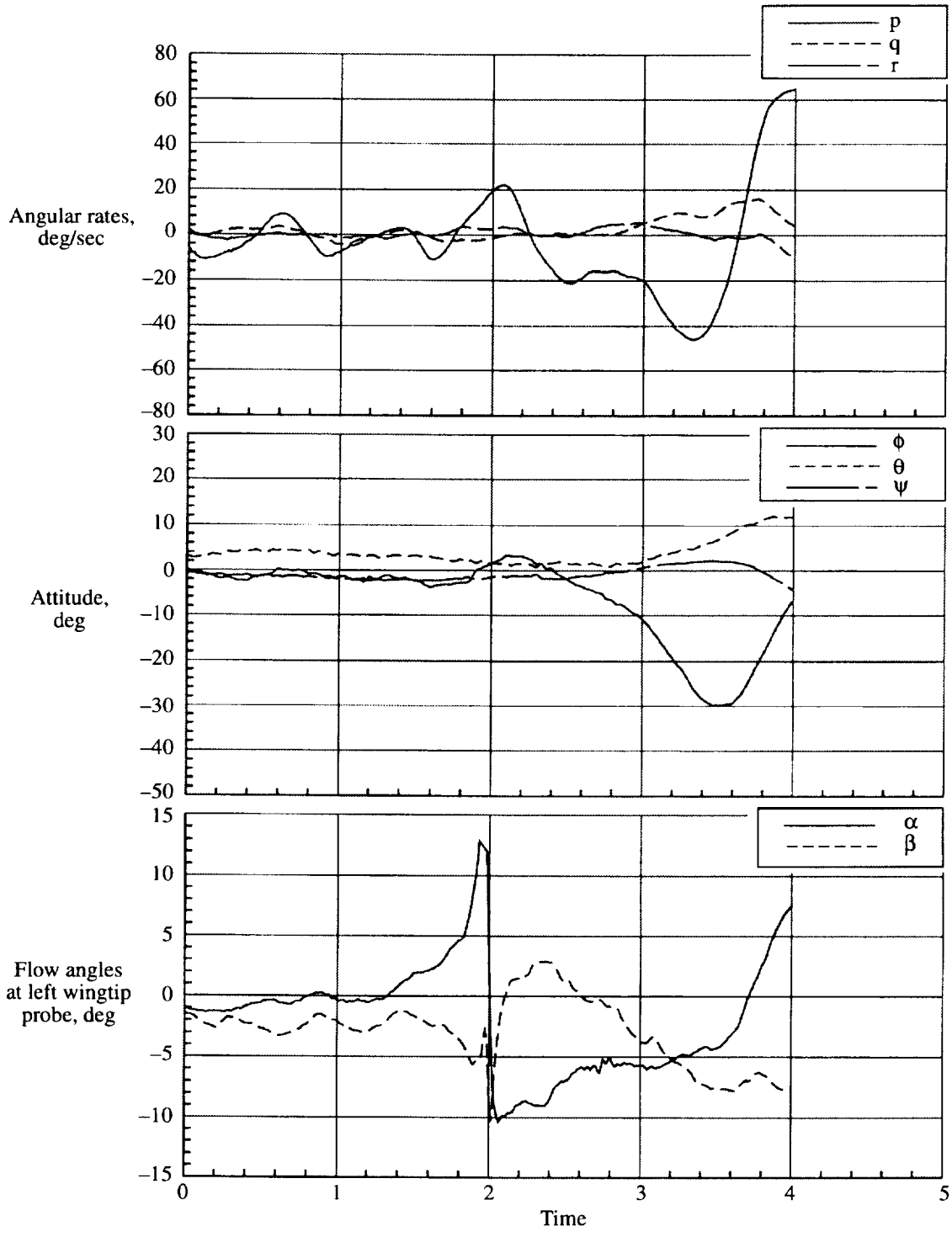

Figure 19. Concluded.

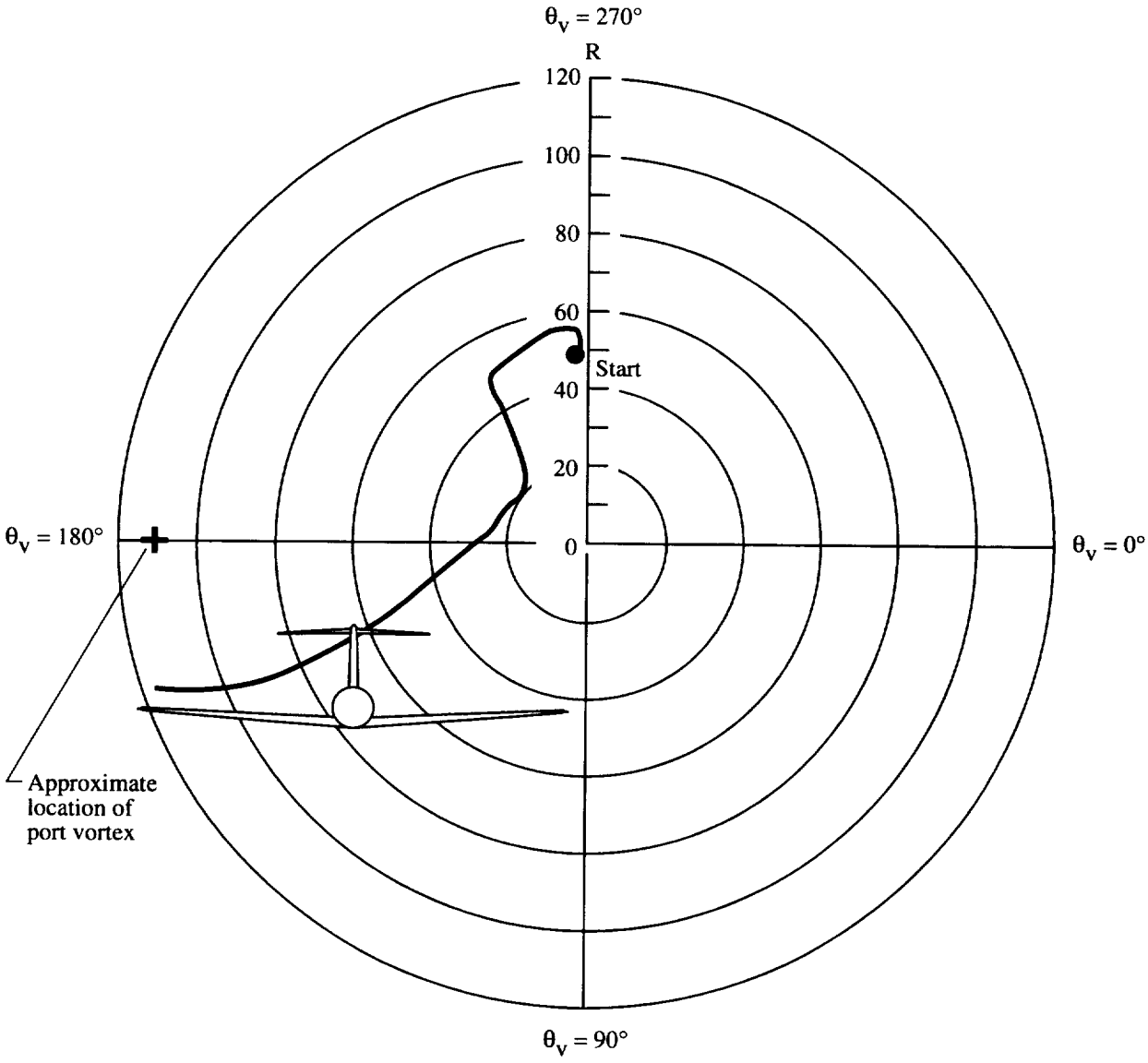

Figure 20. Descending vertical encounter. C_{L_g} = 1.07.

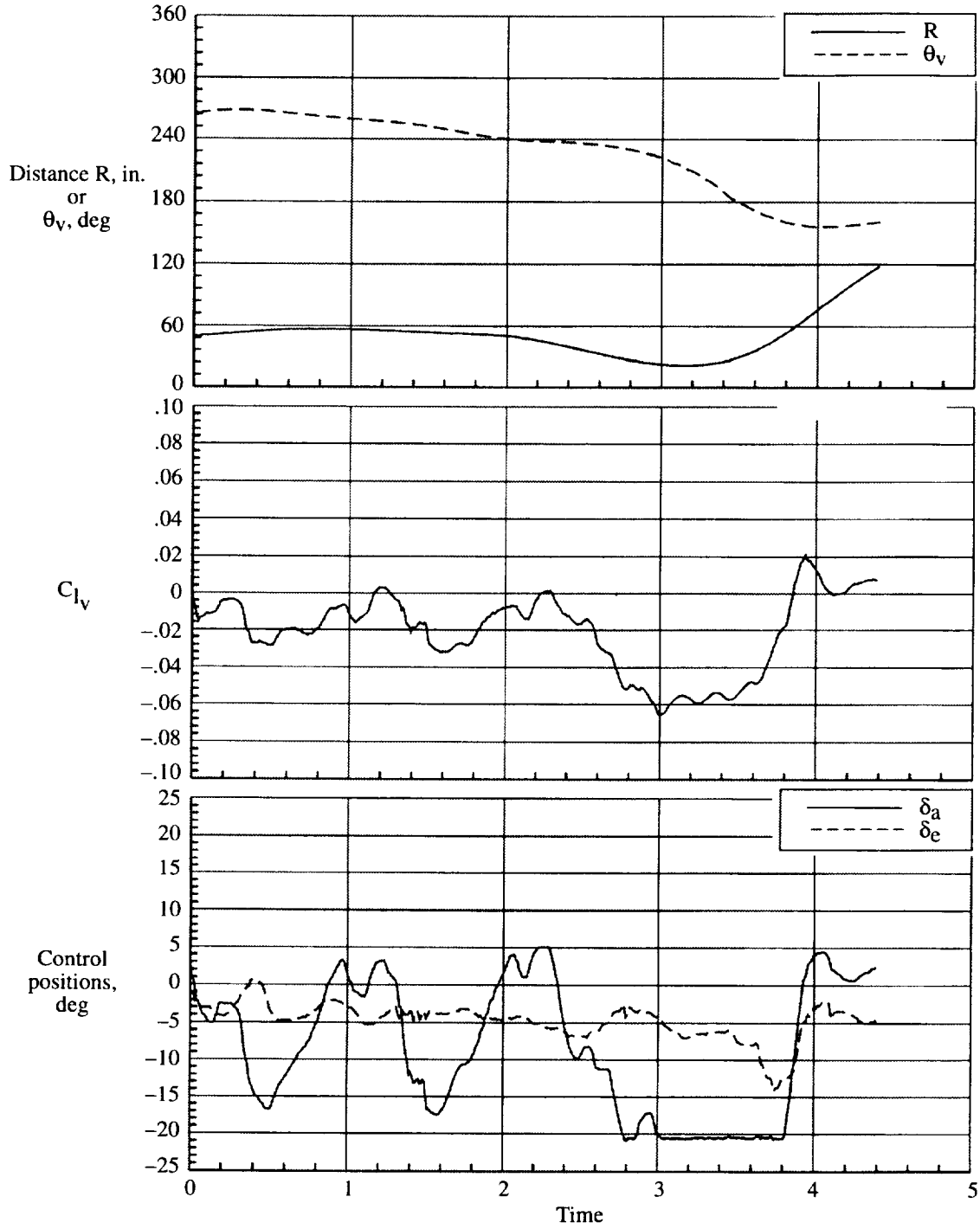

Figure 20. Continued.

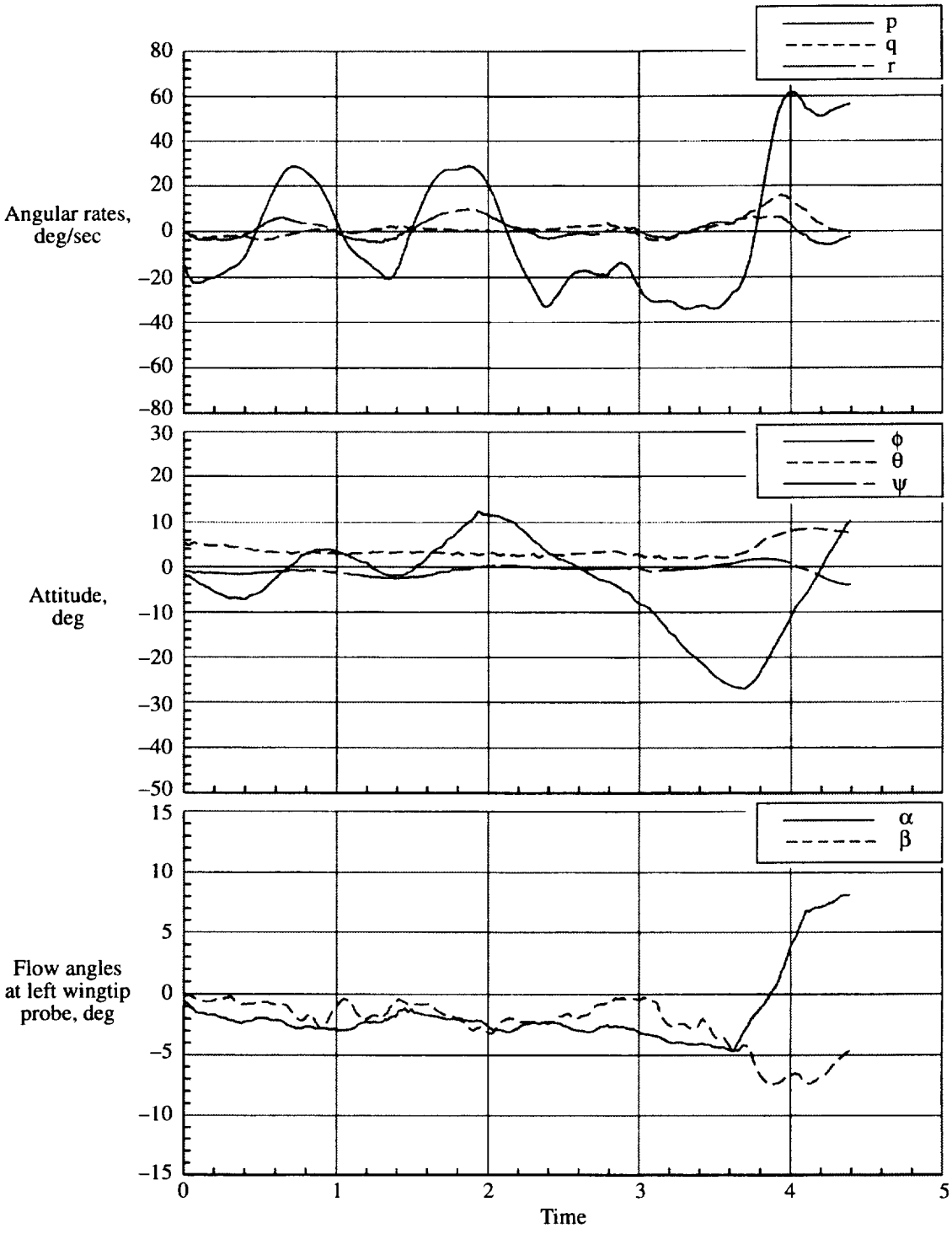

Figure 20. Concluded.

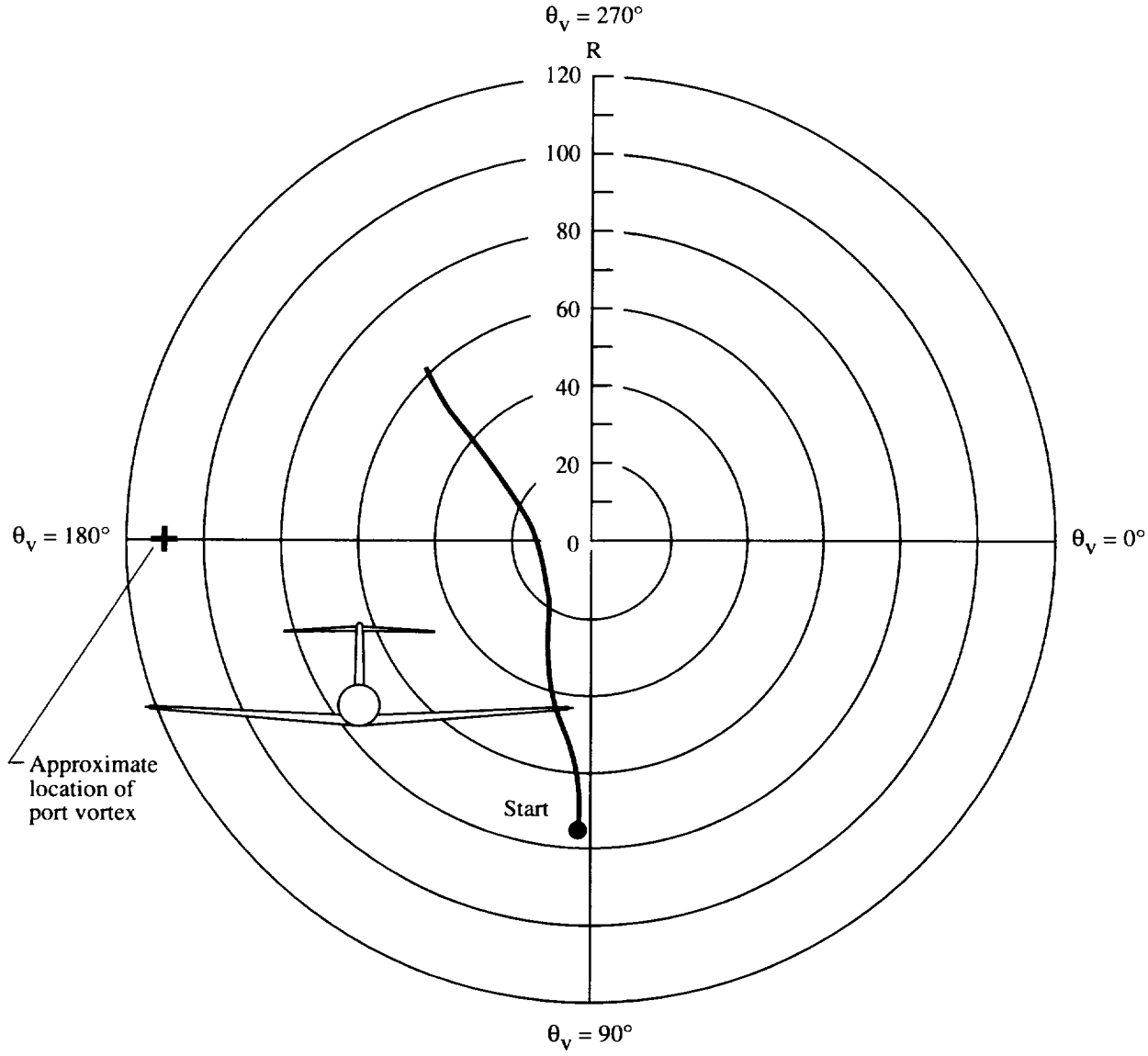

Figure 21. Ascending vertical encounter. C_{L_g} = 1.07.

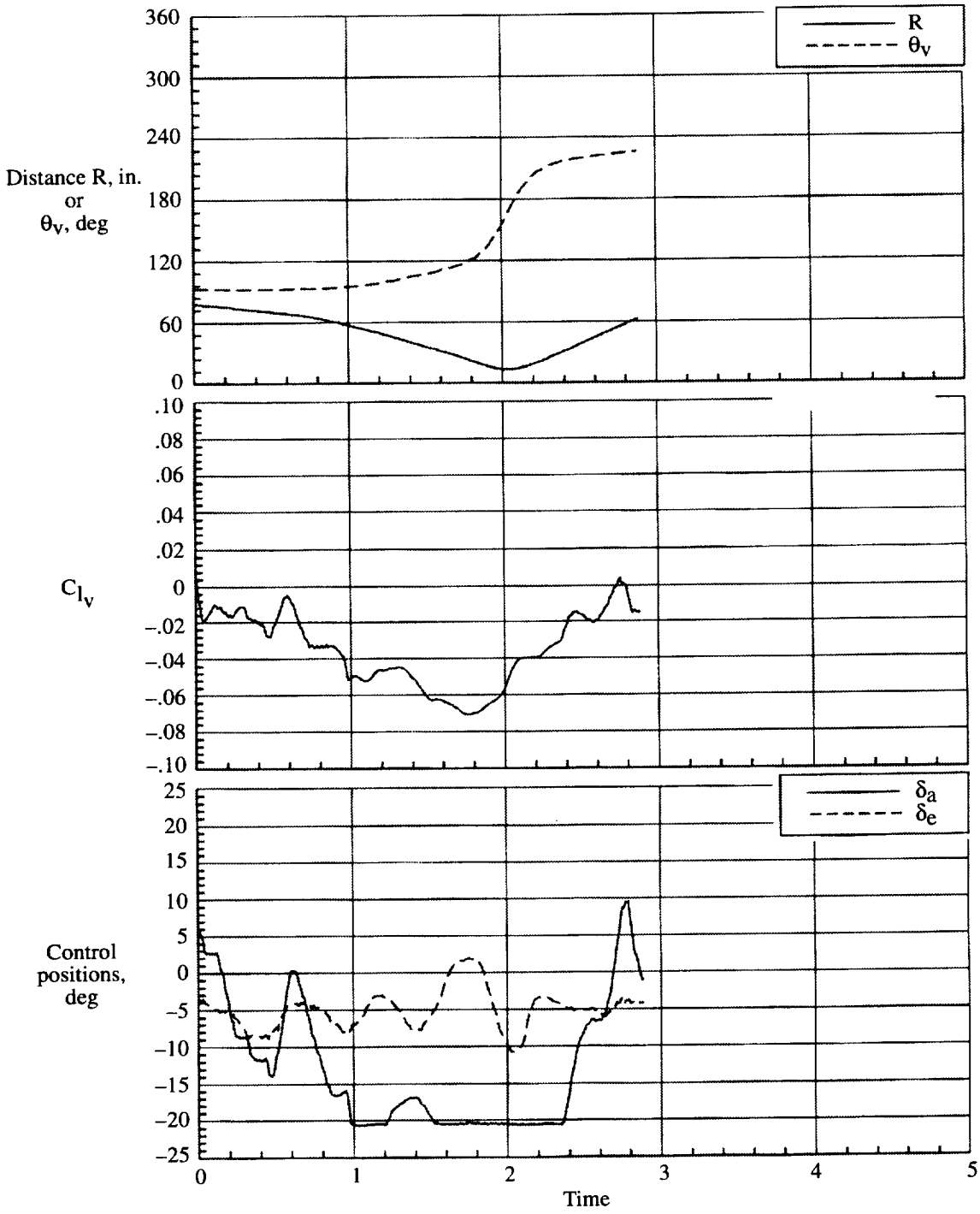

Figure 21. Continued.

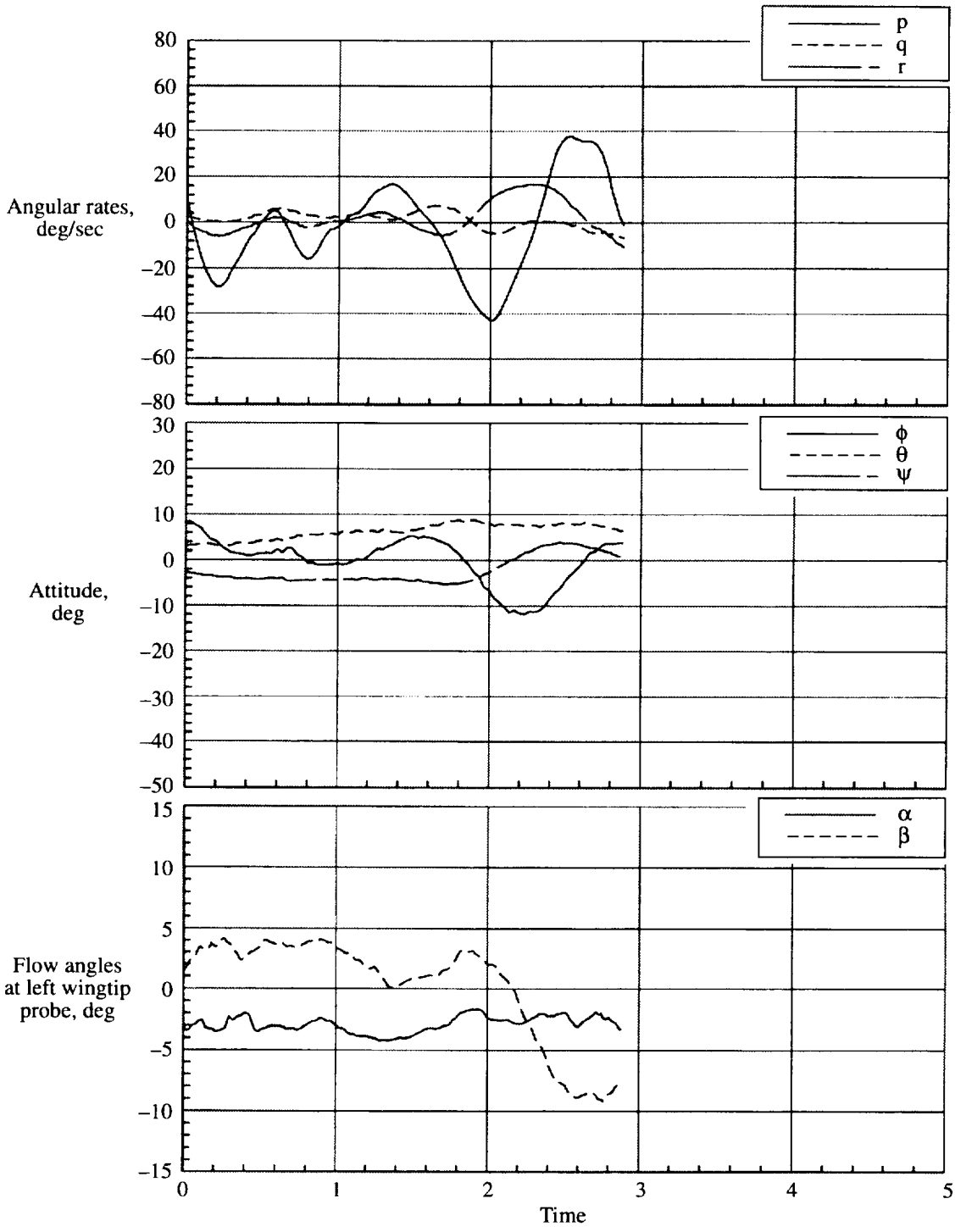

Figure 21. Concluded.

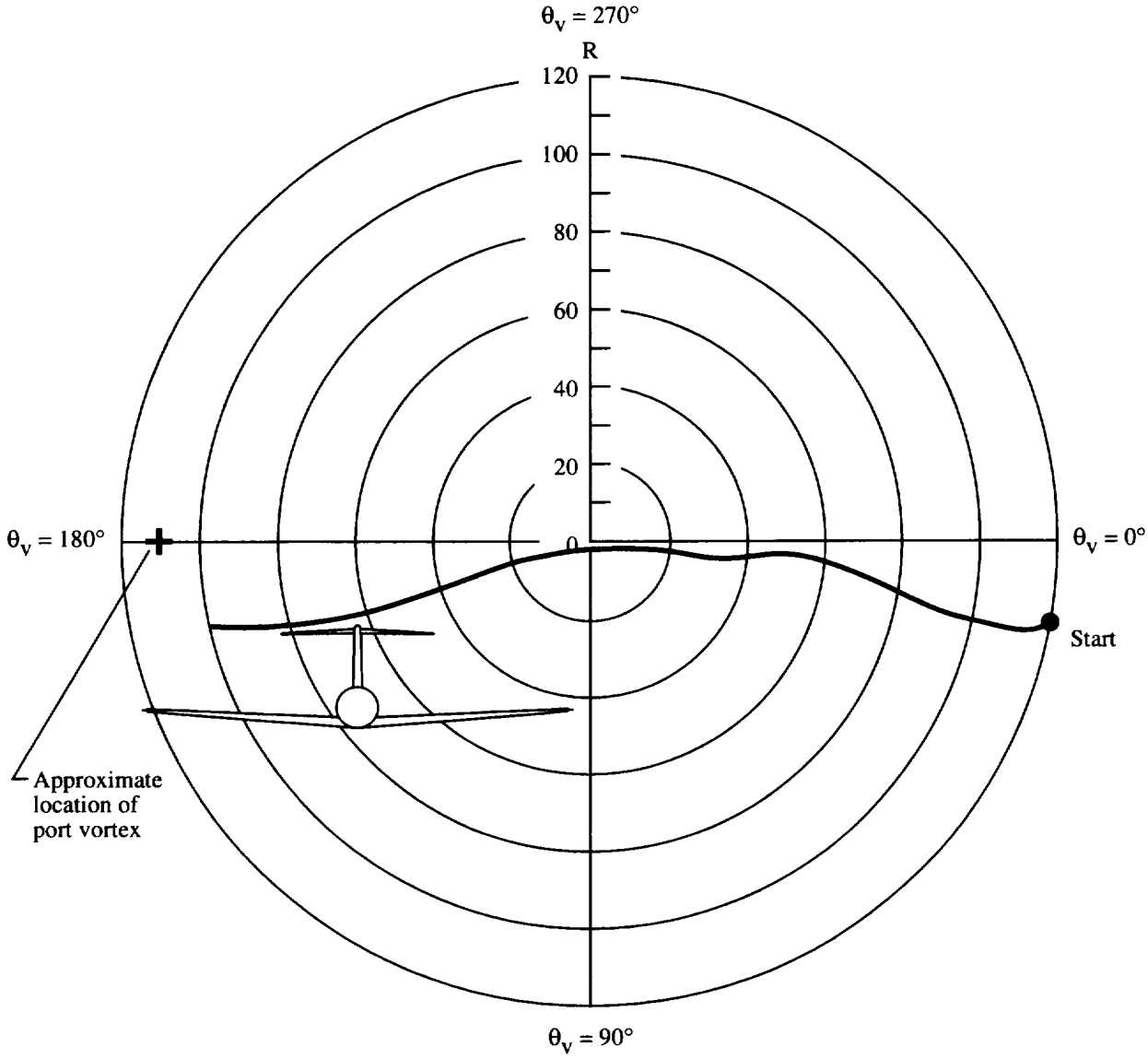

Figure 22. Right-to-left horizontal encounter. $C_{L_g} = 1.18$.

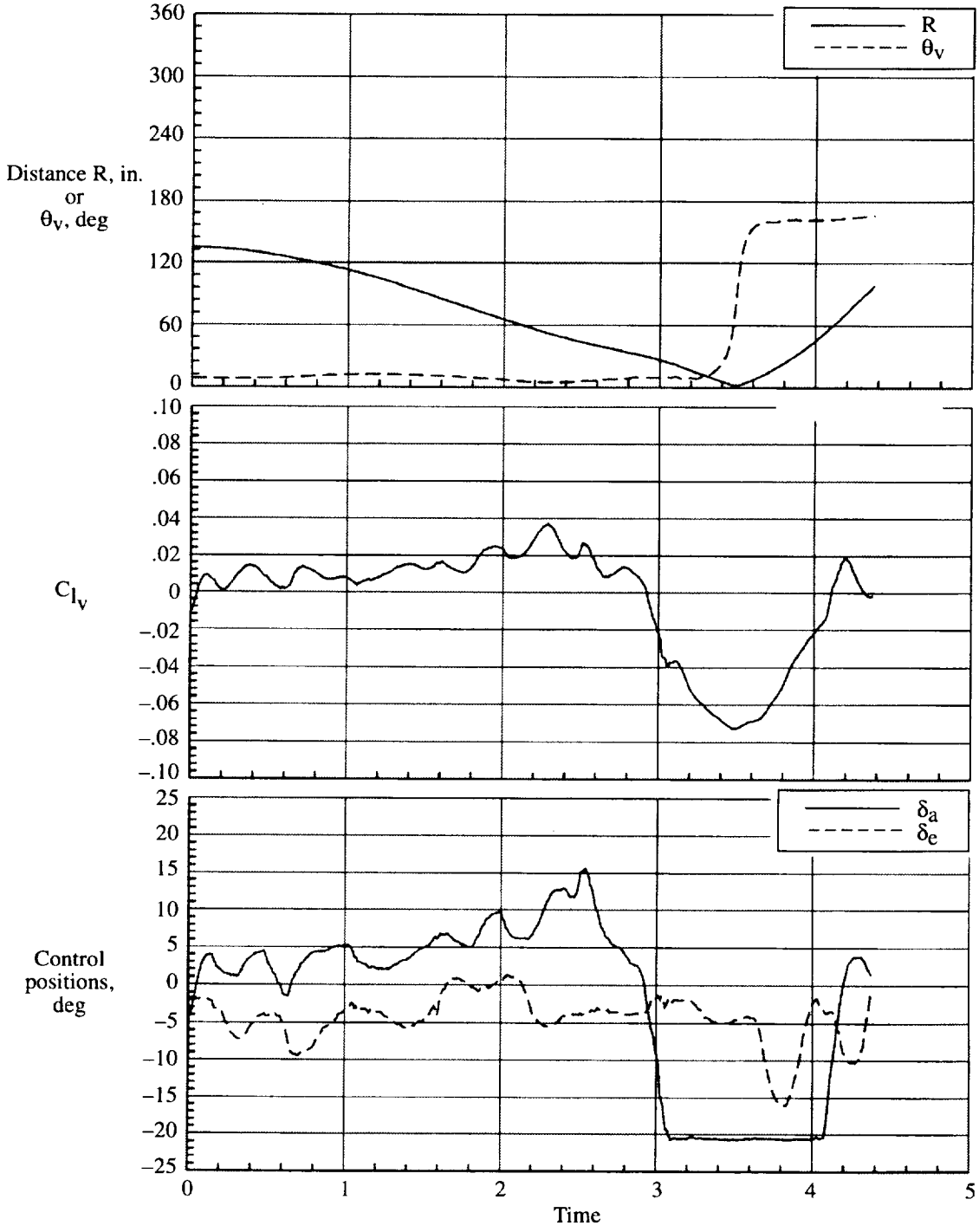

Figure 22. Continued.

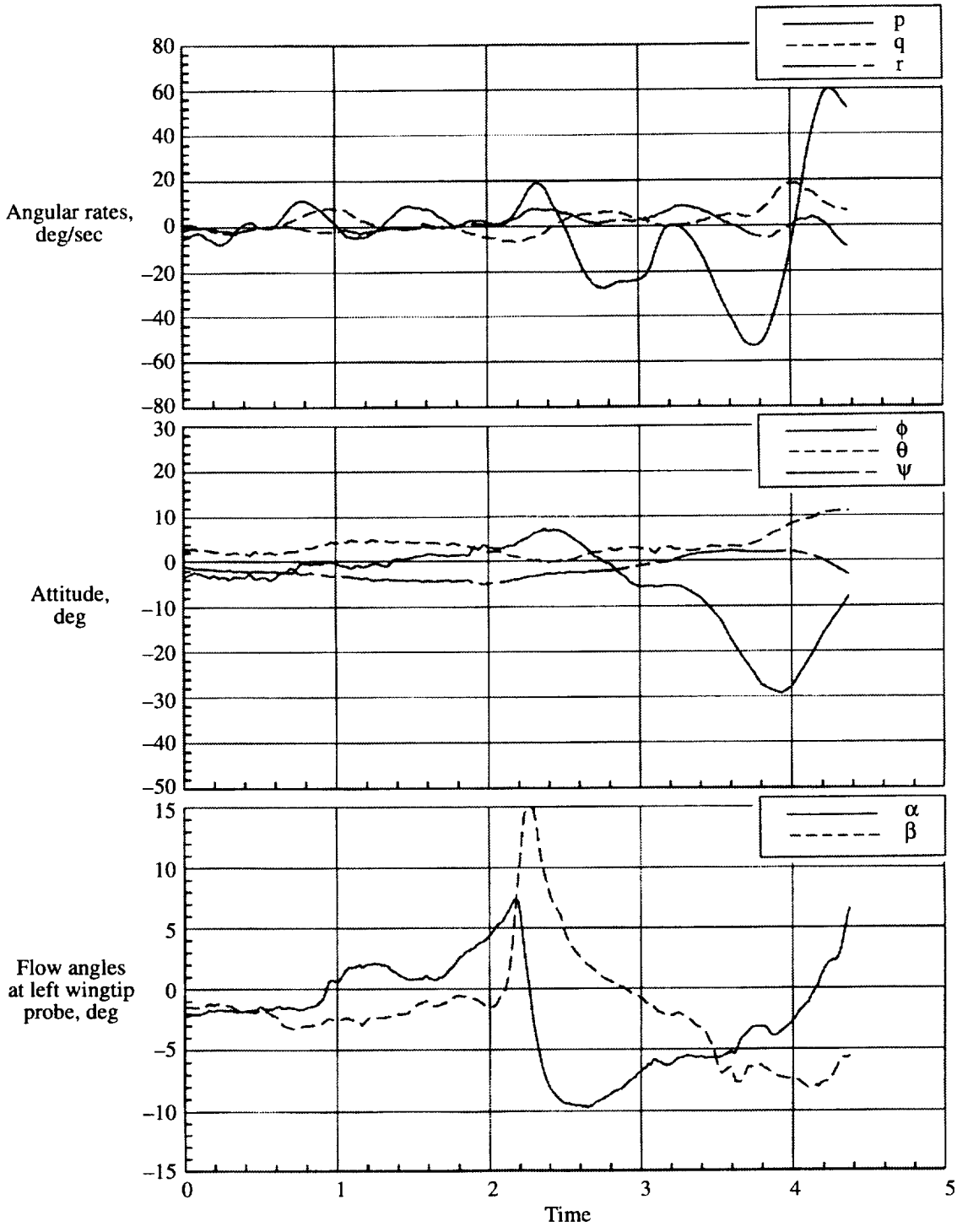

Figure 22. Concluded.

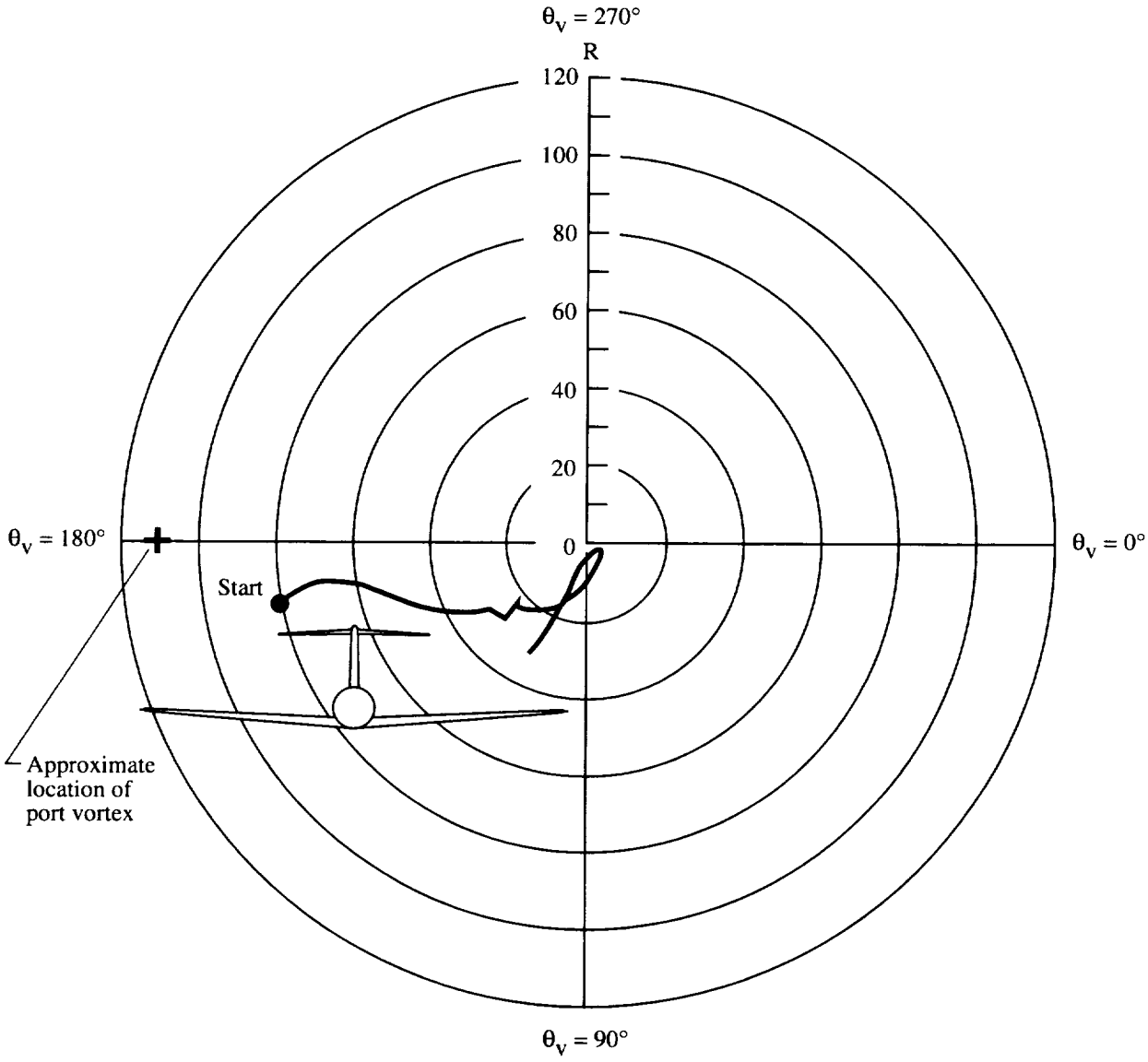

Figure 23. Left-to-right horizontal encounter. $C_{L_g} = 1.18$.

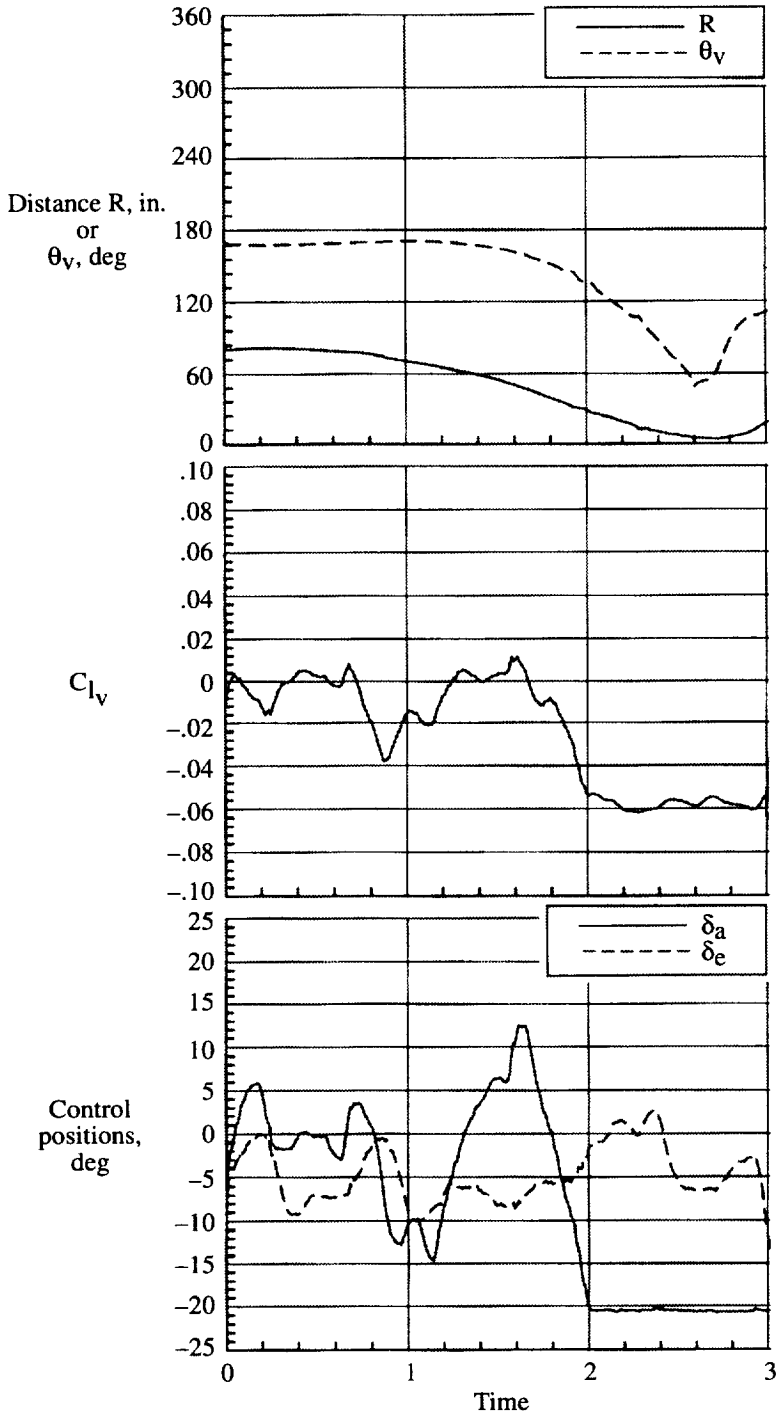

Figure 23. Continued.

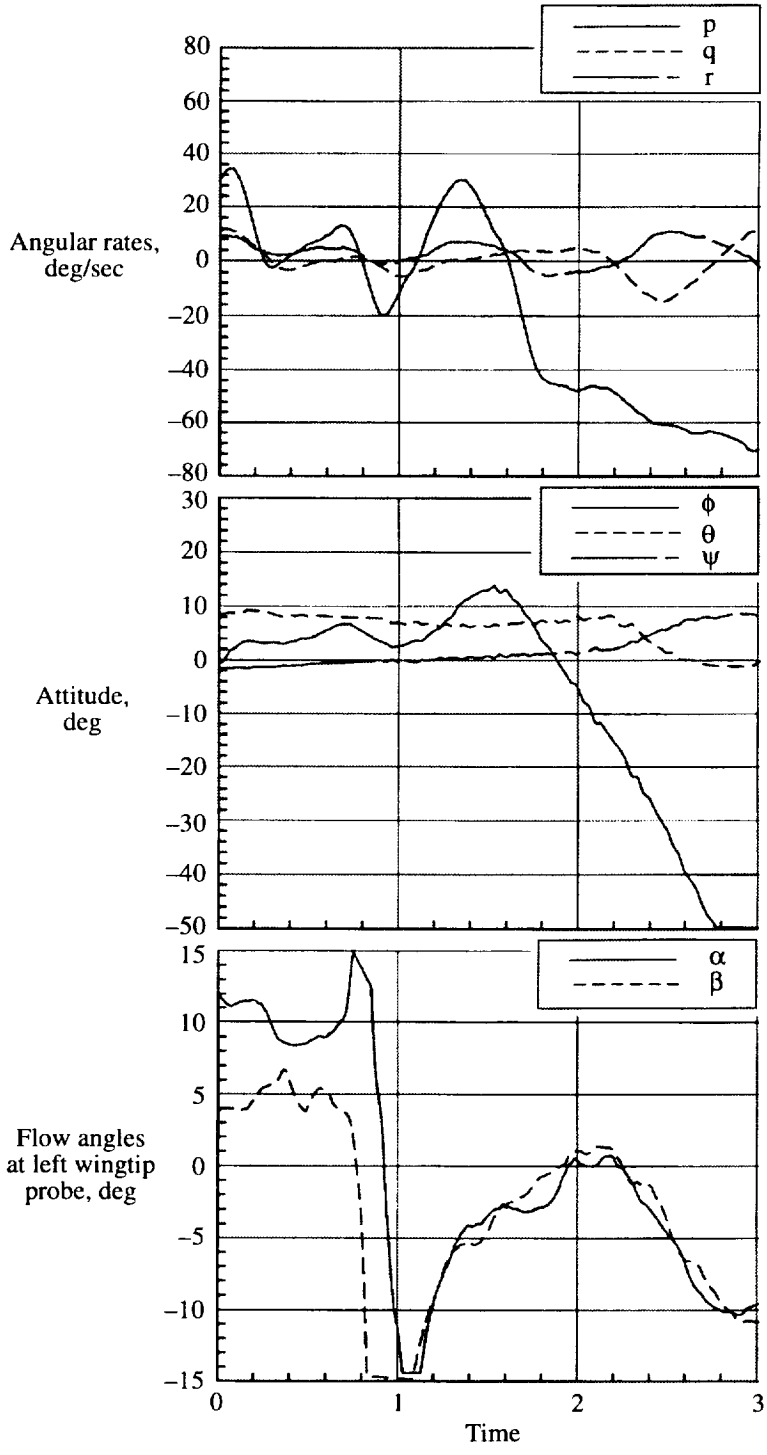

Figure 23. Concluded.

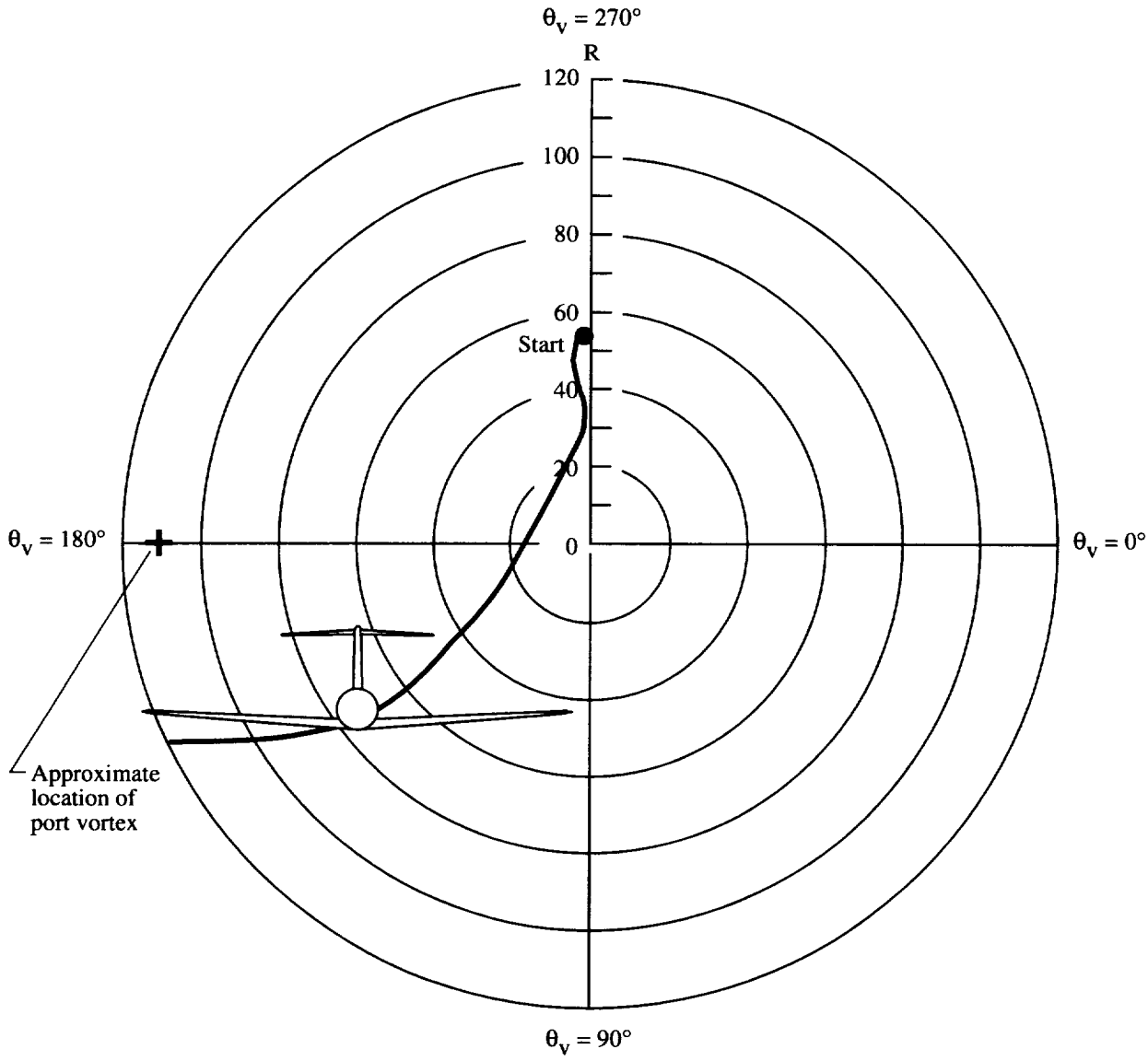

Figure 24. Descending vertical encounter. C_{L_g} = 1.18.

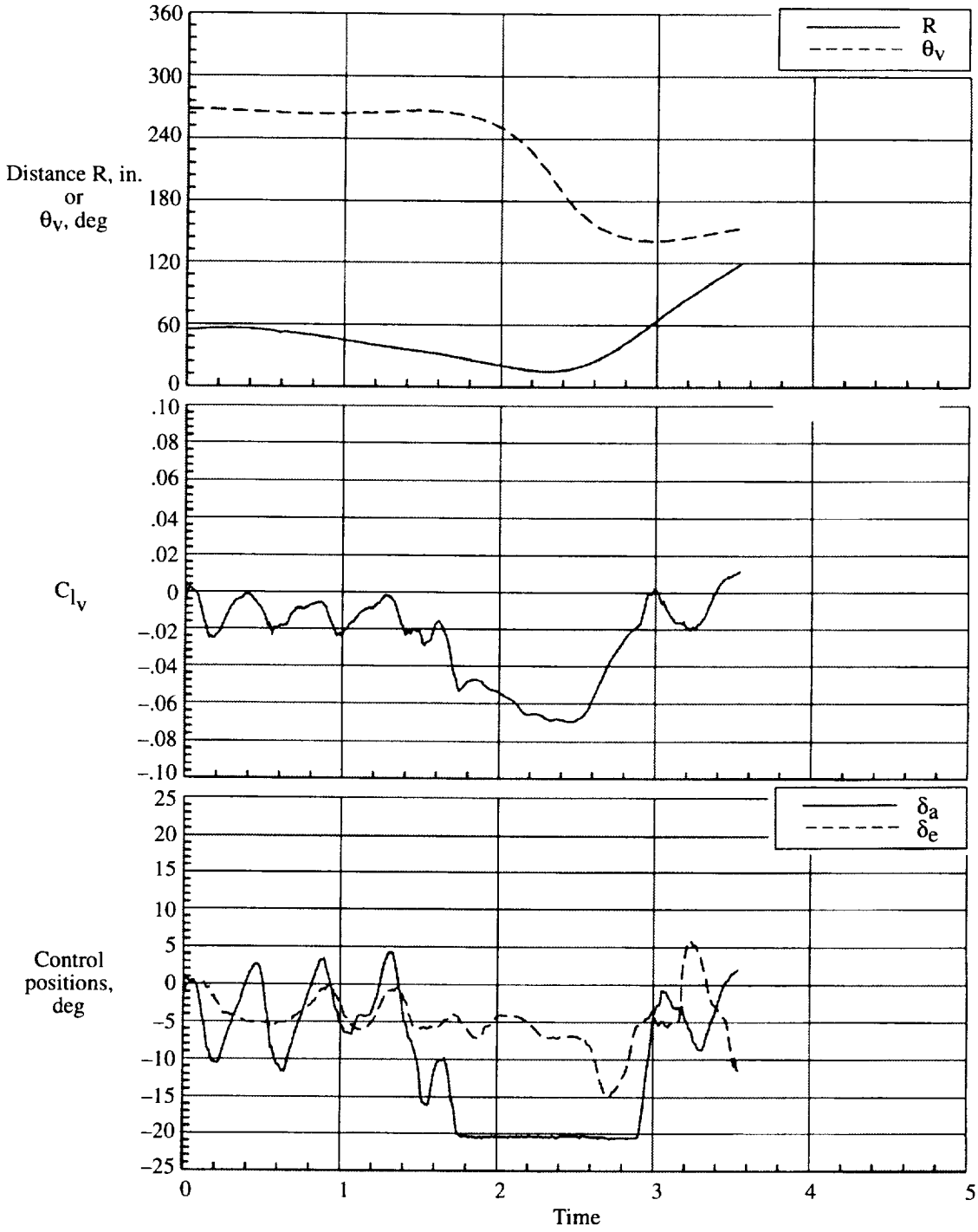

Figure 24. Continued.

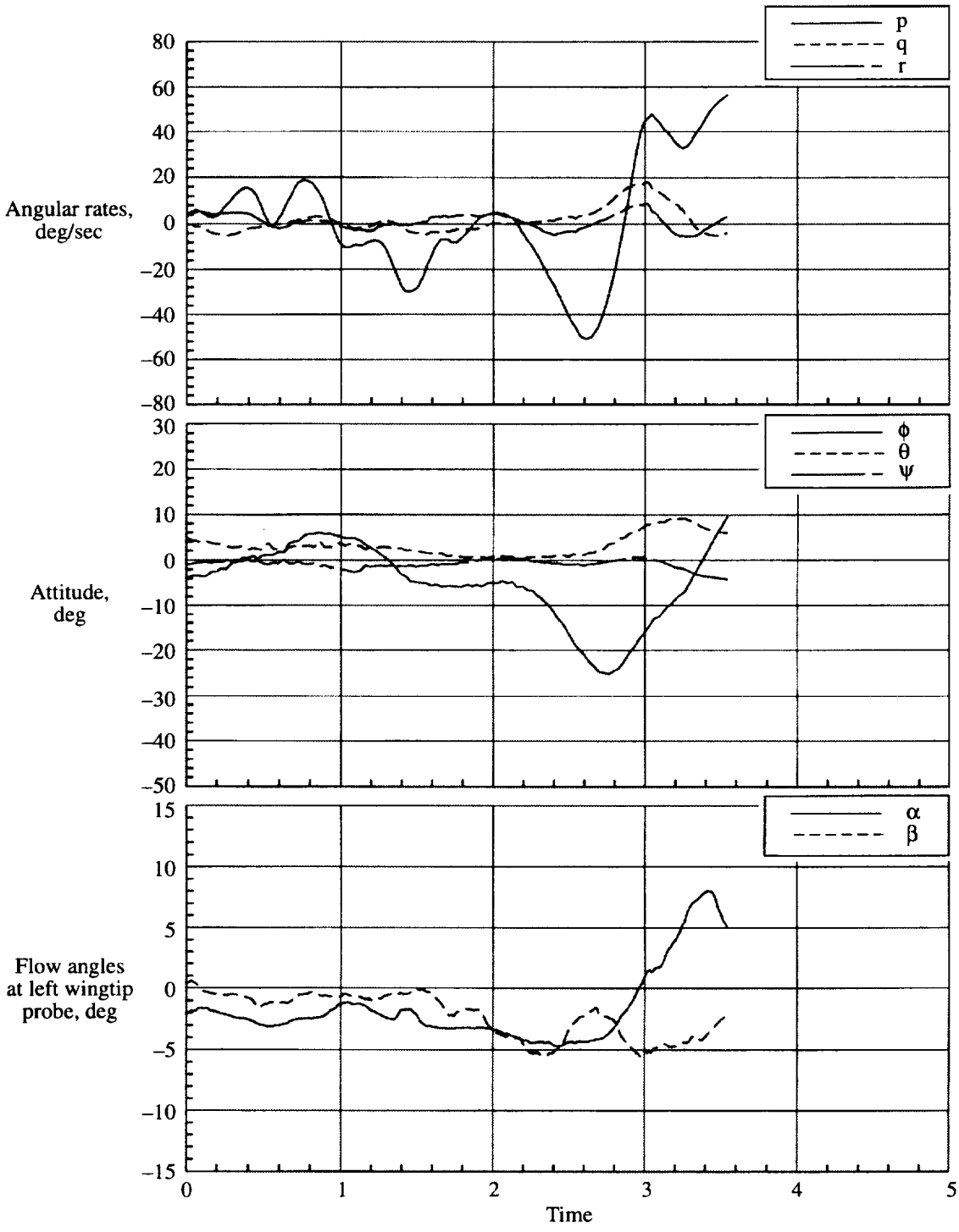

Figure 24. Concluded.

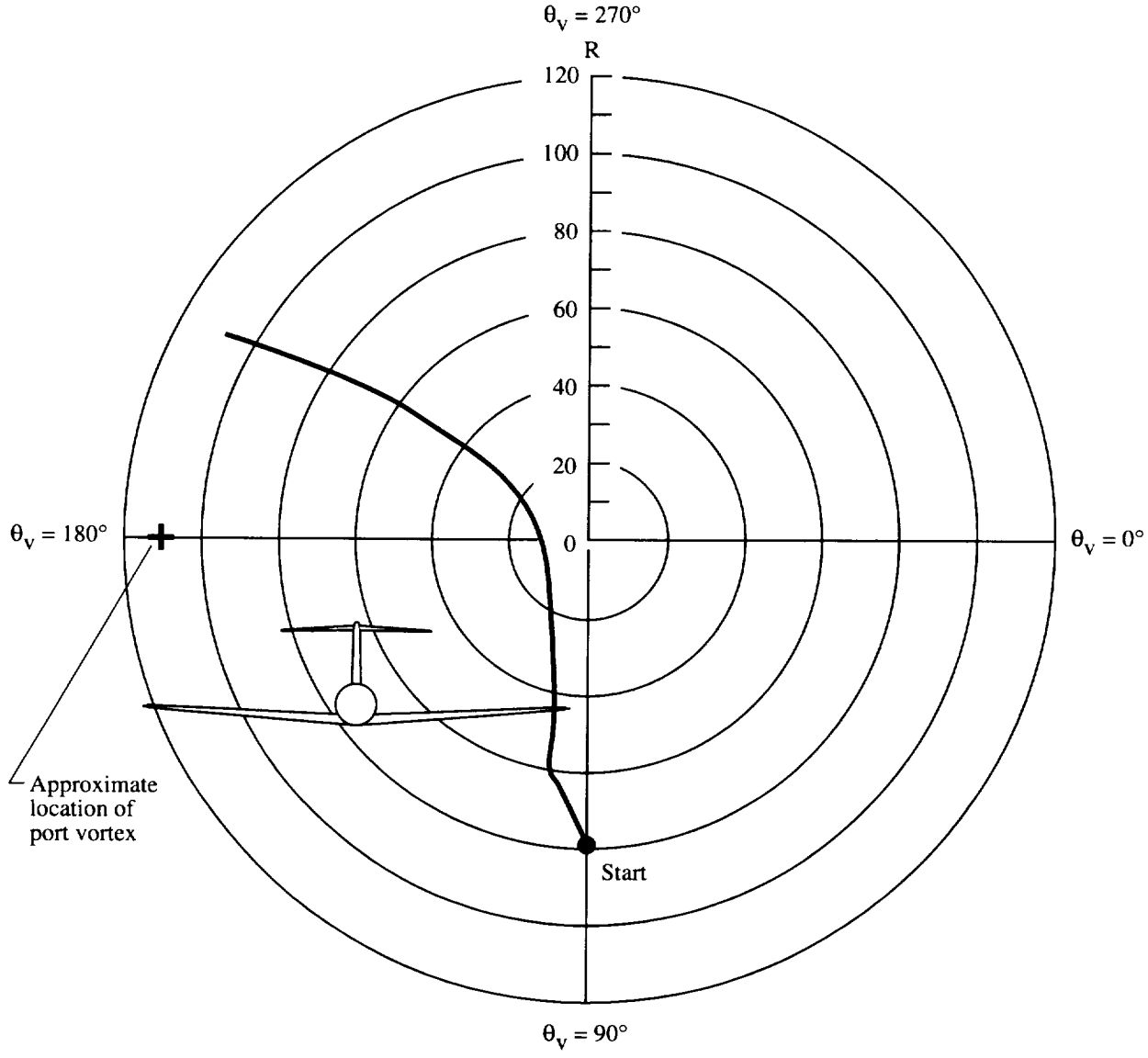

Figure 25. Ascending vertical encounter. $C_{L_g} = 1.18$.

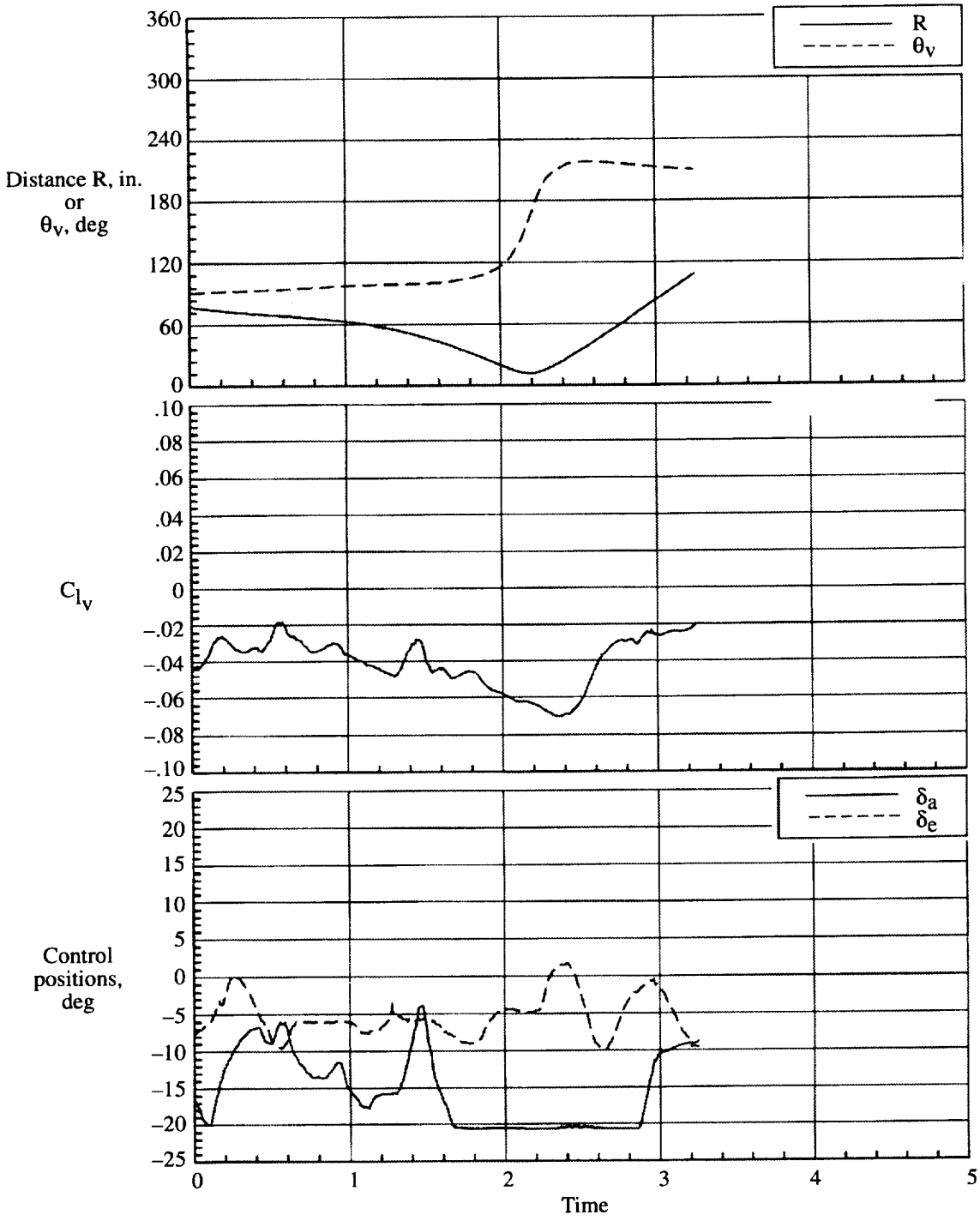

Figure 25. Continued.

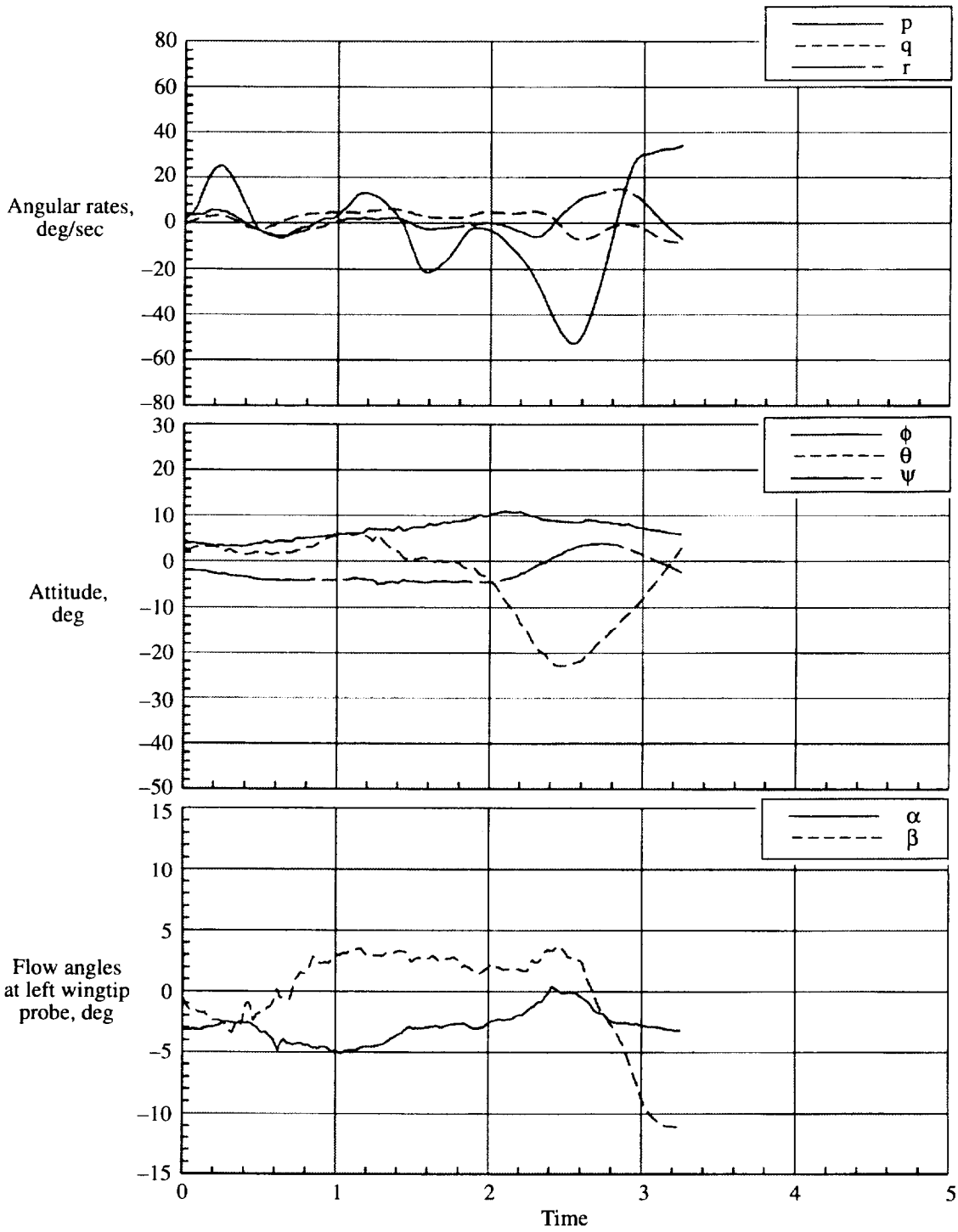

Figure 25. Concluded.

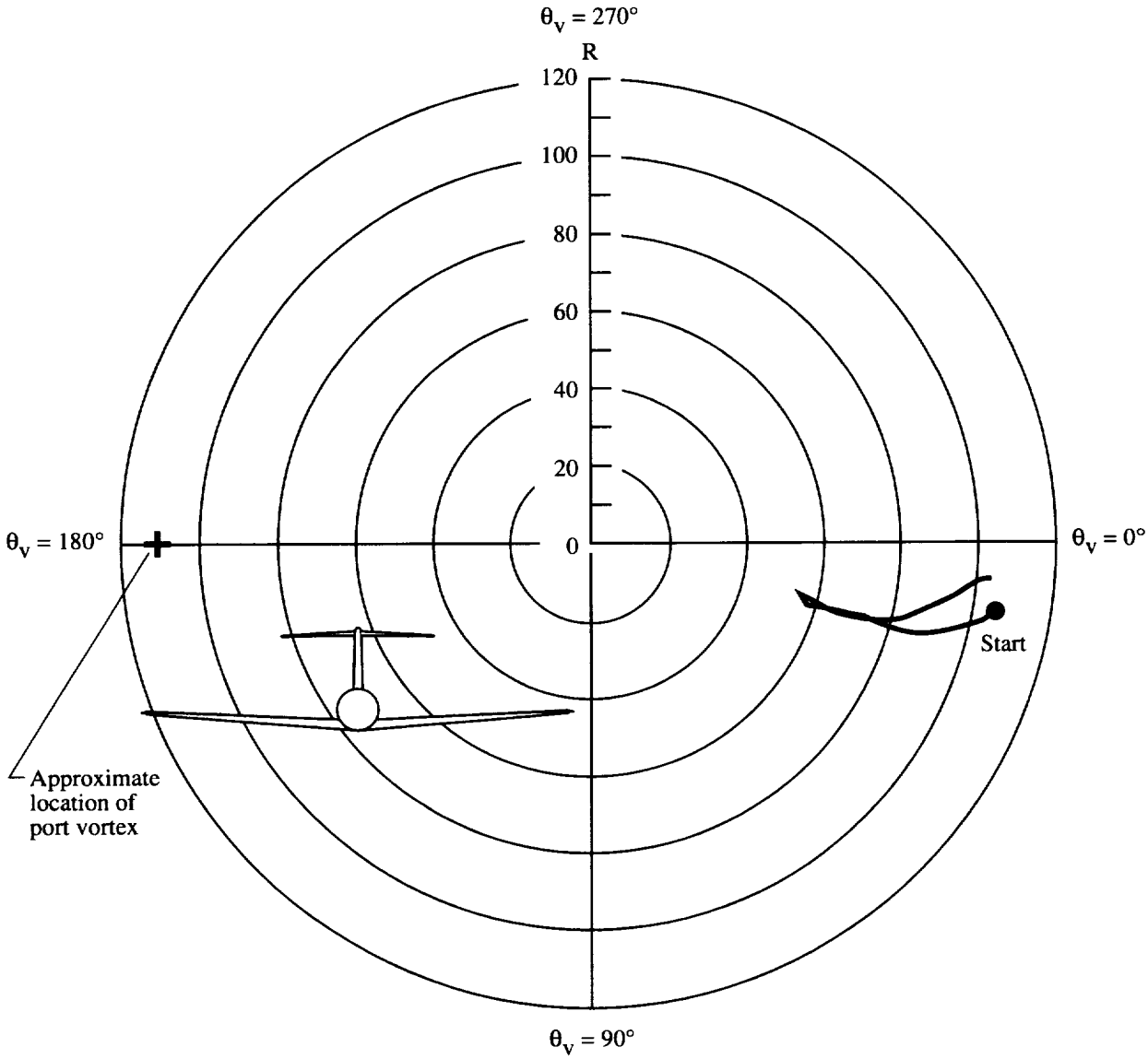

Figure 26. Right-to-left horizontal encounter. $C_{L_g} = 1.25$.

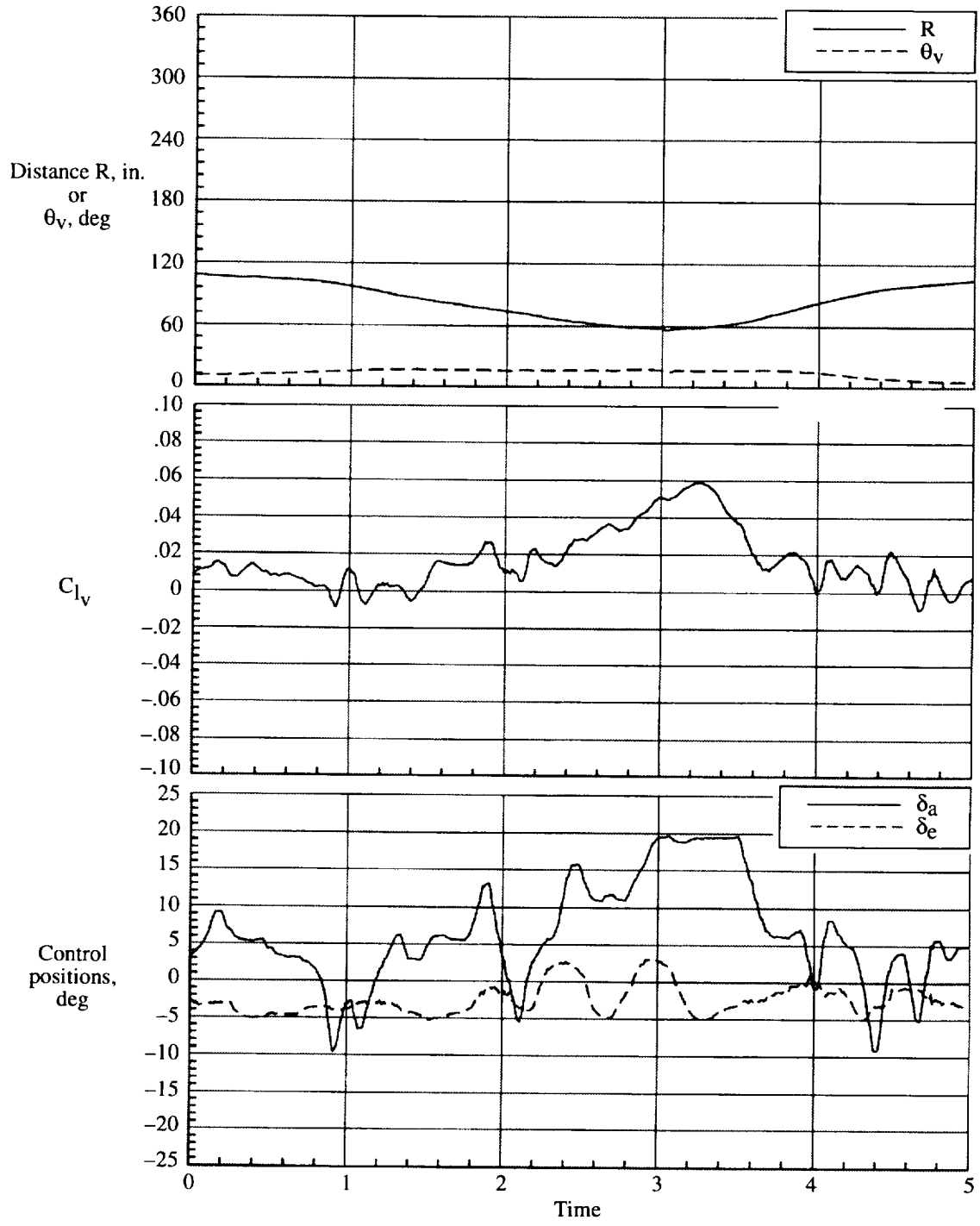

Figure 26. Continued.

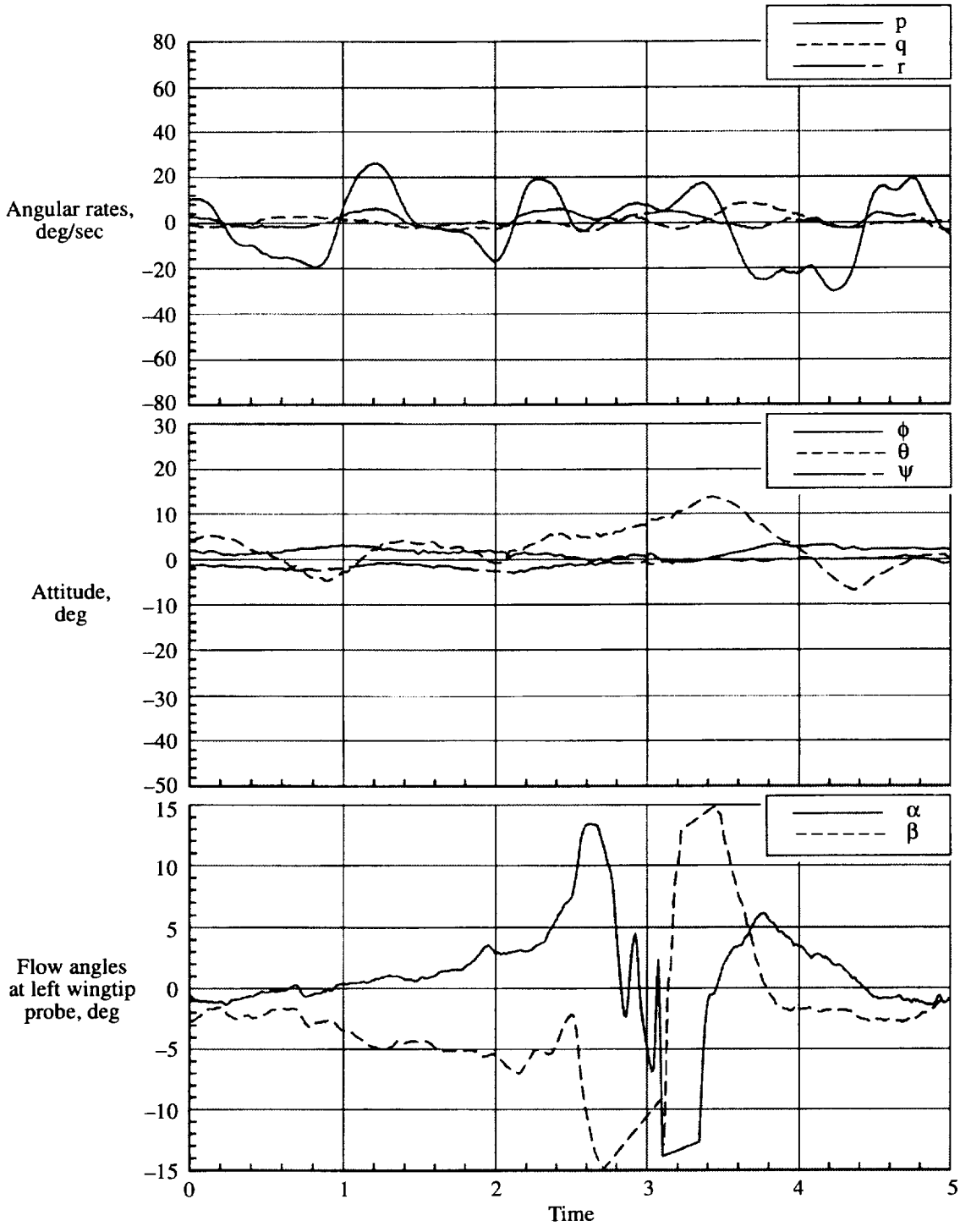

Figure 26. Concluded.

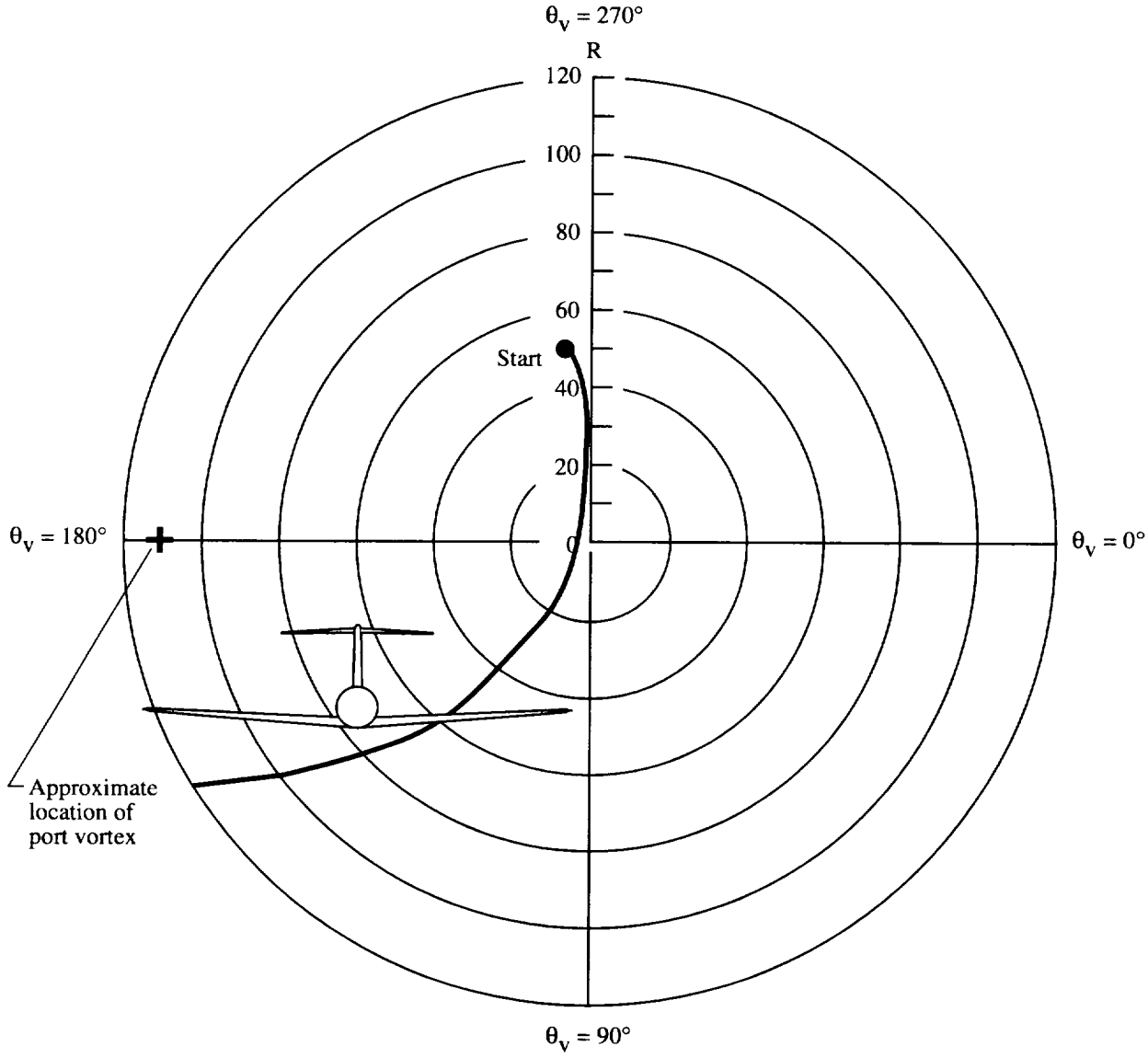

Figure 27. Descending vertical encounter. C_{L_g} = 1.25.

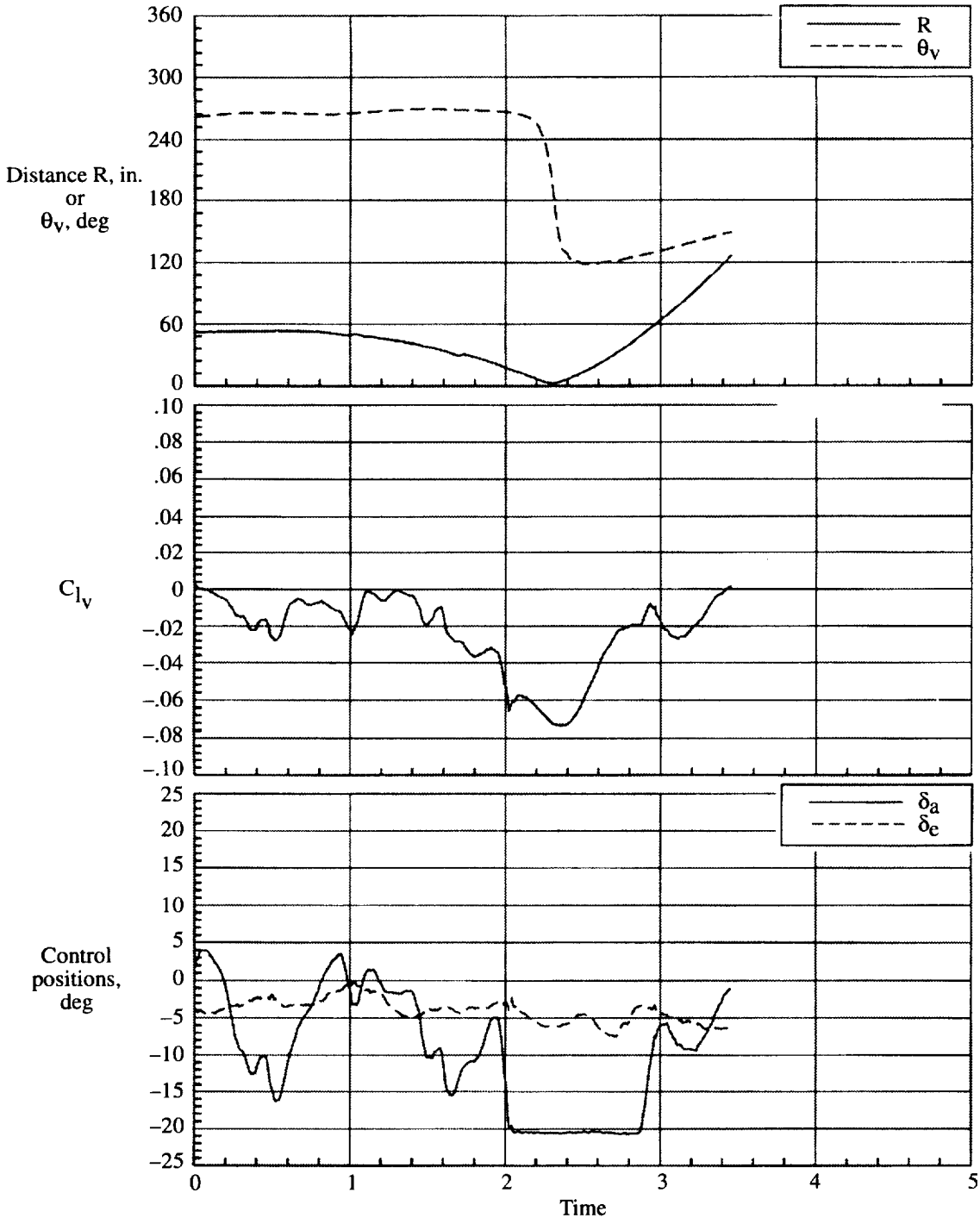

Figure 27. Continued.

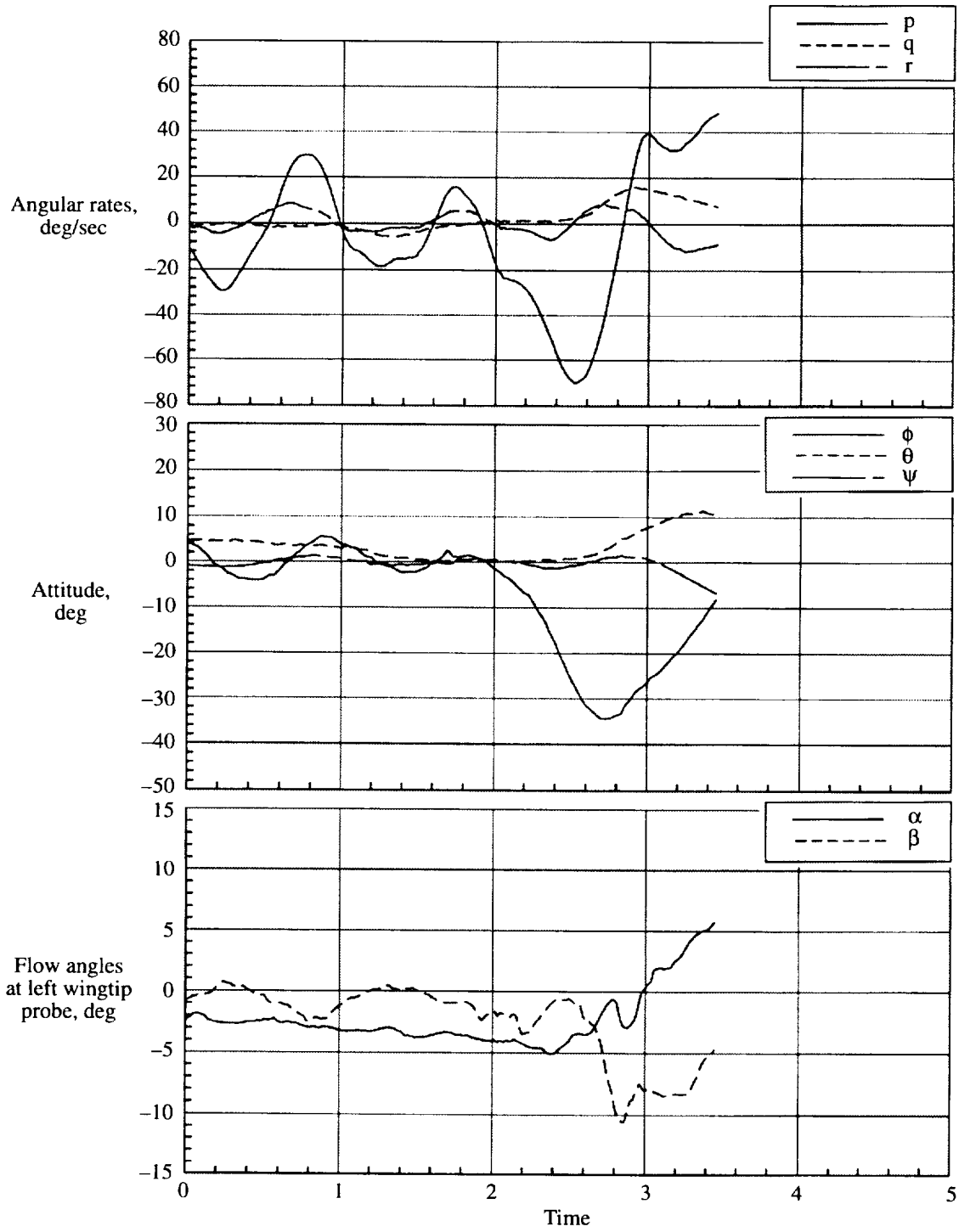

Figure 27. Concluded.

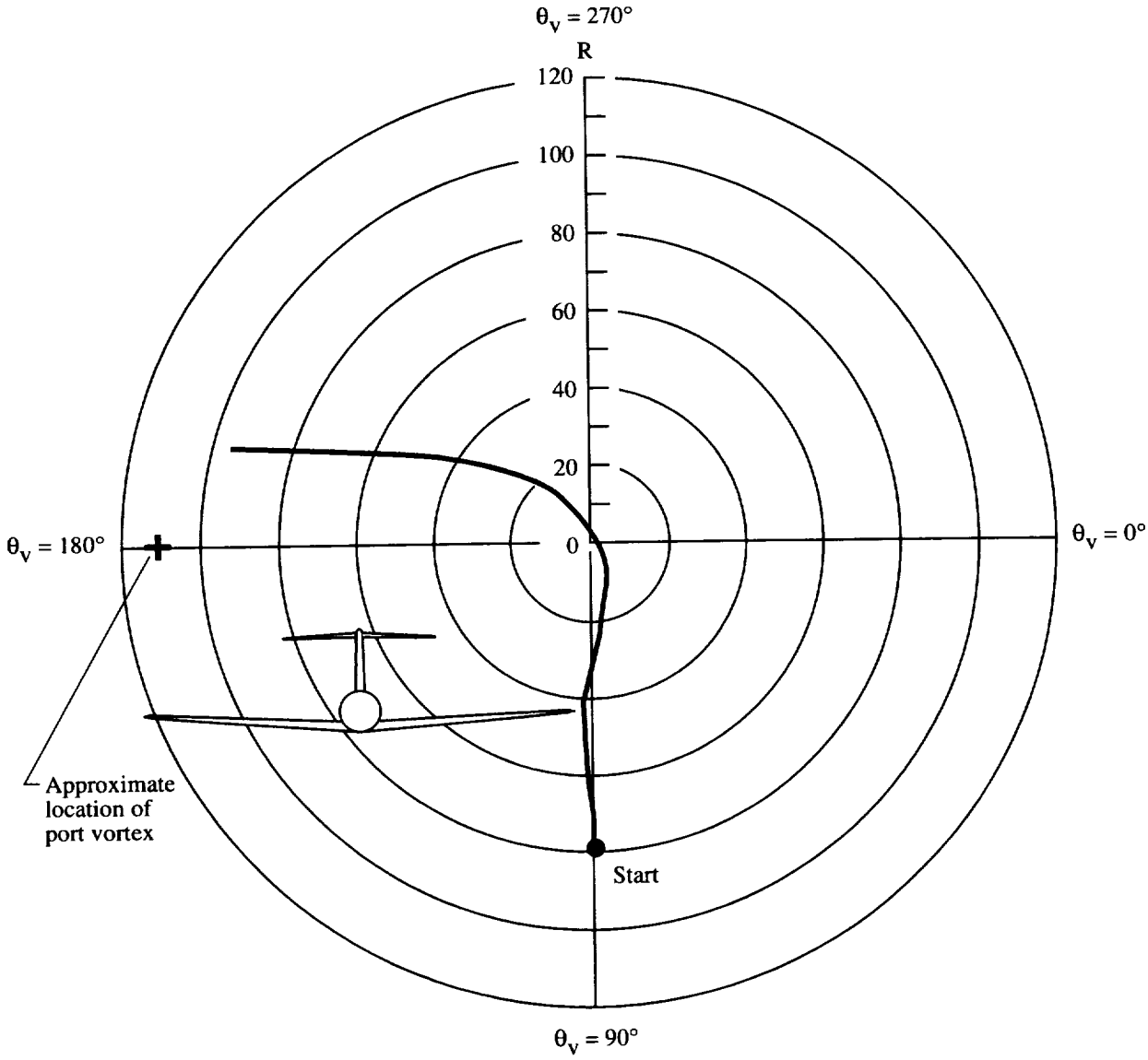

Figure 28. Ascending vertical encounter. $C_{L_g} = 1.25$.

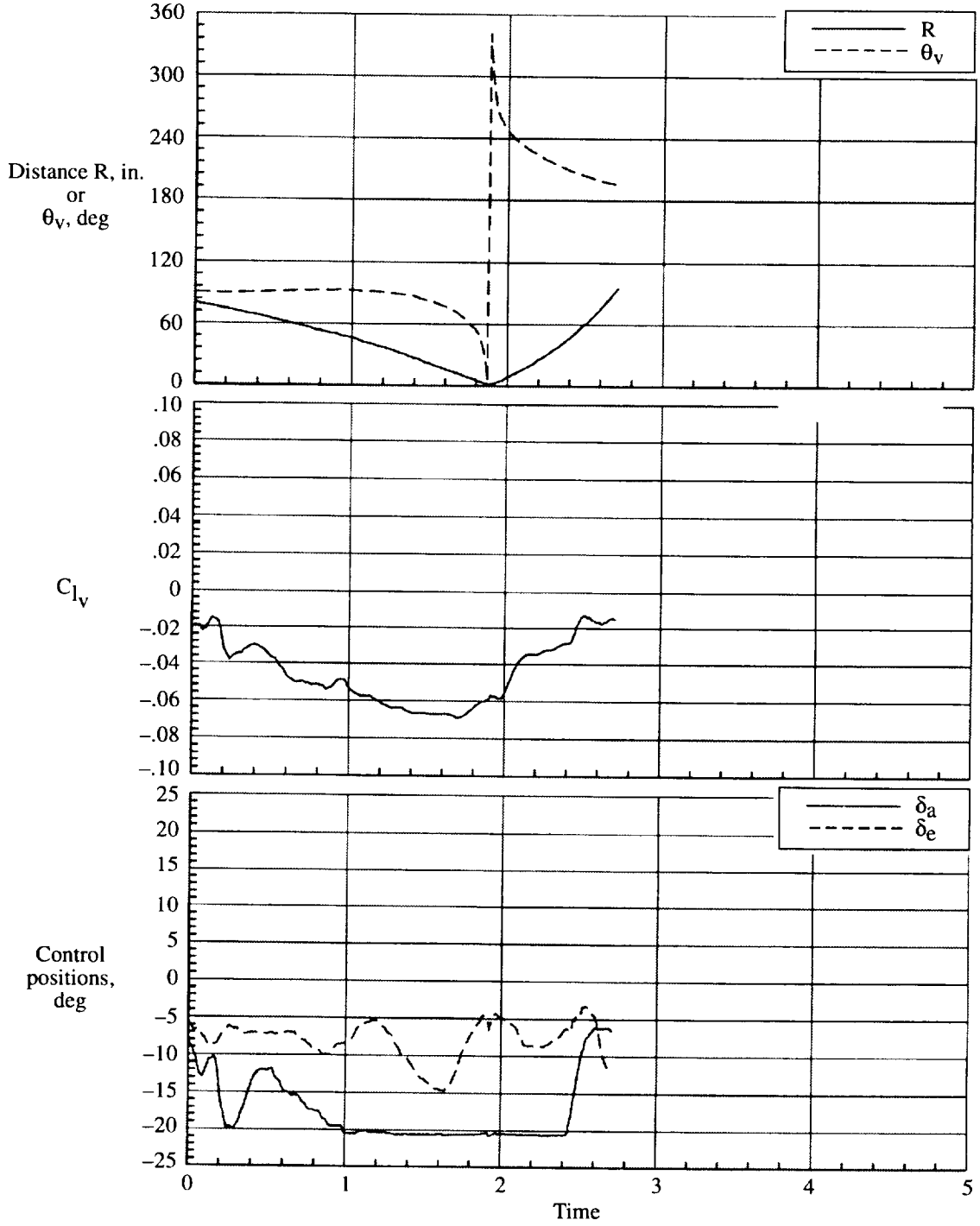

Figure 28. Continued.

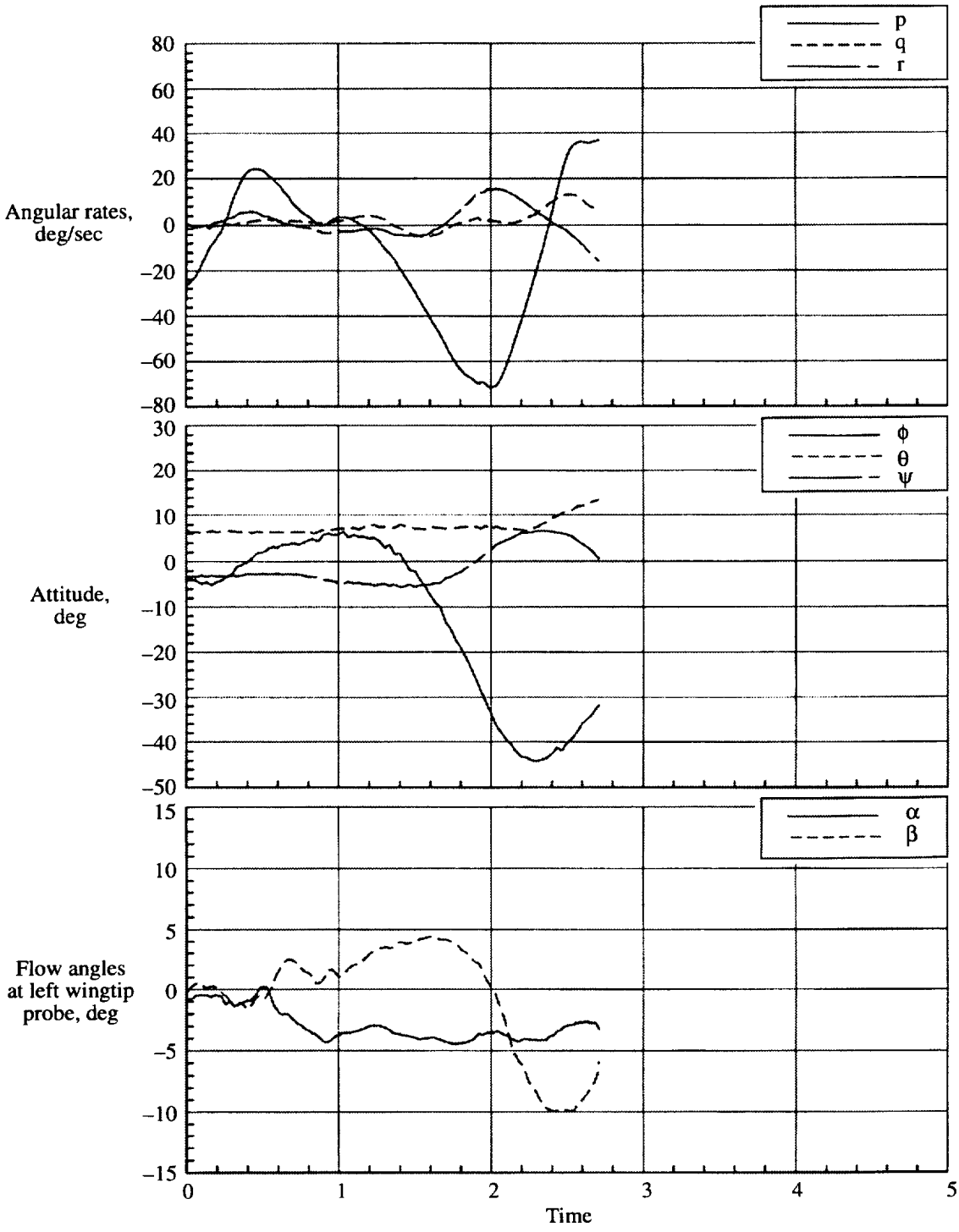

Figure 28. Concluded.

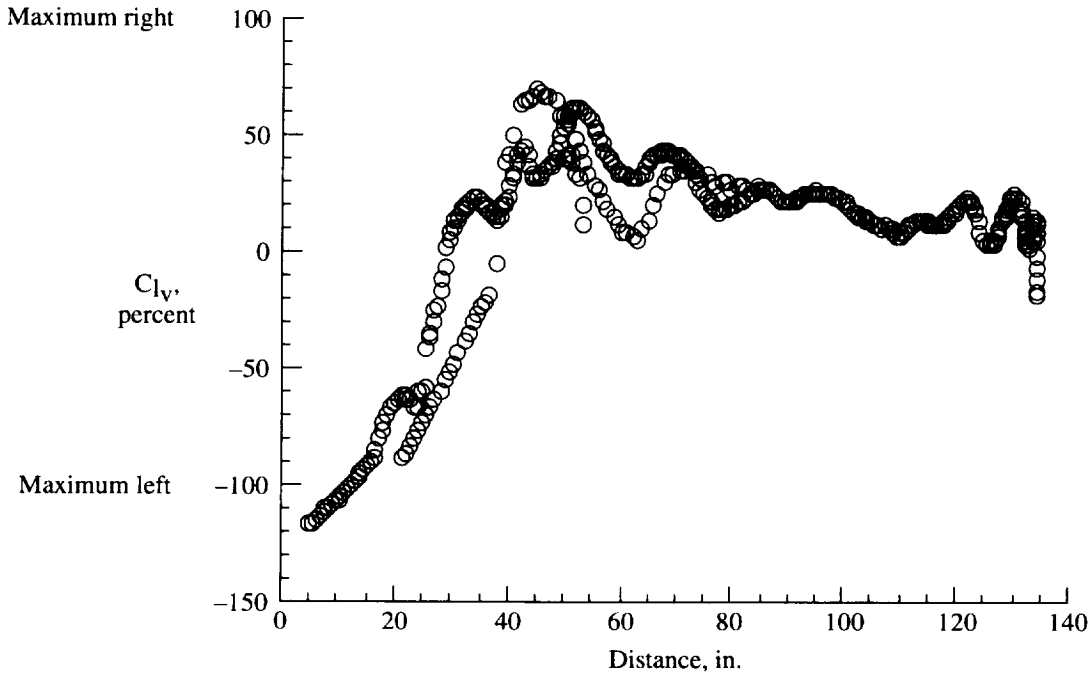

Figure 29. Rolling moment produced on model due to vortex interactions. C_{L_g} = 1.18 along 0° radial ±30°.

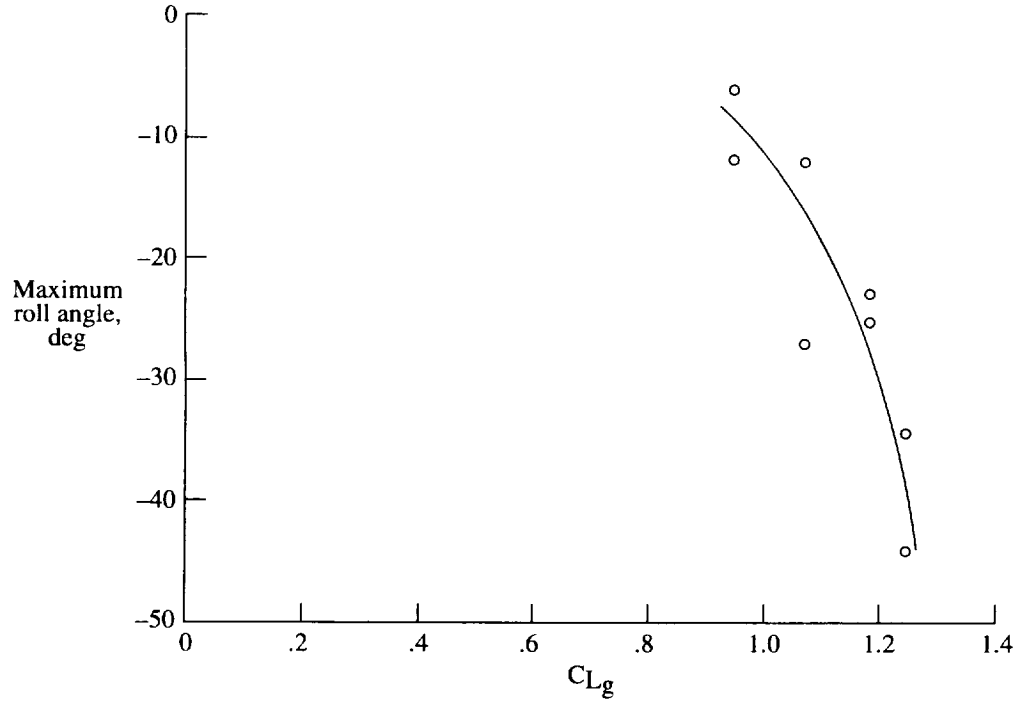

Figure 30. Maximum roll angle produced by vortex encounter.

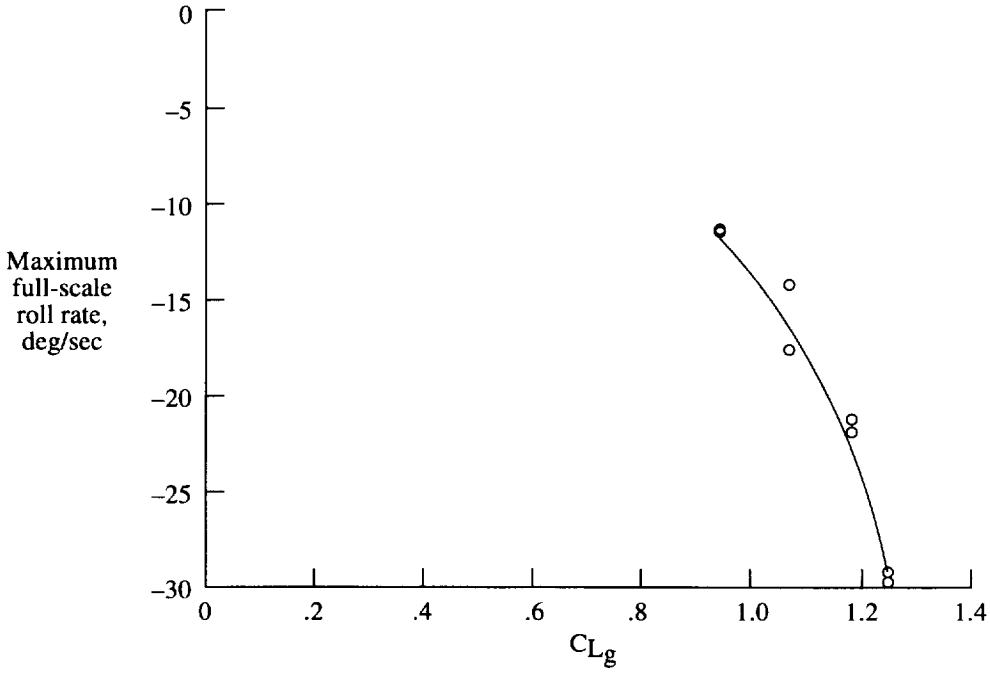

Figure 31. Maximum roll rate produced by vortex encounter.

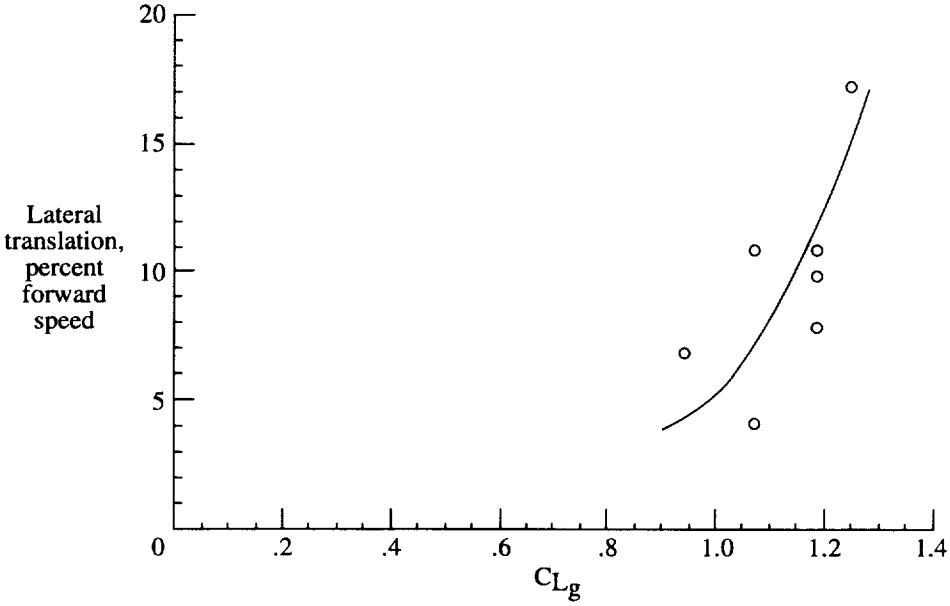

Figure 32. Maximum lateral translation velocity produced by vortex encounter.

REPORT DOCUMENTATION PAGE

Form Approved
OMB No. 0704-0188

1. AGENCY USE ONLY *(Leave blank)*	2. REPORT DATE	3. REPORT TYPE AND DATES COVERED
	November 1997	Technical Paper

4. TITLE AND SUBTITLE
Application of Wind Tunnel Free-Flight Technique for Wake Vortex Encounters

5. FUNDING NUMBERS
WU 505-64-13-15

6. AUTHOR(S)
Jay M. Brandon, Frank L. Jordan, Jr., Catherine W. Buttrill, and Robert A. Stuever

7. PERFORMING ORGANIZATION NAME(S) AND ADDRESS(ES)
NASA Langley Research Center
Hampton, VA 23681-2199

8. PERFORMING ORGANIZATION REPORT NUMBER
L-17462

9. SPONSORING/MONITORING AGENCY NAME(S) AND ADDRESS(ES)
National Aeronautics and Space Administration
Washington, DC 20546-0001

10. SPONSORING/MONITORING AGENCY REPORT NUMBER
NASA TP-3672

11. SUPPLEMENTARY NOTES
Buttrill: Unisys Corp., Hampton, VA.

12a. DISTRIBUTION/AVAILABILITY STATEMENT
Unclassified–Unlimited
Subject Category 08
Availability: NASA CASI (301) 621-0390

12b. DISTRIBUTION CODE

13. ABSTRACT *(Maximum 200 words)*
A wind tunnel investigation was conducted in the Langley 30- by 60-Foot Tunnel to assess the free-flight test technique as a tool in research on wake vortex encounters. A typical 17.5-percent scale business-class jet airplane model was flown behind a stationary wing mounted in the forward portion of the wind tunnel test section. The span ratio (model span-generating wingspan) was 0.75. The wing angle of attack could be adjusted to produce a vortex of desired strength. The test airplane model was successfully flown in the vortex and through the vortex for a range of vortex strengths. Data obtained included the model airplane body axis accelerations, angular rates, attitudes, and control positions as a function of vortex strength and relative position. Pilot comments and video records were also recorded during the vortex encounters.

14. SUBJECT TERMS
Free flight; Wake vortex; Wind tunnel

15. NUMBER OF PAGES
74

16. PRICE CODE
A04

17. SECURITY CLASSIFICATION OF REPORT	18. SECURITY CLASSIFICATION OF THIS PAGE	19. SECURITY CLASSIFICATION OF ABSTRACT	20. LIMITATION OF ABSTRACT
Unclassified	Unclassified	Unclassified	